



**BEN-GURION UNIVERSITY OF THE NEGEV
FACULTY OF ENGINEERING SCIENCES
DEPARTMENT OF MECHANICAL ENGINEERING**

***IMMERSED BOUNDARY METHOD
FOR INVESTIGATION OF CONFINED
THERMALLY DRIVEN FLOWS***

**THESIS SUBMITTED IN PARTIAL FULFILLMENT OF THE
REQUIREMENTS FOR THE M.Sc. DEGREE**

By: Yosef Gulberg

September 2016



**BEN-GURION UNIVERSITY OF THE NEGEV
FACULTY OF ENGINEERING SCIENCES
DEPARTMENT OF MECHANICAL ENGINEERING**

***IMMERSED BOUNDARY METHOD
FOR INVESTIGATION OF CONFINED
THERMALLY DRIVEN FLOWS***

**THESIS SUBMITTED IN PARTIAL FULFILLMENT OF THE
REQUIREMENTS FOR THE M.Sc. DEGREE**

By: Yosef Gulberg

Supervised by: Dr. Yuri Feldman

Author:.....

Date:.....

Supervisor:.....

Date:.....

Chairman of Graduate Studies Committee:.....

Date:.....

September 2016

ACKNOWLEDGEMENT

My utmost gratitude goes to my thesis advisor Dr. Yuri Feldman for his permanent and tireless guidance through every stages of the research, for inspiring me , and for giving me the opportunity and encouraging me to develop myself both in the area of theoretical and computational fluid mechanics. I wish him many more years of fruitful research.

I would like to express my gratitude to the academic and administrative staff in the Department of Mechanical Engineering for their personal support during my M.Sc. studies. A word of gratitude is also devoted to all colleagues from my research group and to my fellow students. Thanks for their help and for creating a friendly environment.

Abstract

The emphasis of this study is focused on passive control of natural convection flow in confined enclosures. In the first part of the study, the impact of the effective size of convection cells in spherical geometry is investigated. Laminar natural convection flow inside multi-layered spherical shells with internal hot and external cold boundaries was investigated. Direct numerical simulations (DNS), which were performed by utilizing the immersed boundary method, addressed the fully 3D natural convection flow inside spherical shells with concentric, eccentric, equi-spaced and non-equi-spaced, zero-thickness internal baffles. The insulation efficiency of the spherical shell was studied for up to four equi-spaced concentric internal layers. A unified functional dependency, correlating modified Nu^* and Ra^* numbers, was derived for spherical shells with up to four equi-spaced concentric internal layers. The effects of both vertical and horizontal eccentricities of the internal layers and of the width variation of concentric layers on the overall insulating performance of the spherical shell were investigated and quantified in terms of the Nu – Ra functionality.

In the second part of the study, the concept of “smart” thermo-insulation is established. A concept of "smart" thermally insulating materials, intelligently adapted for the specified engineering configuration, is established and extensively validated. The thermal insulation is achieved by local suppression of the momentum of the confined natural convection flow in the most critical regions, as determined by the linear stability analysis of the flow in the presence of implants of heterogeneous porous media. The implants are modelled by unconnected packed beds of equi-sized cylinders. The concept is based on the mesoscale approach, for which the non-slip boundary conditions in the vicinity of the packed beds are explicitly imposed by utilizing the immersed boundary (IB) method. Two different patterns of the "smart" porous media materials are established and their thermal insulation properties are quantified. It is shown that the optimized implants of heterogeneous porous media, occupying approximately only 5% of the overall volume, can drastically delay the steady-unsteady transition of the 2D natural convection flow in a square differentially heated cavity with thermally perfectly conducting horizontal walls. In addition, it is demonstrated that the implants allow to achieve a more than twofold decrease of heat flux rate through the cubic differentially heated cavity with all thermally perfectly conducting lateral walls.

Table of Contents

1	Introduction and literature survey	1
1.1.	Motivation of the study.....	1
1.1.1.	Natural convection inside spherical shells.....	1
1.1.2.	Smart passive thermo-insulating materials.....	5
1.2.	Objectives of the study.....	7
2	Theoretical background	9
2.1.	Chapter overview.....	9
2.2.	3D incompressible natural convection flow.....	9
2.2.1.	Physical model.....	9
2.2.2.	Discretization in time.....	11
2.2.3.	Immersed boundary method (IBM): direct forcing approach.....	11
2.3.	“Smart” thermal insulation – concept and theoretical background...	16
2.3.1.	Fully pressure-velocity coupled direct (FPCD).....	16
2.3.2.	Implicit immersed boundary FPCD time stepper.....	18
2.3.3.	Steady-state immersed boundary FPCD solver.....	21
2.3.4.	Linear stability immersed boundary FPCD solver.....	22
3	Results and Discussion	26
3.1.	Chapter overview.....	26
3.2.	Multi-layered spherical shell.....	27
3.2.1.	Verification.....	27
3.2.2.	Discussion.....	37
3.3.	Smart thermo-insulation.....	49
3.3.1.	Verification of the linear stability analysis.....	49
3.3.2.	Results and discussion.....	52
4	Conclusions	66
5	Bibliography	68

NOMENCLATURE

Initials

d	diameter of all the obstacle	[m]
d	discrete delta function	
D	diameter	[m]
F	volumetric boundary forces (non-dimensional)	
g	gravitational acceleration	[m/s ²]
Gr	Grashof number	
H	Helmholtz operator	
I	interpolation operator	
J	Jacobian	
L	characteristic length	[m]
N	total number of the shell boundaries (internal and external)	
Nu	Nusselt number	
p	pressure (non-dimensional)	
q	Eulerian heat source (non-dimensional)	
Q	Lagrangian point's heat fluxes (non-dimensional)	
r	distance (non-dimensional)	
R	radius	[m]
R	regularization operator	
Ra	Rayleigh number	
S	corresponds to all the cells belonging to the surface of immersed body	
t	time (non-dimensional)	
T	temperature	[°K]
ΔT	temperature difference	[°K]
U	the value of the boundary velocity (non-dimensional)	
\mathbf{u}	velocity vector field (non-dimensional)	
\mathbf{X}	position vector (non-dimensional)	

Superscript

n	time step index
'	perturbations
*	intermediate predicted velocity field
*	modified Nusselt or Rayleigh

Subscript

i	designation of internal diameter
i	Index of computational domain points
k	Index of Lagrangian points
p	pressure component
o	designation outer diameter
H	temperature hot
C	temperature cold
cr	critical values
u	x direction component
v	y direction component
w	z direction component
x	x direction component
y	y direction component
z	z direction component
Γ	value on body's boundary

Greek symbols

α	thermal diffusivity	$[m^2/sec]$
β	adiabatic coefficient of thermal expansion	$[1/^\circ K]$
δ	distance to the cube center	
ϵ	eccentricity	
ϵ_k	X coordinate of the Lagrangian point	
η_k	Y coordinate of the Lagrangian point	
ζ_k	Z coordinate of the Lagrangian point	
θ	non-dimensional temperature	
Θ^*	temperature at the Lagrangian points	
λ	leading eigenvalue	
μ	dominant eigenvalue, can be related to the leading eigenvalue λ	
ν	kinematic viscosity	$[m^2/sec]$
ρ	mass density	$[kg/m^3]$
ϕ	diameter ratio	
ω	angular frequency	
Ω	corresponds to a group of flow cells located in the close vicinity to the surface of the immersed body	

List of Figures

1.1	Three types of flow pattern as classified by Bishop et al. [4] and [5]: (a) crescent eddy , (b) kidney-shaped and (c) falling vortices.....	3
1.2	Three dimensional spiral flow pattern time sequence with air. Following disruption of the rolling vortices (a), (b), (c), consecutively [14].....	4
1.3	(a) schematic of 2D cavity with horizontal partition; (b) streamlines plot for $l=L$ [16].....	5
1.4	(a) schematic of 2D cavity with circular rods; (b) plot of streamlines [26].....	5
2.1	Physical model and system of coordinates for the spherical shell: (a) with no internal baffles; (b) with a single internal baffle and two concentric equi-spaced layers.....	10
2.2	A schematic staggered grid discretization of a two-dimensional computational domain D , with a segment of immersed boundary of a body B	12
3.1	Flow characteristics on a mid-plane cross section as a function of Ra number: temperature distribution and path lines projection obtained for the values of $\delta = -0.25, 0, 0.25$ on a 200^3 grid.....	30
3.2	Comparison between the axi-symmetric temperature field provided by Dehghan and Masih [52] and the present results obtained by fully three-dimensional simulations for: (a) $Ra = 10^3$; (b) $Ra = 10^4$; (c) $Ra = 10^5$. The contour colors correspond to 10 equi-spaced values of temperature in the range of $0 < \theta < 1$	31
3.3	A scheme of location of control points.....	32
3.4	Steady-state temperature distribution θ , and projection of the flow path lines for $Ra = 10^4$ in the mid cross section of a spherical shell with: (a) one internal layer; (b) two equi-spaced internal layers; (c) three equi-spaced internal layers; (d) four equi-spaced internal layers.....	39
3.5	Steady-state temperature distribution, θ , and projection of the flow path lines for $Ra = 5 \times 10^5$ in the mid cross section of a spherical shell with: (a) one internal layer; (b) two equi-spaced internal layers; (c) three equi-spaced internal layers; (d) four equi-spaced internal layers.....	41

3.6	<i>Nu</i> – <i>Ra</i> functionality obtained for spherical shells with different numbers of internal layers. The total number of walls for each spherical shell is given in parentheses. The dashed line corresponds to the universal correlation of Scanlan et al. [7] obtained for a single-layered spherical shell.....	43
3.7	<i>Nu*</i> – <i>Ra*</i> functionality. The correlation for modified <i>Nu*</i> is valid for a multilayered spherical shell containing up to five equi-spaced concentric walls (four internal layers).....	44
3.8	Steady-state flow fields, obtained at the mid-plane cross section of a three-wall spherical shell for $Ra = 5 \times 10^5$. Contours of the temperature θ and projection of the flow path lines for: (a) $\epsilon = 0,167$; (b) $\epsilon = 0,335$	46
3.9	Steady-state flow fields obtained at the mid-plane cross section of a three-wall spherical shell for $Ra = 5 \times 10^5$. Contours of the temperature θ and projection of the flow path lines for: (a) $\epsilon = 0,167$; (b) $\epsilon = 0,167$	47
3.10	Steady-state flow fields obtained at the mid cross section of a three-wall spherical shell for $Ra = 5 \times 10^5$. Contours of the temperature θ and projection of the flow path lines for: (a) $D_b/D_i = 1.17$; (b) $D_b/D_i = 1.83$	48
3.11	Vertically aligned cylinders confined by a square cavity: schematic representation of a geometrical model of the computational domain. Arrow indicates the direction in which the force of gravity acts.....	50
3.12	Contours of the averaged oscillating amplitudes and the corresponding absolute values of leading eigenvectors obtained for: (a) velocity component u_x ; (b) velocity component u_y ; (c) temperature, θ	52
3.13	A typical flow field inside a differentially heated cavity filled with thermal insulating material. $Ra = 10^7$, <i>Porosity</i> = V_V/V_T , V_V -void, V_T -total. (a) $\phi = 0.9$ (b) $\phi = 0.8$ (c) $\phi = 0.7$	53
3.14	<i>Nu</i> – <i>Ra</i> functionality for a differentially heated cavity filled with thermal insulating material.....	54

3.15	Contours of the criterion A and the corresponding steady state distribution of temperature, θ with superimposed streamlines obtained at $Ra = 2.11 \times 10^6$ for: (a) no obstacles; (b) 2 obstacles; (c) 4 obstacles; (d) 6 obstacles; (e) 8 obstacles; (f) 10 obstacles; (g) 20 obstacles; (h) 40 obstacles. Diameter of all the obstacles is equal to $d = 0.04$	58
3.16	Contours of the criterion B and the corresponding steady state distribution of temperature θ , with superimposed streamlines obtained at $Ra = 2.11 \times 10^6$ for: (a) no obstacles; (b) 2 obstacles; (c) 4 obstacles; (d) 6 obstacles; (e) 8 obstacles; (f) 10 obstacles; (g) 20 obstacles; (h) 40 obstacles. Diameter of all the obstacles is equal to $d = 0.04$	61
3.17	Variation of the values of the averaged Nu number obtained for the vertical hot wall of the cavity at $Ra_{cr} = 2.11 \times 10^6$ and the critical Rayleigh, Ra_{cr} number for the steady-unsteady transition obtained by the linear stability analysis as a function of a number of cylindrical obstacles for : (a) A optimization criterion; (b) B optimization criterion.....	62
3.18	3D setup obtained by extrusion of the corresponding 2D configurations in the z direction with superimposed temperature distribution at mid cross-section of the cavity obtained at $Ra = 2.11 \times 10^6$ by : (a) 20 cylinders location of which was obtained by utilizing optimization criteria A and B ; (b) 40 cylinders location of which was obtained by utilizing optimization criteria A and B	64

List of Tables

3.1	Comparison between the present and the scanned [51] average Nu values obtained for the flow developing in the presence of an isothermal hot sphere placed within a cubic container with all isothermal cold walls.....	28
3.2	Flow characteristics along the spherical shell center-lines, all the velocity components (u_x , u_y , u_z) are multiplied by a factor of 10^3	33
3.3	Average (in space) Nu numbers for steady laminar axi-symmetric flow.....	36
3.4	Average (in time and in space) Nu numbers for unsteady 3D flow. Results reported for axi-symmetric flow are given in parentheses.....	37
3.5	Nu number values for a double-layered horizontally eccentric internal sphere.....	49
3.6	Verification of grid independence of the averaged Nu values calculated at the hot wall of the cubic cavity for $Ra = 2.11 \times 10^6$	65
3.7	Validation of the concept of "smart" thermally insulating materials for 2D and 3D flows. The Nu values were averaged over a hot wall of a differentially heated cavity with all thermally perfectly conducting horizontal (2D) and lateral (3D) walls.....	65

Chapter 1

Introduction and literature survey

1.1. Motivation of the study

Passive control of natural convection flow in confined enclosures has gained significant attention in past decades due to its importance for many engineering designs. The phenomenon present in thermal energy storage (TES) systems, nuclear reactor and heat exchangers, climate control of buildings, just to name a few. A vast majority of studies reported in the literature have employed a heuristic approach, investigating the effect of obstacles embedded into the enclosure on the momentum and the thermal properties of the confined flow. The present work aims at developing a novel methodology to further enhance and systemize the passive control of confined natural convection flows.

In the first part of the study, the impact of the effective size of convection cells in spherical geometry controlled by embedding internal thin baffles between hot and cold boundaries of a differentially heated spherical shell is investigated. The fully 3D natural convection flow is investigated by the series of numerical simulations. The numerical simulations are enhanced by the immersed boundary functionality to impose no-slip constraints on all the solid boundaries. An extensive parametric study including concentric, eccentric, equi-spaced and non-equi-spaced internal baffles is performed to improve thermal insulation efficiency of the spherical annuli.

In the second part of the study, the concept of “smart” thermo-insulation is established. The key idea is to control the confined natural convection flow by locally suppressing its momentum in the most critical regions of the convective flow. Those regions are revealed by the formal linear stability analysis. Efficiency of the proposed concept of smart thermo-insulation is demonstrated by applying it to the natural convection flow in square (for 2D) and cubic (for 3D) differentially heated cavities. It is demonstrated that the proposed approach can drastically delay the steady-unsteady transition of the 2D natural convection flow and achieve a more than twofold decrease of heat flux through the 3D differentially heated cavity.

1.1.1. Natural convection inside spherical shells

Buoyancy-driven flow developing inside spherical annuli has been the subject of considerable research, both theoretical and experimental for the past fifty years. Typically, the buoyancy-driven

flow between two isothermal concentric spheres (where the inner sphere is held at a high temperature and the outer sphere at a low temperature) has been investigated as a function of the diameter ratio, $\phi = D_i/D_o$ and the Rayleigh Ra and Prandtl Pr , numbers. The interest of the scientific and engineering community to spherical annuli configuration is due to the fact that the flow comprises an essential heat transfer mechanism in various engineering design problems, such as in solar energy collectors, storage tanks, thermal energy storage (TES) systems and nuclear reactors. Another potential application of spherical annuli is related to the design of the Titan Montgolfiere hot air balloon, which was recently chosen by NASA as the air-robot vehicle of choice for the exploration of Titan's atmosphere. Given Titan's low gravity (one-seventh that of Earth) and its cryogenic atmospheric temperatures (72–94 K), heat transfer by radiation can safely be neglected, and natural convection can be regarded as the only heat transfer mechanism for the stationary suspended balloon. Such a balloon, designed to provide a minimized heat flux rate through its walls, could serve as a sustainable air-robot platform for carrying a payload sufficient for a long-term space mission. The concept of the double-walled Titan Montgolfiere, for which the spherical shell plays the role of a thermal insulator separating the hot interior of the balloon from the cold surroundings, has recently been established and investigated by Samanta et al. [1] and Feldman et al. [2]. One of the main findings of both studies was that theoretical estimation of the heat flux rate through the boundaries of the insulating gap of both scaled and full-scale balloons has the greatest uncertainties. This finding motivated further research [3], which focused on a more detailed analysis of transitional and fully turbulent, natural convection flows inside narrow spherical differentially heated shells ($0.8 \leq \phi \leq 0.9$), and yielded an improved $Nu-Ra$ correlation derived specifically for that range of ϕ values.

Pioneering experimental studies considering natural convection in the spherical annuli are due to the works of Bishop et al. [4] and [5], who focused on visualization of the flow and classified three distinct types of flow pattern – “crescent eddy”, “kidney-shaped” and “falling vortices” (see Fig.1.1) – that depend on the diameter ratio ϕ of the shells.

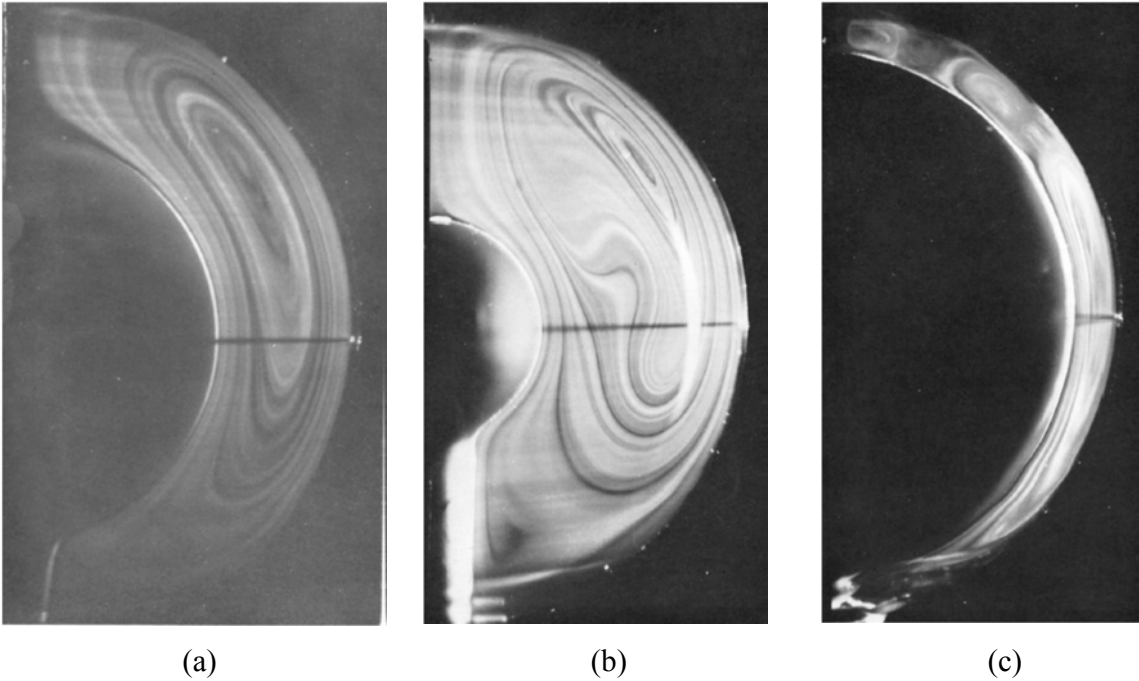


Figure 1.1. Three types of flow pattern as classified by Bishop et al. [4, 5] : (a) crescent eddy; (b) kidney-shaped eddy; (c) falling vortices.

The experimental results of Bishop et al. [4, 5] were confirmed by the study of Mack and Hardee [6], who derived a low-Rayleigh-numbers analytical solution for the natural convection of air between two concentric spheres. More recently, the natural convection flow of working fluids other than air (namely, water and silicone oils) was experimentally addressed by Scanlan et al. [7] and visualized by Yin et al. [8]. The latter group described naturally induced flow patterns and categorized the type of the flow for each fluid in terms of the inverse of the relative gap width and the Rayleigh number. Subsequent numerical studies on steady and transient, natural convection flow inside spherical shells extended the state of the art to an even wider range of Pr ($0.71 \leq Pr \leq 100$) [9, 10] and Ra ($10^2 \leq Ra \leq 5 \times 10^5$) [10] numbers, and to the analysis of vertically eccentric configurations [11].

The theoretical analysis of unsteady natural convection inside a differentially heated spherical annulus is a challenging problem, since different flow regimes can dominate locally in its different regions, taking the form of the Rayleigh-Bénard convection at the top of the shell, of a differentially heated cavity at the near-equatorial region, and of a thermally stable flow regime, at the bottom of the shell. Moreover, instabilities and transition scenarios are sensitive to the value of the Pr number and to the ratio of the internal to external diameter, ϕ [12, 13]. For shells with an internal hot

boundary and an external cold boundary, the flow patterns vary with the ratio ϕ : Powe et al. [14] described a “modified kidney shaped eddy” for wide shells ($\phi \leq 0.5$), an “interior expansion–contraction” for $0.5 \leq \phi \leq 0.65$, a “three dimensional spiral” flow for $0.65 \leq \phi \leq 0.85$ (shown in Fig. 1.2), and a “falling vortices” pattern for narrow shells ($0.85 \leq \phi$). Fütterer et al. [15] reported that the flow inside shells of large and moderate widths ($0.41 \leq \phi \leq 0.71$), with a cold internal boundary and a hot external boundary, exhibited an unsteady “dripping blob” phenomenon for $Pr = \infty$.

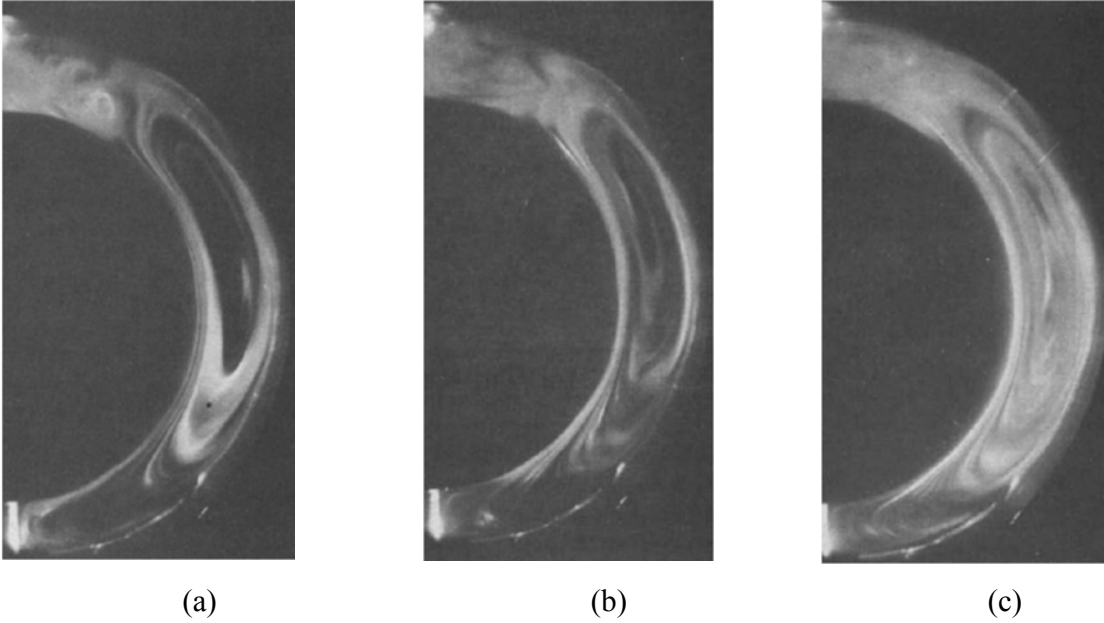


Figure 1.2. Three dimensional spiral flow pattern time sequence with air. Following disruption of the rolling vortices (a), (b), (c), consecutively [14].

The first part of the present study focuses on investigation of the impact of the effective size of convection cells on the heat flux in spherical geometry. The size of convection cells is controlled by embedding internal thin baffles between hot and cold boundaries of differentially heated spherical shells. The effectiveness of equi-spaced/non-equi-spaced and concentric/eccentric configurations of the internal baffles is studied. Different configurations of the internal baffles are simulated by numerical simulations and enhanced by the immersed boundary functionality to impose no-slip constraints on all the solid boundaries. Additionally, we propose a novel modified $Nu^* - Ra^*$ correlation for a spherical shell with up to four internal equi-spaced concentric layers in the range of $10^2 \leq Ra \leq 10^7$.

1.1.2. Smart passive thermo-insulating materials

Enhancement of passive control of confined natural convection flows has attracted considerable attention over the past decades. Passive flow control does not involve additional energy consumption and does not require design of auxiliary systems, which explains its high attractiveness for many engineering applications. In practice, passive flow control is typically implemented by either exploiting the flow blockage effects of solid internal discrete obstructions, or by partition of the interior of confinement (see Fig. 1.3), thereby decreasing the effective length scale of the natural convection flow [16-20]. Recently, a number of studies investigating the effect of an array of adiabatic bodies immersed into the bulk of convective flow on its thermal properties have been published [7, 8, 21- 27] (see e.g. Fig. 1.4).

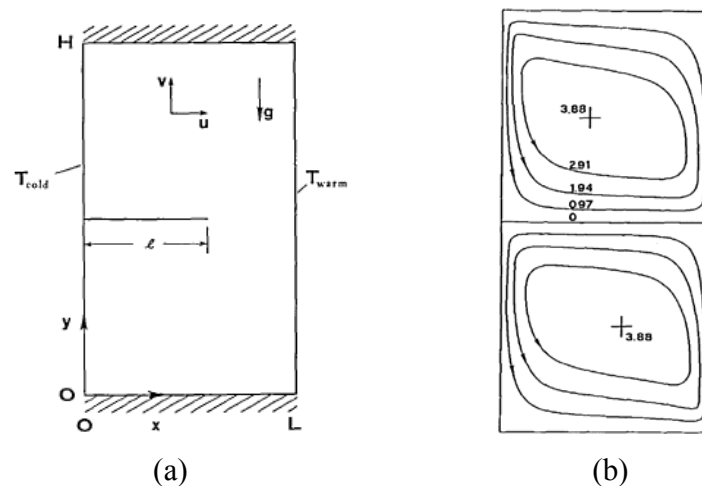


Figure 1.3. (a) scheme of 2D cavity with horizontal partition; (b) streamlines plot for $l=L$ [16].

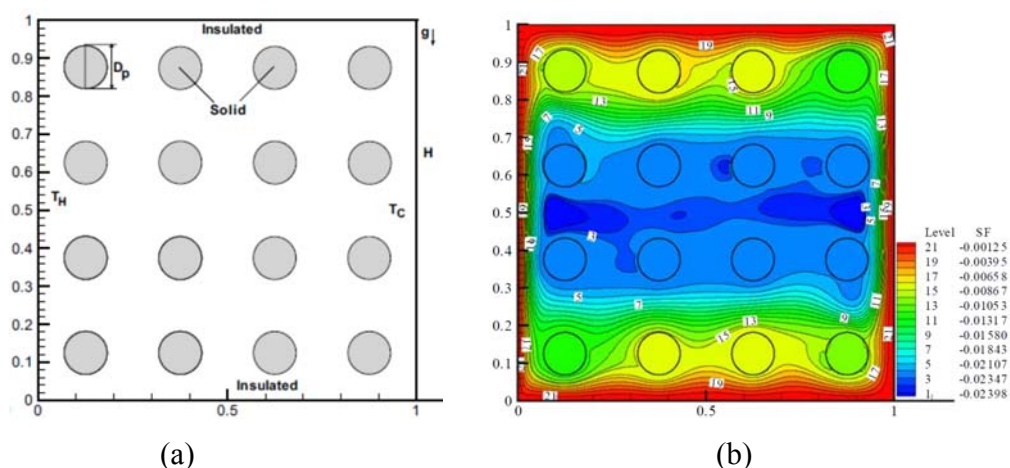


Figure 1.4. (a) scheme of 2D cavity with circular rods; (b) streamlines plot [26].

Motivated by the aforementioned, the present study focuses on investigation of the potential of applying heterogeneous porous media for enhancement of flow control in terms of the thermal insulating efficiency. Analysis of flow and heat transfer in porous media has traditionally been based on applying volume-averaging techniques to fluid flow equations. In such cases, the complex geometry of solid boundaries is modelled by assuming a continuous phase that overlaps solid and fluid regions and is treated by macroscopic averaged equations (see e.g [28-33]). Flow fields near the solid boundaries are not resolved explicitly, and interface effects are modelled by a priori provided correlations. The drawback of volume-averaging techniques is their lack of generality, resulting from the considerable morphological variations of porous materials. Therefore, an accurate prediction of important flow characteristics of a particular porous material can be performed only if the corresponding experimental data is available. However, experimental data is typically acquired for specific porous materials and flow conditions, thus severely restricting the application of volume-averaging techniques.

The mesoscale approach, explicitly resolving flow near solid surfaces, offers an alternative to the volume-averaging technique. The approach has gained popularity in the last decade with a rapid development of computational power. The studies performed to date typically treat the porous materials as composite voids and beds of solid particles, and address flow through ordered, staggered or randomly packed beds of different particle shapes that correspond to various porous media configurations. Although the mesoscale modeling of porous media is typically restricted to non-contacting packed beds of solid particles, the characteristic distance between them is close enough to significantly affect the heat and mass transfer processes. This allows for the further generalization of the obtained results to elucidate the fundamental macroscale mechanisms and geometrical characteristics of the corresponding heterogeneous porous media. Widely used application of the mesoscale approach is related to the passive control of confined natural convection flows in terms enhancement of their thermo-insulating efficiency. The research in this area is mainly motivated by the need to control heat flux rate through the confined enclosures partially filled with solid products of various forms, orientations and distributions, and is relevant to indoor environmental control [34, 35], refrigeration equipment and thermal management of greenhouses [22], and cooling of electronic devices [36, 37] etc.

The second part of the present work is aimed to develop a systematic mesoscale approach based the methodology for control of incompressible natural convection flows in confined enclosures

utilizing heterogeneous porous media. This task has so far been performed only heuristically, attributing the reduced heat flux rate to the blockage effects of solid non-connected obstacles and to redirection of the flow away from the vertical cold and hot walls toward the cavity center.

The principal novelty of the present work is to control the flow by intelligent suppression of the fluctuations of the major flow characteristics (for example, perturbations, velocity components, temperature, pressure, or their combinations) in the most critical regions, as determined by linear stability analysis of the slightly supercritical flow. The control is achieved by explicit placing of heterogeneous porous media, whose spatial location, homogeneity and porosity have been optimized for the specific flow configuration. Porous media implants, created by this methodology, establish the concept of smart thermo-insulating materials, intelligently suppressing the oscillations of the thermal flow in accordance with the given optimization criteria. Efficiency of the proposed concept of smart thermo-insulation is demonstrated by applying it to the natural convection flow in square (for 2D) and cubic (for 3D) differentially heated cavities. It is shown that optimized, non-homogenous, porous media implants, occupying approximately only 5 percent of the overall volume, can drastically delay the steady-unsteady transition of the 2D natural convection flow, and achieve a more than twofold decrease of heat flux rate through the cubic differentially heated cavity.

1.2. Objectives of the study

The present work has two primary objectives. Each primary objective is preceded by the corresponding secondary objective. The first primary objective is to investigate the potential of enhancement of insulating properties of spherical annuli by inserting internal, thermally passive, idealized baffles of zero thickness. All the baffles considered in the present study are of a spherical geometry. The influence of various configurations of the baffles (equi-spaced/non-equi-spaced and concentric/eccentric) on the natural convection flow inside the differentially heated spherical annuli and on the thermal insulating properties of the annuli are parametrically investigated. The aim is to derive a novel $Nu - Ra$ correlation, which will allow fast and reliable estimation of insulating efficiency of multilayered spherical shells. The study is also aimed at investigating the effect of the eccentricity of the internal baffles (both horizontal and vertical) on the developing various flow patterns. The fundamental questions regarding the impact of both vertical and horizontal eccentricities on the total heat flux rate through the shell boundaries, and the effect of

the width of the internal layer and its proximity to the hot and cold boundaries on the total heat flux, are also addressed.

The above primary objective is preceded by adapting and customization of an in-house developed code, allowing for the time integration of the Navier Stokes and the energy equations with embedded IB functionality to impose no-slip boundary conditions on all solid boundaries. The solver extends the general pressure–velocity segregated solver [38] (based on the tensor product factorization (TPF) method combined with the Thomas solver (TPT)) with the immersed boundary functionality. Prior to applying the developed solver, we perform its extensive verification by means of detailed grid independence study and comparison with previously published data, relevant to the primary objective of the research.

The second primary objective of the present study is to develop a formal methodology for establishing a concept for design of "smart" thermally insulating materials. In practice, such materials can be built of implants of heterogeneous porous media whose geometry and spatial orientation is intelligently adapted to any specific engineering configuration. The implants of porous media are modelled as packed beds consisting of unconnected equi-sized cylinders. At the first stage, the aim is to determine the location of each cylinder by an iterative procedure based on the linear stability analysis of the 2D flow fields. The objective then is to perform an extensive study to validate an adaptation of the obtained 2D patterns of the porous media to their 3D analogs embedded into the bulk of realistic 3D confined natural convection flow.

The above primary objective is again preceded by adapting and customization of an in-house developed linear stability solver, capable of analyzing 2D domain flow in the presence of a large number of immersed bodies of arbitrary shapes. An extensive verification study of the solver is performed for the flow configurations relevant to the present research, including grid independence analysis of the steady state and linear stability results in terms of average, Nu values and critical values of Rayleigh, Ra_{cr} and oscillating frequency, ω_{cr} .

Chapter 2

Theoretical background¹

2.1. Chapter overview

In this chapter, the physical model and numerical methodology utilized in the present study are presented. The first part of the study focuses on the natural convection flow between hot and cold boundaries of a differentially heated spherical shell in the presence of single or multiple spherical baffles of various orientations. In Section 2.2, the theoretical background regarding simulation of the 3D incompressible natural convection flow in single- and multi-layered spherical shells is given. The emphasis is on the presentation of the physical model, and on a detailed explanation of the immersed boundary method utilized in the present study to resolve the natural convection flow near the solid boundaries. In the second part of the study, the concept of “smart” thermo-insulating materials is established. In Section 2.3, the numerical methodology used for establishing and verification of the concept is detailed. The idea underlying the “smart” thermal insulation is based on the local suppression of the momentum of the natural convection flow. In practice, the implementation of the local suppression is based on well-defined criteria. The criteria are formally provided by the 2D linear stability analysis, enhanced by the embedded IB functionality. The milestones of the utilized linear stability analysis are given in Sections 2.3.4 and 2.3.5.

2.2. 3D incompressible natural convection flow

2.2.1. Physical model

The natural convection flow inside single or multi-layered spherical shells is described by the momentum, energy and continuity equations. The Boussinesq approximation is utilized to model the buoyancy effect. The governing equations are formulated in Cartesian coordinates (x,y,z) , with the origin located at the center of the shell and the gravity acting opposite to the positive direction of z axis (see Fig. 2.1). The continuity equation Eq. (2.1), Navier–Stokes Eq. (2.2), and energy equation Eq. (2.3), written in dimensionless form are:

$$\nabla \cdot \mathbf{u} = 0, \tag{2.1}$$

¹ This chapter is based on Y. Gulberg, Y. Feldman [39], Y. Feldman, Y. Gulberg [54]

$$\frac{\partial \mathbf{u}}{\partial t} + (\mathbf{u} \cdot \nabla) \mathbf{u} = -\nabla p + \sqrt{\frac{Pr}{Ra}} \nabla^2 \mathbf{u} + \theta \vec{e}_z, \quad (2.2)$$

$$\frac{\partial \theta}{\partial t} + (\mathbf{u} \cdot \nabla) \theta = \frac{1}{\sqrt{PrRa}} \nabla^2 \theta, \quad (2.3)$$

where $\mathbf{u}(u, v, w)$, p , t , and θ are non-dimensional velocity, pressure, time and temperature, respectively, and \vec{e}_z is a unit vector in the z direction.

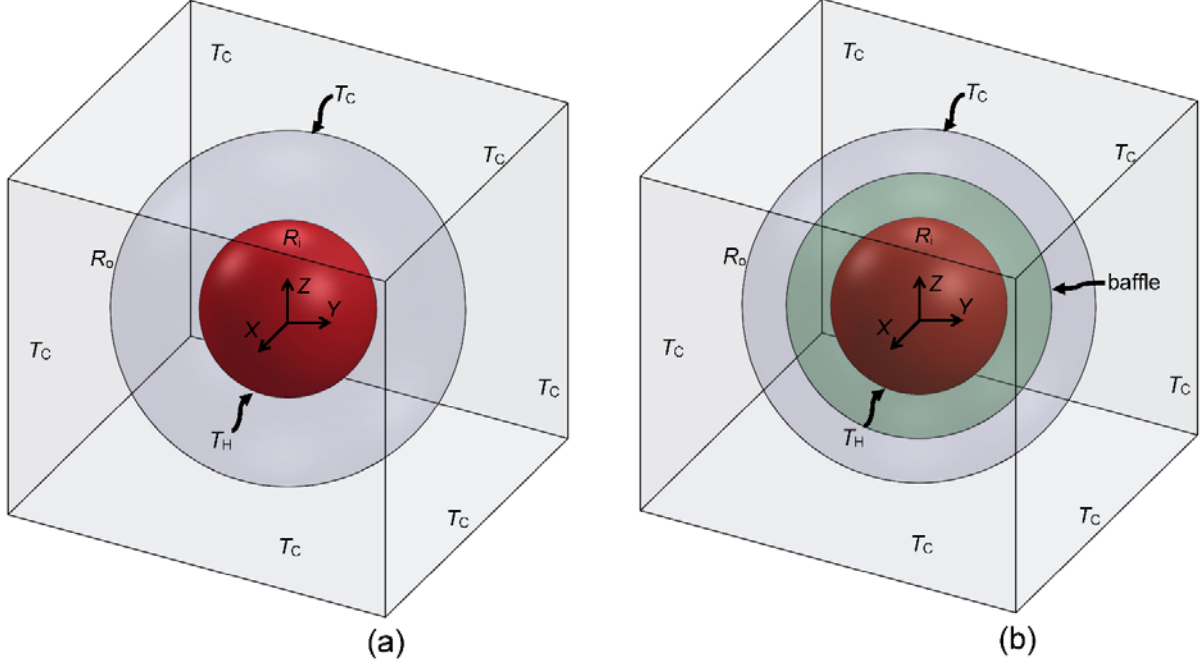


Figure 2.1. Physical model and system of coordinates for the spherical shell: (a) with no internal baffles; (b) with a single internal baffle and two concentric equi-spaced layers.

These non-dimensional equations were obtained using the characteristic length L , $U = \sqrt{g\beta L\Delta T}$, $t = L/U$ and $P = \rho U^2$ for length, velocity, time and pressure, respectively. Here $L = R_o - R_i$ is the total shell width, R_o is the radius of the outer sphere, and R_i is the radius of the inner sphere, ρ is the mass density, β is the adiabatic coefficient of thermal expansion, g is the gravitational acceleration, and $\Delta T = T_H - T_c$ is a temperature difference between the cold and hot boundaries. The non-dimensional temperature θ is defined as $\theta = (T - T_c)/\Delta T$. The Ra and Pr numbers are $Ra = \frac{g\beta}{\nu\alpha} \Delta T L^3$ and $Pr = \nu/\alpha$, where α is the thermal diffusivity and ν is a kinematic viscosity. The Boussinesq approximation $\rho = \rho_0(1 - \beta(T - T_c))$ is utilized to model the buoyancy effect. Consequently, an additional term appears as a source in the z -direction Navier-Stokes Eq.2.2, thereby allowing for the temperature-velocity coupling.

2.2.2. Discretization in time

The time derivative in the unsteady momentum and the energy equation is approximated by the first order forward Euler's scheme:

$$\frac{\partial f^{n+1}}{\partial t} = \frac{f^{n+1} - f^n}{\Delta t} \quad (2.4)$$

Utilizing the Euler's scheme, the momentum Eq. (2.2) and the energy (Eq. (2.3)) equations can be rewritten as follows:

$$\frac{u^{n+1} - u^n}{\Delta t} + (\mathbf{u}^n \cdot \nabla) \mathbf{u}^n = -\nabla p + \sqrt{\frac{Pr}{Ra}} \nabla^2 \mathbf{u}^{n+1} + \theta^{n+1} \vec{e}_z \quad (2.5)$$

$$\frac{\theta^{n+1} - \theta^n}{\Delta t} + (\mathbf{u}^n \cdot \nabla) \theta^n = \frac{1}{\sqrt{PrRa}} \nabla^2 \theta^{n+1} \quad (2.6)$$

After carrying out space and time discretizations, Eqs. (2.1), (2.5) and (2.6) are presented in a block matrix form:

$$\begin{bmatrix} H_u & 0 & 0 & 0 & -\nabla_p^x \\ 0 & H_v & 0 & 0 & -\nabla_p^y \\ 0 & 0 & H_w & \vec{e}_z & -\nabla_p^z \\ 0 & 0 & 0 & H_\theta & 0 \\ \nabla_u^x & \nabla_v^y & \nabla_w^z & 0 & 0 \end{bmatrix} \begin{bmatrix} u^{n+1} \\ v^{n+1} \\ w^{n+1} \\ \theta^{n+1} \\ p \end{bmatrix} = \begin{bmatrix} RHS_u^{n-1,n} \\ RHS_v^{n-1,n} \\ RHS_w^{n-1,n} \\ RHS_\theta^{n-1,n} \\ 0 \end{bmatrix}, \quad (2.7)$$

where $H_u = H_v = H_w = Gr^{-0.5} \Delta - I/\Delta t$ and $H_\theta = Pr^{-1} Gr^{-0.5} \Delta - I/\Delta t$ are the Helmholtz operators for the scalar momentum and the energy equations, respectively, I is the identity operator, Δ is the Laplacian operator, and $\nabla^x, \nabla^y, \nabla^z$ are the first derivatives with respect to the x, y and z coordinates, respectively. The discrete differential operators in the LHS of Eq. (2.7) can contain different boundary conditions, and therefore for the general case, $H_u \neq H_v \neq H_w$ and $\nabla_u^x \neq \nabla_v^y, \nabla_v^y \neq \nabla_w^z, \nabla_w^z \neq \nabla_p^z$.

2.2.3. Immersed boundary method (IBM): direct forcing approach

The IBM [40] was implemented for imposing the Dirichlet boundary conditions for the temperature and velocity fields at the spherical shell boundaries and the internal baffles. The IBM is not a standalone solver, rather, it requires a ‘‘driver’’ with which to be combined and its

implementation should be perceived as a philosophy of enforcing boundary conditions. In principle, such a “driver” can be any time-marching solver, whose efficiency is typically boosted by choosing a computational domain of rectangular/prismatic shape, and by utilizing a structured grid for spatial discretization of the NS and energy equations. It should be noted that in the present implementation, the immersed bodies must neither intersect nor touch each other, imposing that the minimal distance between the two adjacent immersed boundaries is at least a size of a single grid cell. In the present formulation, the flow within the differentially heated spherical shell is an integral part of a more general natural convection flow within the whole cube, including also the outer ($R > R_o$), and the inner ($R < R_i$) regions (see Fig. 2.1). The flow was simulated by applying no-slip boundary conditions at all the cube faces, which were held at a constant temperature T_c (the same temperature of the external boundary of the spherical shell). In the present work, only the results relevant to the spherical shell region are discussed. Below, we detail the IBM formulation implemented in the present study.

Fig. 2.2 shows the setup of a typical spatial discretization implemented on a staggered grid.

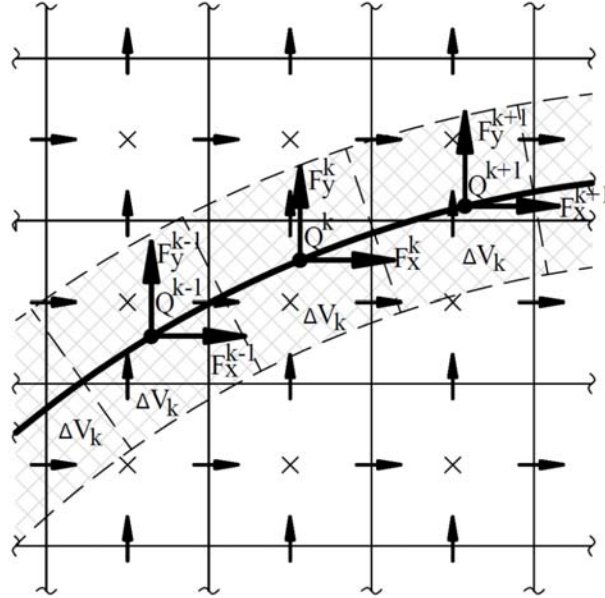


Figure 2.2. A schematic staggered grid discretization of a two-dimensional computational domain D , with a segment of immersed boundary of a body B . A virtual shell, whose thickness is equal to the grid cell width, is shaded. The horizontal and vertical arrows (\rightarrow, \uparrow) represent the discrete velocity locations, u_i and v_i respectively. Pressure p_j and temperature T_j are applied at the center of each cell designated by (\times). Lagrangian points ($\epsilon_k, \eta_k, \epsilon_k$) along ∂B are shown as black dots (\cdot), where volumetric boundary forces $\mathbf{F}_k (F_x, F_y, F_z)$ and volumetric boundary heat fluxes Q_k are applied.

The grid is characterized by offset velocity, temperature and pressure fields. An arbitrary immersed object B , within a computational domain D , (whose geometry does not, in general, have to conform to the underlying spatial grid) is represented by the surface ∂B , determined by a set of Lagrangian points \mathbf{X}_k . The same distance between neighboring points approximately equal to the grid size should be preserved to provide high accuracy [41].

We next associate a discrete volume dV_k with each Lagrangian point \mathbf{X}_k , such that an ensemble of these volumes forms a thin shell with a thickness equal to the width of the grid cell. At the Lagrangian points, appropriate surface forces \mathbf{F}_k , and heat fluxes Q_k , are applied to enforce the non-slip velocity and the Dirichlet temperature boundary conditions along, ∂B . Since the location of the Lagrangian boundary points does not necessarily coincide with the underlying spatial discretization, regularization and interpolation operators must be defined to convey information about the immersed body in both directions. The regularization operator, R , smears volumetric forces, \mathbf{F}_k , and heat fluxes Q_k , on the nearby computational domain, while the I interpolation operator acts in the opposite direction and imposes non-slip/thermal boundary conditions on the points located on the body surface :

$$R(\mathbf{F}_k(\mathbf{X}_k), Q_k(\mathbf{X}_k)) = \int_S (\mathbf{F}_k(\mathbf{X}_k), Q_k(\mathbf{X}_k)) \cdot \delta(\mathbf{x}_i - \mathbf{X}_k) dV_{Sk} \quad (2.8)$$

$$I(\mathbf{u}(\mathbf{x}_i), \theta(\mathbf{x}_i)) = \int_\Omega (\mathbf{u}(\mathbf{x}_i), \theta(\mathbf{x}_i)) \cdot \delta(\mathbf{x}_i - \mathbf{X}_k) dV_{\Omega i} \quad (2.9)$$

where S corresponds to all cells belonging to the immersed body surface, Ω corresponds to a group of flow cells located in the close vicinity to the immersed body surface, dV_{Sk} corresponds to the infinitesimal volume surrounding each Lagrangian point k , and $dV_{\Omega i}$ is the volume of the corresponding flow cell, whose velocity and temperature values are explicitly involved in enforcing boundary conditions at point k of the immersed body. Convolution with the Dirac delta function are used to facilitate the exchange of information to and from ∂B . Among the variety of discrete delta functions available, the function described by Roma et al. [42], specifically designed for use on staggered grids where even/odd de-coupling does not occur, was chosen. This delta function was successfully utilized in a number of previous studies [38,41-43].

$$d(r) = \begin{cases} \frac{1}{6\Delta r} \left[5 - 3\frac{|r|}{\Delta r} - \sqrt{-3\left(1 - \frac{|r|}{\Delta r}\right)^2 + 1} \right] & \text{for } 0.5\Delta r \leq |r| \leq 1.5\Delta r \\ \frac{1}{3\Delta r} \left[1 + \sqrt{-3\left(\frac{|r|}{\Delta r}\right)^2 + 1} \right] & \text{for } |r| \leq 0.5\Delta r \\ 0 & \text{otherwise} \end{cases} \quad (2.10)$$

where Δr is the cell width in the r direction. The discrete delta function $d(r)$ is supported over only three cells which comprised of an advantage for computational efficiency. The discrete form of regularization and interpolation operators for the 3D domain are governed by

$$(\mathbf{f}_i, q_i) = \Delta x^3 \sum_k (\mathbf{F}_k, Q_k) \cdot d(\epsilon_k - x_i) \cdot d(\eta_k - y_i) \cdot d(\zeta_k - z_i) \quad (2.11)$$

$$(\mathbf{U}_k, \Theta_k) = \Delta x^3 \sum_i (\mathbf{u}_i, \theta_i) \cdot d(x_i - \epsilon_k) \cdot d(y_i - \eta_k) \cdot d(z_i - \zeta_k) \quad (2.12)$$

where \mathbf{f}_i, q_i are the discrete volumetric force and heat source defined on the staggered grid (x_i, y_i, z_i) , and \mathbf{U}_k, Θ_k are the discrete boundary velocity and temperature defined at the k -th Lagrangian point $(\epsilon_k, \eta_k, \zeta_k)$.

Among the vast variety of existing pressure–velocity segregated solvers, the code recently developed and parallelized by Vitoshkin and Gelfgat [38] was chosen. The system of governing equations is solved using a SIMPLE method implementing a segregated approach. The linear system solver implements an algorithm based on the tensor product factorization (TPF) method, combined with the Thomas solver (TPT).

The direct forcing method approximates the boundary force \mathbf{F}^* , and volumetric heat flux Q^* , for rigid bodies with an intermediate predicted velocity field \mathbf{u}^* , initially calculated by ignoring the presence of the immersed body. The forces at Lagrangian points are calculated explicitly:

$$\mathbf{F}^*(\mathbf{X}_k, t^n) = \frac{\mathbf{U}^\Gamma(\mathbf{X}_k, t^n) - \mathbf{U}^*(\mathbf{X}_k, t^n)}{\Delta t}, \quad (2.13)$$

where \mathbf{U}^* represents the values of the boundary velocity obtained by interpolation of the nearby predicted velocity field on the immersed body surface, and \mathbf{U}^Γ corresponds to the preset boundary velocity (which is zero for the stationary boundary). The calculated \mathbf{F}^* is smeared over the volumes of the computational domain using the regularization operator. The obtained discrete volumetric forces \mathbf{f}^* enter as sources into the momentum equations:

$$\frac{\mathbf{u}^* - \mathbf{u}^n}{\Delta t} + (\mathbf{u}^n \cdot \nabla) \mathbf{u}^n - \mathbf{f}^* = -\nabla p + \sqrt{\frac{Pr}{Ra}} \nabla^2 \mathbf{u}^* + \theta^{n+1} \vec{e}_z \quad (2.14)$$

The algorithm is finalized by the standard projection-correction step, which includes the solution of the Poisson equation yielding the fields of corrected pressure and divergence free velocity vector. The boundary temperature values Θ^Γ of the surface of the immersed body are enforced by:

$$Q^*(\mathbf{X}_k, t^n) = \frac{\Theta^\Gamma(\mathbf{X}_k, t^n) - \Theta^*(\mathbf{X}_k, t^n)}{\Delta t}, \quad (2.15)$$

where the temperature of the Lagrangian points Θ^* is an interpolation of the intermediate temperature field θ^* , initially computed by ignoring the presence of the immersed body, and Q^* is a non-dimensional volumetric heat source, subsequently smeared over adjacent volumes by a regularization operator Eq. (2.11). As a result, the regularized volumetric Eulerian heat source q^* enters as a source into the corresponding energy equations:

$$\frac{\theta^{n+1} - \theta^n}{\Delta t} + (\mathbf{u}^n \cdot \nabla)\theta^n - q^* = \frac{1}{\sqrt{PrRa}} \nabla^2 \theta^{n+1} \quad (2.16)$$

It should be emphasized that the source/sink q^* value is relevant only if the preset Dirichlet or Neumann boundary conditions have to be enforced (i.e., in the presence of a thermally active immersed surface). If the immersed body is exposed only to convective flow and does not actively emit/absorb the heat by itself, then only non-slip boundary conditions are enforced on the immersed surface. In this case, a zero value is assigned to the q^* term appearing in Eq. (2.16). Formally, this imposes zero thermal resistance in the direction normal to the body surface, in accordance with the assumptions typically treating the internal baffle as an idealized zero thickness surface. Note also that due to the stationary boundaries, the interpolation/regularization operators can be pre-computed for each prescribed immersed surface: there is no need to employ a delta function at each time step, since it will yield the same result, thereby considerably decreasing the computational effort.

Next we define the Nu Nusselt number as a ratio of convective to conductive fluxes. Utilizing the same scaling as in Eqs. (2.1)–(2.3), the non-dimensional heat flux from the infinitesimal immersed surface is defined as:

$$\frac{\partial \Theta^*}{\partial \hat{n}} = \Delta x \sqrt{PrRa} Q^* \quad (2.17)$$

where Q^* is defined in Eq. (2.15). The heat flux values averaged over the entire surface are then used for calculation of the Nu numbers at the inner Nu_i , and outer Nu_o boundaries of the spherical shell:

$$Nu_i = \frac{1}{\pi D_i D_o} \left(\overline{\frac{\partial \Theta^*}{\partial \hat{n}}} \right) A_i \quad (2.18)$$

$$Nu_o = \frac{1}{\pi D_i D_o} \left(\overline{\frac{\partial \Theta^*}{\partial \hat{n}}} \right) A_o \quad (2.19)$$

2.3. “Smart” thermal insulation – concept and theoretical background

In this section, the numerical methodology, used for establishing, implementation and verification of the concept of "smart" thermo-insulation, is presented. The concept of "smart" thermo-insulation comprises heterogeneous porous material whose spatial pattern is intelligently fine-tuned to the given engineering configuration. The porous medium is modelled by unconnected packed beds consisting of equisized cylindrical cylinders. The concept of smart thermal insulation is formally established by utilizing the linear stability analysis of 2D natural convection flows augmented by the immersed boundary functionality. The results obtained by the 2D linear stability analysis were subsequently validated by performing 3D time integration of NS and energy equations, utilizing the algorithm presented in the previous section.

The implemented numerical methodology, based on the implicit formulation of the IB method and a fully pressure-velocity coupled approach, incorporates three solvers: a time marching solver for the time integration of the NS equations (Section 2.3.2); a steady-state solver based on the full Newton iteration (Section 2.3.3); and a linear stability solver (Section 2.3.4) for calculating the necessary part of the whole spectrum of the flow by utilizing the Arnoldi iteration method. All three solvers are based on the previously developed fully pressure-velocity coupled direct (FPCD) solver [44, 49] briefly described in Section 2.3.1 for the sake of completeness.

2.3.1. Fully pressure-velocity coupled direct (FPCD)

We consider the 2D NS equations for isothermal incompressible flow:

$$\nabla \cdot \mathbf{u} = 0, \quad (2.20)$$

$$\frac{\partial \mathbf{u}}{\partial t} + (\mathbf{u} \cdot \nabla) \mathbf{u} = -\nabla p + \frac{1}{Re} \nabla^2 \mathbf{u}, \quad (2.21)$$

where $\mathbf{u}(u, v)$, p and Re are the non-dimensionalized velocity vector, the pressure field, and the Reynolds number, respectively. By applying a second order backward finite difference scheme for time discretization, Eqs. (2.20) , (2.21) can be rewritten as:

$$\nabla \cdot \mathbf{u}^{n+1} = 0, \quad (2.22)$$

$$\left[\frac{1}{Re} \nabla^2 \mathbf{u} - \frac{3}{2\Delta t} \mathbf{u} \right]^{n+1} - \nabla p = \left[(u \cdot \nabla)u - \frac{2}{\Delta t} \mathbf{u} \right]^n + \frac{1}{2\Delta t} \mathbf{u}^{n-1}. \quad (2.23)$$

Note that all the non-linear terms are taken from the previous time step and moved to the right hand side (RHS) of Eqs. (2.22), (2.23). The system of vector Eqs. (2.22), (2.23) can be compactly rewritten in a block-matrix form as:

$$\begin{bmatrix} H_u & 0 & -\nabla_p^x \\ 0 & H_v & -\nabla_p^y \\ \nabla_u^x & \nabla_v^y & 0 \end{bmatrix} \begin{bmatrix} \mathbf{u}^{n+1} \\ \mathbf{v}^{n+1} \\ p \end{bmatrix} = \begin{bmatrix} RHS_u^{n-1,n} \\ RHS_v^{n-1,n} \\ 0 \end{bmatrix} \quad (2.24)$$

where ∇^x and ∇^y are the first derivatives with respect to the x and y coordinates, respectively, $H = \frac{1}{Re} \Delta - 3I/2\Delta t$ are the corresponding Helmholtz operators acting on u and v velocity components, I is the identity operator and ∇ is the Laplacian operator. The lower indices correspond to the scalar fields on which an operator acts. The left hand side (LHS) of Eqs. (2.24), known as the Stokes operator, is further discretized with a standard staggered mesh second-order conservative finite-volume formulation [45]. Non-linear terms, moved to the RHS of Eqs. (2.24), are approximated by the conservative central differencing scheme to exclude the appearance of artificial viscosity (see Ref. [49] for the discretization details). Following Ref. [44, 49] the fully pressure-velocity coupled solution of Eqs. (2.24) can be obtained by LU factorization of the Stokes operator, with a set of suitable boundary conditions for all the velocity components and a single Dirichlet reference point for the pressure field. The discrete Stokes operator remains unchanged during the solution, reducing the time integration of the NS equations to two backward substitutions at each time step. The high efficiency of the above approach (see Ref. [49] for the characteristic computational times) is achieved by utilizing a modern multifrontal direct solver for sparse matrices (MUMPS), exploiting the sparseness of the discrete Stokes operator at both LU factorization and back substitution stages. The FPCD approach formulated in Eqs. (2.24) can be straightforwardly adjusted to the simulation of natural convection flows, with buoyancy effects being introduced by the Boussinesq approximation and governed by:

$$\nabla \cdot \mathbf{u} = 0, \quad (2.25)$$

$$\frac{\partial \mathbf{u}}{\partial t} + (\mathbf{u} \cdot \nabla) \mathbf{u} = -\nabla p - Gr^{-0.5} \nabla^2 \mathbf{u} + \theta \vec{e}_y, \quad (2.26)$$

$$\frac{\partial \theta}{\partial t} + (\mathbf{u} \cdot \nabla) \theta = Pr^{-1} Gr^{-0.5} \nabla^2 \theta. \quad (2.27)$$

where $\mathbf{u}(u, v)$, θ and p correspond to the non-dimensionalized velocity, the temperature and the pressure fields respectively, Gr is the Grashof number, Pr is the Prandtl number, and \vec{e}_z is the unit vector in the opposite direction to gravity. Discretizing the time by a second-order backward finite difference scheme leads to:

$$\nabla \cdot \mathbf{u}^{n+1} = 0, \quad (2.28)$$

$$\left[Gr^{-0.5} \nabla^2 \mathbf{u} - \frac{3}{2\Delta t} \mathbf{u} + \theta \vec{e}_y \right]^{n+1} - \nabla p = \left[(\mathbf{u} \cdot \nabla) \mathbf{u} - \frac{2}{\Delta t} \mathbf{u} \right]^n + \frac{1}{2\Delta t} \mathbf{u}^{n-1}, \quad (2.29)$$

$$\left[Pr^{-1} Gr^{-0.5} \nabla^2 \theta - \frac{3}{2\Delta t} \theta \right]^{n+1} = \left[(\mathbf{u} \cdot \nabla) \theta - \frac{2}{\Delta t} \theta \right]^n + \frac{1}{2\Delta t} \theta^{n-1}. \quad (2.30)$$

Then, using the same notations as for Eqs. (2.24), the compact block-matrix form of the vector Eqs. (2.29), (2.30) reads:

$$\begin{bmatrix} H_u & 0 & 0 & -\nabla_p^x \\ 0 & H_v & \vec{e}_y & -\nabla_p^y \\ 0 & 0 & H_\theta & 0 \\ \nabla_u^x & \nabla_v^y & 0 & 0 \end{bmatrix} \begin{bmatrix} \mathbf{u}^{n+1} \\ v^{n+1} \\ \theta^{n+1} \\ p \end{bmatrix} = \begin{bmatrix} RHS_u^{n-1,n} \\ RHS_v^{n-1,n} \\ RHS_\theta^{n-1,n} \\ 0 \end{bmatrix} \quad (2.31)$$

where $H_u = H_v = Gr^{-0.5} \Delta - 3I/2\Delta t$ are the Helmholtz operators for the scalar momentum equations and for the energy equation $H_\theta = Pr^{-1} Gr^{-0.5} \Delta - 3I/2\Delta t$, I is the identity operator, Δ is the Laplacian operator and ∇^x, ∇^y are the first derivatives with respect to x and y coordinates, respectively. The discrete differential operators in the LHS of Eq. (2.24) and (2.31) can contain different boundary conditions, and therefore for the general case $H_u \neq H_v$ and $\nabla_u^x \neq \nabla_p^x, \nabla_v^y \neq \nabla_p^y$.

2.3.2. Implicit immersed boundary FPCD time stepper

The discrete pressure p appearing in Eqs. (2.24, 2.31) does not actively participate in time propagation, and therefore can be viewed as the Lagrange multiplier that constrains the solenoidal velocity. It is therefore reasonable to augment the existing Stokes operators Eqs. (2.24, 2.31) with the IB functionality by adding an additional set of Lagrange multipliers to enforce the appropriate

boundary conditions at the Lagrangian points. Formally, the extended block-matrix form of the Stokes operator for 2D isothermal incompressible flow (see Eqs. (2.24)) is formulated as:

$$\begin{array}{ccc|cc} \left[\begin{array}{ccc} H_u & 0 & -\nabla_p^x \\ 0 & H_v & -\nabla_p^y \\ \nabla_u^x & \nabla_v^y & 0 \end{array} \right] & \begin{array}{cc} R_{F_x} & 0 \\ 0 & R_{F_x} \end{array} & \begin{array}{c} u^{n+1} \\ v^{n+1} \\ p \\ F_x \\ F_y \end{array} & = & \begin{array}{c} RHS_u^{n-1,n} \\ RHS_v^{n-1,n} \\ 0 \\ U_b \\ V_b \end{array} \end{array} \quad (2.32)$$

Here, the vertical and horizontal dashed lines separate between the "original" Stokes operator, located at the top left corner of the matrix, and the additional entries related to the embedded immersed boundary functionality. These additional entries can be formally divided into two types. The first type corresponds to the "weights" of the unknown non-dimensional volumetric forces F_x and F_y , obtained by applying the regularization operator R smearing the forces over the vicinity of the Lagrangian points. The second type corresponds to the "weights" of the Eulerian velocity components. To precisely impose no-slip boundary conditions, the sum of the above "weights," each multiplied by its Eulerian velocity component, should be equal to the velocities U_b and V_b of the corresponding Lagrangian points. In other words, entries of the second type are nothing more than the additional equations necessary to achieve closure of the whole system of Eqs. (2.32), after the unknowns F_x and F_y have been added. It should be noted that as a result of the utilization of the same Dirac delta functions (Eq. 2.10) in both the interpolation I and R operators, and the uniform staggered grid in the near vicinity of the immersed body surface, the interpolation and regularization operators are transposed to each other, $R_F = I_u^T$. Note also that for all rigid stationary immersed bodies, the values of U_b and V_b are all equal to zero and the extended Stokes operator in Eqs. (2.32) does not vary in time. As a result, LU factorization of the extended Stokes operator should be performed only once at the beginning of the computational procedure. For moving/deforming bodies, the location of the Lagrangian points is updated at each time step, requiring modification of the extended Stokes operator (see Eqs. (2.32)) with its subsequent LU factorization. The factorization can be efficiently performed on a massively parallel machine, taking advantage of the high scalability parallelization built-in to the MUMPS solver [47].

Using the same notations as for Eqs. (2.32), an extended immersed boundary formulation for the natural convection flow can be written as:

$$\begin{bmatrix}
H_u & 0 & 0 & -\nabla_p^x & R_{F_x} & 0 & 0 \\
0 & H_v & \vec{e}_y & -\nabla_p^y & 0 & R_{F_y} & 0 \\
0 & 0 & H_\theta & 0 & 0 & 0 & R_Q \\
\hline
\nabla_u^x & \nabla_v^y & 0 & 0 & 0 & 0 & 0 \\
I_u & 0 & 0 & 0 & 0 & 0 & 0 \\
0 & I_v & 0 & 0 & 0 & 0 & 0 \\
0 & 0 & I_\theta & 0 & 0 & 0 & 0
\end{bmatrix}
\begin{bmatrix}
u^{n+1} \\
v^{n+1} \\
\theta^{n+1} \\
p \\
F_x \\
F_y \\
Q
\end{bmatrix}
=
\begin{bmatrix}
RHS_u^{n-1,n} \\
RHS_v^{n-1,n} \\
RHS_\theta^{n-1,n} \\
0 \\
U_b \\
V_b \\
\Theta
\end{bmatrix}
\quad (2.33)$$

Similarly to the Eqs. (2.32), the "original" Stokes operator located at the top left corner of the block-matrix form is separated by the vertical and horizontal dashed lines from the immersed boundary entries. The R_Q entries correspond to the "weights" of the unknown, non-dimensional, volumetric heat sources smeared over the vicinity of the corresponding Lagrangian points by the regularization operator R , whereas the I_θ entries are the "weights" of the Eulerian temperatures, imposing Dirichlet boundary conditions at the neighboring Lagrangian points.

In most thermal problems, precise estimation of the average \overline{Nu} number is of significant practical importance and is particularly critical for the present implementation of the IB method, which relies on a uniform Cartesian grid. As a result, a further refining of the Eulerian grid adjacent to the immersed boundary for a more precise resolution of the thinnest boundary layers is not practical. An alternative way to obtain an accurate estimation of the Nu number is to express the unknown Lagrangian non-dimensional volumetric heat sources in terms of the temperature gradients in the direction normal to the immersed boundary as:

$$Q = \frac{1}{Pr\sqrt{Gr}} \frac{\partial\theta}{\Delta x \partial n}, \quad (2.34)$$

where $\Delta x = \Delta y$ is the dimension of the uniform Eulerian grid in the vicinity of the immersed surface. Following 0, the \overline{Nu} value averaged over the surface of the immersed body reads:

$$\overline{Nu} = \frac{1}{2} \left(\sum_{k=1}^M \frac{\partial\theta}{\partial n} \Delta x \right)_k, \quad (2.35)$$

where the local $\frac{\partial\theta}{\partial n}$ values at every point $1 \leq k \leq M$ of the immersed body are provided by the solution of Eqs. (2.33), reformatted in terms of the temperature gradients in the direction normal to the body surface.

2.3.3. Steady-state immersed boundary FPCD solver

The immersed boundary method incorporated into the pressure-velocity coupled direct solver is implemented similarly to the direct forcing approach by introducing R regularization, and I interpolation operators. However, contrary to the direct forcing approach, it does not need the prediction and correction steps at each time step. The values of boundary force \mathbf{F}^* and volumetric heat flux Q^* in Lagrangian points are implicitly obtained as a part of the overall solution. The steady state isothermal incompressible flow with an embedded immersed boundary functionality is governed by the following equations:

$$\nabla \cdot \mathbf{u} = 0, \quad (2.36)$$

$$(\mathbf{u} \cdot \nabla)\mathbf{u} + \nabla p + \frac{1}{Ra} \nabla^2 \mathbf{u} - R_{\mathbf{F}} = 0, \quad (2.37)$$

$$I(\mathbf{u}) - \mathbf{U}_b = 0 \quad (2.38)$$

where $R_{\mathbf{F}}$ and $I(\mathbf{u})$ are additional entries which resulted by applying regularization R and interpolation I operators. A second order backward finite difference scheme, and a standard staggered grid, second order, conservative finite-volume method, are utilized for the temporal and spatial discretizations respectively. Additional entries $R_{\mathbf{F}}$ and $I(\mathbf{u})$ introduced by the immersed boundary formulation are implemented by utilizing discrete Dirac delta functions (see Eq. 2.10). Equation (2.36-2.38) can be presented in block-matrix form:

$$\begin{bmatrix} J_x & 0 & J_p & R_{F_x} & 0 \\ 0 & J_y & J_p & 0 & R_{F_y} \\ J_u & J_v & 0 & 0 & 0 \\ I_u & 0 & 0 & 0 & 0 \\ 0 & I_v & 0 & 0 & 0 \end{bmatrix} \begin{bmatrix} \delta(u) \\ \delta(v) \\ \delta(p) \\ \delta(F_x) \\ \delta(F_y) \end{bmatrix} = - \begin{bmatrix} F_{n_x} - \sum_j R_j F_{j_x} \\ F_{n_y} - \sum_j R_j F_{j_y} \\ F_{n_p} \\ \sum_i I_i u_x - U_{b_x} \\ \sum_i I_i u_y - U_{b_y} \end{bmatrix}, \quad (2.39)$$

where J_x, J_y, J_u, J_v, J_p are parts of Jacobian \mathbf{J} of a system of momentum and continuity equations that does not include immersed boundary functionality, corresponding to discrete right hand sides $F_{n_x}, F_{n_y}, F_{n_p}$ calculated at the iteration n . The matrix is expanded by entries of R_{F_x}, R_{F_y} and I_u, I_v as a result of embedded, immersed boundary formulation. The immersed boundary entries also contribute to the right hand side of Eqs. (2.39). The volumetric forces F_j and interpolated velocities u_i , both calculated at the iteration n , are added to the corresponding right hand sides of the

momentum and interpolation equations. The index i corresponds to Eulerian points and index j corresponds to Lagrangian points.

Natural convection flow with an embedded, immersed boundary functionality is governed by

$$\nabla \cdot \mathbf{u} = 0, \quad (2.40)$$

$$(\mathbf{u} \cdot \nabla)\mathbf{u} + \nabla p - Gr^{-0.5}\nabla^2\mathbf{u} - \theta\vec{e}_z - R_F = 0, \quad (2.41)$$

$$(\mathbf{u} \cdot \nabla)\theta - Pr^{-1}Gr^{-0.5}\nabla^2\theta - R_Q = 0, \quad (2.42)$$

$$I(\mathbf{u}) - \mathbf{U}_b = 0, \quad (2.43)$$

$$I(\theta) - \Theta_b = 0. \quad (2.44)$$

The Buossinesq approximation is utilized for simulating the buoyancy effects. Similarly to the formulation of isothermal flow, operators R_F , R_Q , $I(\mathbf{u})$, and $I(\theta)$ are introduced by applying regularization R and interpolation I operators to address the impact of the immersed boundary on the velocity and temperature fields. Utilizing the same time and space discretization as for Eqs. (2.36-2.38), Eqs. (2.41-2.44) can be rewritten in a compact block-matrix form as:

$$\begin{bmatrix} J_x & 0 & 0 & J_p & R_{F_x} & 0 & 0 \\ 0 & J_y & \vec{e}_y & J_p & 0 & R_{F_y} & 0 \\ 0 & 0 & J_\theta & 0 & 0 & 0 & R_Q \\ J_u & J_v & 0 & 0 & 0 & 0 & 0 \\ I_u & 0 & 0 & 0 & 0 & 0 & 0 \\ 0 & I_v & 0 & 0 & 0 & 0 & 0 \\ 0 & 0 & I_\theta & 0 & 0 & 0 & 0 \end{bmatrix} \begin{bmatrix} \delta(u) \\ \delta(v) \\ \delta(\theta) \\ \delta(p) \\ \delta(F_x) \\ \delta(F_y) \\ \delta(Q) \end{bmatrix} = - \begin{bmatrix} F_{n_x} - \sum_j R_j F_x \\ F_{n_y} - \sum_j R_j F_y \\ F_{n_\theta} - \sum_j R_j Q \\ F_{n_p} \\ \sum_i I_{iu_x} - U_{b_x} \\ \sum_i I_{iu_y} - U_{b_y} \\ \sum_i I_{i\theta} - \Theta_b \end{bmatrix} \quad (2.45)$$

The iterative Newton-Raphson method is used to solve Eqs. (2.45).

2.3.4. Linear stability immersed boundary FPCD solver

Linear stability analysis of natural convection flow with an embedded, immersed, boundary functionality is detailed in the following. The present linear stability approach is based on the algorithm previously developed by Gelfgat [49]. The presently implemented method imposes no restrictions on either the number of bodies or their shape. However, it requires that the body boundaries do not touch or intersect, and that the minimal distance between the neighbouring

bodies is at least the size of a single grid cell. The linear stability eigenproblem of natural convection flow in the presence of an immersed body is formulated by assuming infinitesimally small perturbations in the form of $\{\tilde{\mathbf{u}}(x, y), \tilde{\theta}(x, y), \tilde{p}(x, y), \tilde{\mathbf{F}}(x, y), \tilde{Q}(x, y)\}e^{\lambda t}$ around the steady state flow \mathbf{U} , Θ , p , \mathbf{F} , Q as follows:

$$\lambda \tilde{\mathbf{u}} = -(\mathbf{U} \cdot \nabla) \tilde{\mathbf{u}} - (\tilde{\mathbf{u}} \cdot \nabla) \mathbf{U} - \nabla \tilde{p} + Gr^{-0.5} \nabla^2 \tilde{\mathbf{u}} - \tilde{\theta} \vec{e}_z - R_{\tilde{\mathbf{F}}}, \quad (2.46)$$

$$\lambda \tilde{\theta} = -(\mathbf{U} \cdot \nabla) \tilde{\theta} - (\tilde{\mathbf{u}} \cdot \nabla) \Theta + Pr^{-1} Gr^{-0.5} \nabla^2 \tilde{\theta} + R_{\tilde{Q}}, \quad (2.47)$$

$$\nabla \cdot \tilde{\mathbf{u}} = 0, \quad (2.48)$$

$$I(\tilde{\mathbf{u}}) = 0, \quad (2.49)$$

$$I(\tilde{\theta}) = 0, \quad (2.50)$$

Eqs. (2.46-2.50) rewritten in a block-matrix form is:

$$\lambda \mathbf{B} \begin{bmatrix} \tilde{\mathbf{u}} \\ \tilde{\theta} \\ \tilde{p} \\ \tilde{\mathbf{F}} \\ \tilde{Q} \end{bmatrix} = \mathbf{J} \begin{bmatrix} \tilde{\mathbf{u}} \\ \tilde{\theta} \\ \tilde{p} \\ \tilde{\mathbf{F}} \\ \tilde{Q} \end{bmatrix}, \quad (2.51)$$

where \mathbf{J} is the Jacobian matrix calculated from the RHS of Eqs. (2.46-2.50) and \mathbf{B} is the diagonal matrix whose diagonal elements corresponding to the values of $\tilde{\mathbf{u}}$, $\tilde{\theta}$ are equal to unity, whereas the diagonal elements corresponding to \tilde{p} , $\tilde{\mathbf{F}}$, \tilde{Q} are equal to zero. Since the discretization is performed on a structured staggered grid in the Cartesian coordinates system, the Jacobians \mathbf{J} of Eqs. (2.45) and (2.51) are equal. In linear stability analysis, we are interested in finding the critical value of control parameter Gr , Re numbers, at which the real part of λ (leading eigenvalue) is equal to zero, $Real(\lambda) = 0$. The solution is based on a standard Arnoldi iteration implemented within an open source ARPACK package, seeking the dominant eigenvalue (largest by modulus). However, the eigenproblem (2.51) cannot be directly transformed into a standard eigenproblem, since $det(\mathbf{B}) = 0$, therefore it is solved in a shift-invert mode.

$$(\mathbf{J} - \sigma \mathbf{B})^{-1} \mathbf{B} \begin{bmatrix} \tilde{\mathbf{u}} \\ \tilde{\theta} \\ \tilde{\rho} \\ \tilde{\mathbf{F}} \\ \tilde{\mathbf{Q}} \end{bmatrix} = \mu \begin{bmatrix} \tilde{\mathbf{u}} \\ \tilde{\theta} \\ \tilde{\rho} \\ \tilde{\mathbf{F}} \\ \tilde{\mathbf{Q}} \end{bmatrix}, \quad \mu = \frac{1}{\lambda - \sigma} \quad (2.52)$$

The dominant eigenvalue μ can be related to the leading eigenvalue λ when the approach is applied to the shift-invert problem, where σ is a complex shift. To converge, the approach requires from the complex shift σ to be close to the λ value, whose imaginary part $Im(\lambda)$ corresponds to the critical angular oscillating frequency, ω_{cr} . The value of ω_{cr} is either known in case of benchmark problems, or can be estimated by a series of successive numerical simulations of the slightly bifurcated flow.

The present linear stability approach extends the algorithm presented by Gelfgat [49], with an IB functionality. Theoretically, no specific restrictions are imposed either on the number of bodies or on their shape. However, the method requires that the body boundaries do not touch or intersect and that the minimal distance between neighboring bodies is at least the size of a single grid cell. The solution procedure is as follows. First, the steady state solution is calculated by the Newton method for the given value of the control parameter (Gr or Re numbers). Then, the linear stability analysis is performed by utilizing a shift-invert Arnoldi iteration (see Eqs. (2.52)). The corresponding eigenvalue problem is solved by a secant method, providing a precise value for the critical control parameter. The overall process requires numerous solutions of large systems of linear equations, which should be performed at each step of the Newton method and while building the Krylov basis for the Arnoldi iteration. Typically, no more than ten iterations are required for the calculation of the steady-state solution (by the Newton method), while the shift-invert Arnoldi iteration needs $O(10^4)$ iterations to converge, thus comprising the key issue determining the computational efficiency of the whole process.

Next, to efficiently implement the product of the operator $(\mathbf{J} - \sigma \mathbf{B})^{-1} \mathbf{B}$ by the vector $[\tilde{\mathbf{u}} \ \tilde{\theta} \ \tilde{\rho} \ \tilde{\mathbf{F}} \ \tilde{\mathbf{Q}}]^T$ required at each Arnoldi iteration step, we exploit the fact that the operator $(\mathbf{J} - \sigma \mathbf{B})^{-1} \mathbf{B}$ does not change during the building of the Krylov basis for the Arnoldi iteration (see Eqs. (2.52)). The product implementation is simply a solution \mathbf{X} of the linear system $(\mathbf{J} - \sigma \mathbf{B})\mathbf{X} = \mathbf{B}[\tilde{\mathbf{u}} \ \tilde{\theta} \ \tilde{\rho} \ \tilde{\mathbf{F}} \ \tilde{\mathbf{Q}}]^T$. By utilizing the direct solver MUMPS, the LU decomposition of the operator $(\mathbf{J} - \sigma \mathbf{B})$ is performed once at the beginning of the process, and then each vector of the Krylov

basis is obtained by just two subsequent back substitutions, whose complexity is comparable to that of matrix-vector multiplication. Note also that the overall performance is additionally boosted by being a $(\mathbf{J} - \sigma\mathbf{B})$ sparse matrix. At the end of the stage, we receive the leading eigenvalue λ and the leading eigenvectors of all flow fields are calculated.

Chapter 3

Results and Discussion

3.1. Chapter overview

In this chapter, the results obtained in the framework of the current study are presented and discussed. The first part of the study (Section 3.2) focuses on the analysis of 3D laminar natural convection flow in multi-layered spherical shells. The section includes an extensive verification study of the in-house solver acquired with IB functionality to perform the time integration of NS equations in the presence of immersed bodies of an arbitrary shape. The verification study includes comparison with the independent results available in the literature and grid independence analysis. The section presents results regarding characteristics of laminar natural convection flow inside multi-layered spherical shells with internal hot and external cold boundaries. An affect of adding zero-thickness internal baffles on the thermal efficiency and the flow characteristics of the flow developing in single- and multi-layered spherical shells was studied. Natural convection flow developing inside spherical shell configurations with non-equi-spaced, zero-thickness, internal baffles, were also discussed. The reported results also include the new $Nu - Ra$ correlation derived for equi-spaced, multi-layered, spherical shells.

The second part of the study (Section 3.2) presents results regarding implementation of the concept of “smart” thermally insulating materials. The results obtained by the linear stability analysis were favorably verified by comparison with the corresponding time integration results performed for the slightly bifurcated flow (both by obtained in-house developed solvers). The concept “smart” thermally insulating materials was extensively studied taking the configuration of a differentially heated 2D square cavity as a test bed. The pattern of thermally insulating material obtained by the linear stability analysis of 2D flow was subsequently validated for realistic 3D natural convection flow developing inside a differentially heated cubical cavity.

3.2. Multi-layered spherical shell²

3.2.1. Verification

Natural convection in a cubic enclosure with a sphere

The developed solver was first verified by simulating the natural convection flow developing in the presence of an isothermal hot sphere placed within a cubic container with isothermal cold walls. The flow is governed by the same non-dimensional NS Eqs. (2.1)–(2.3) as the original problem, the only difference being that all the length scales are normalized by the cube side length, d . The inner hot sphere is located on the vertical centerline of the cube, and its distance to the cube center is determined by the non-dimensional parameter $-0.25 \leq \delta \leq 0.25$, defined as $\delta = Z_c - Z_{sph}$, where Z_c and Z_{sph} are the non-dimensional Z coordinates corresponding to the centers of the cubic container and of the sphere, respectively [51]. All the results were obtained on a 200^3 uniform grid. Fig. 3.1 shows the flow characteristics in terms of the temperature distribution and projection of the path lines on a mid-plane cross section obtained for the $Ra = 10^4, 10^5, 10^6$ and $\delta = -0.25, 0, 0.25$ values. There is an excellent agreement between the characteristics of the presently computed flow and the previously published results [51] for the entire range of Ra and δ values. For all the Ra values, the flow at $\delta = -0.25$ is characterized by a clearly distinguished thermal plume rising up from the top of the sphere. The plume becomes less developed as δ increases, and the restricting effect of the top boundary on the rising up convective flow becomes more pronounced. All the configurations are characterized by the strong temperature gradients just below the sphere and close to the cube top boundary, indicating the existence of a thin boundary layers in these regions. When $\delta = 0.25$, the thermal plume, localized at the top half of the cube, is radially squeezed for all the Ra values, giving rise to the development of a thermally stratified region with almost zero velocities below the sphere. The spiral form of the flow path lines observed for all the configurations presented in Fig. 3.1 clearly indicate the 3D character of the flow, which is a consequence of the end-wall effects.

Table 3.1 compares between the presently obtained and the previously published [51] values of average Nu numbers. An acceptable agreement between the results is observed for the entire range of Ra numbers. The differences between the results grow up with increasing the Ra

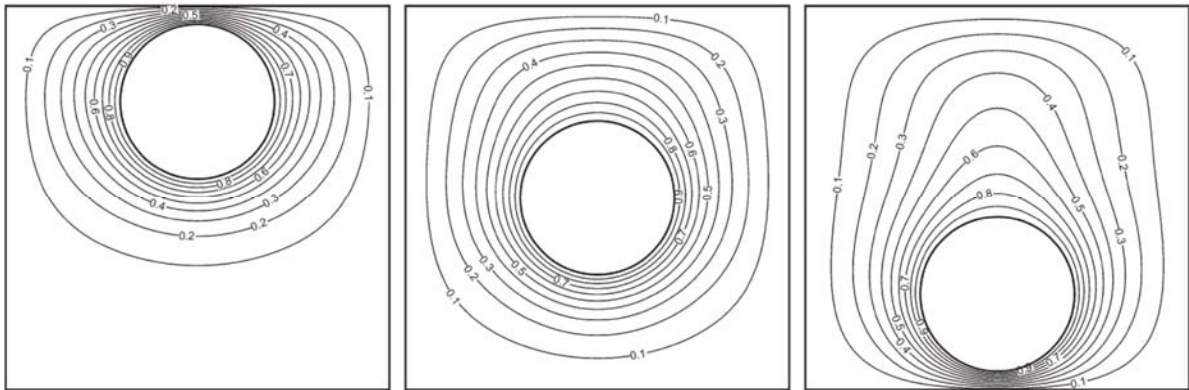
² This section is based on Y. Gulberg, Y. Feldman [39]

values, which can apparently be a consequence of different approaches utilized for calculation of the Nu numbers.

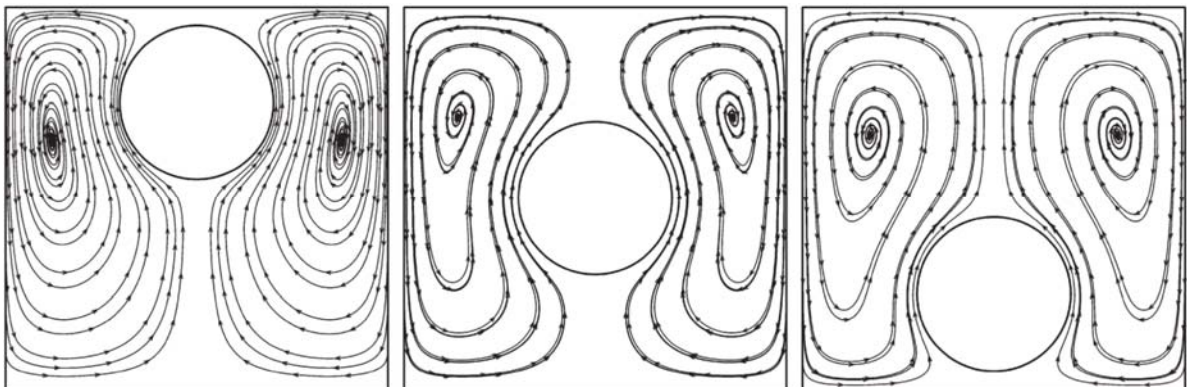
Table 3.1

Comparison between the present and the scanned [51] average Nu values obtained for the flow developing in the presence of an isothermal hot sphere placed within a cubic container with all isothermal cold walls.

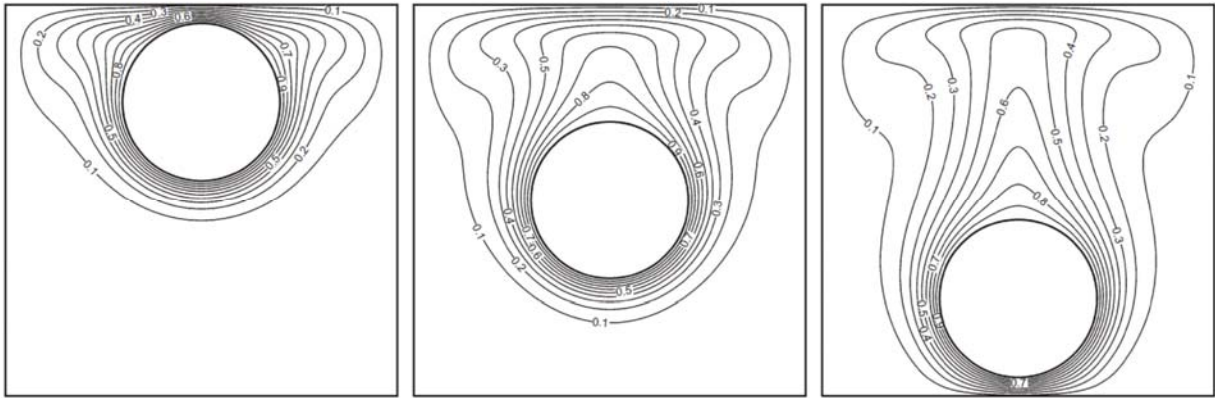
δ	$Ra = 10^4$		$Ra = 10^5$		$Ra = 10^6$	
	Ref. [51]	Present	Ref. [51]	Present	Ref. [51]	Present
-0.25	9.867	10.199	13.665	13.774	20.89	21.993
-0.2	8.843	9.117	12.931	13.058	20.631	21.862
-0.1	8.087	8.451	12.729	13.105	20.772	22.164
0	7.859	8.314	12.658	13.415	20.701	22.344
0.1	7.947	8.507	12.351	13.446	20.367	22.525
0.2	8.615	9.266	12.254	13.635	19.664	22.208
0.25	9.621	10.387	12.944	14.426	19.721	22.393



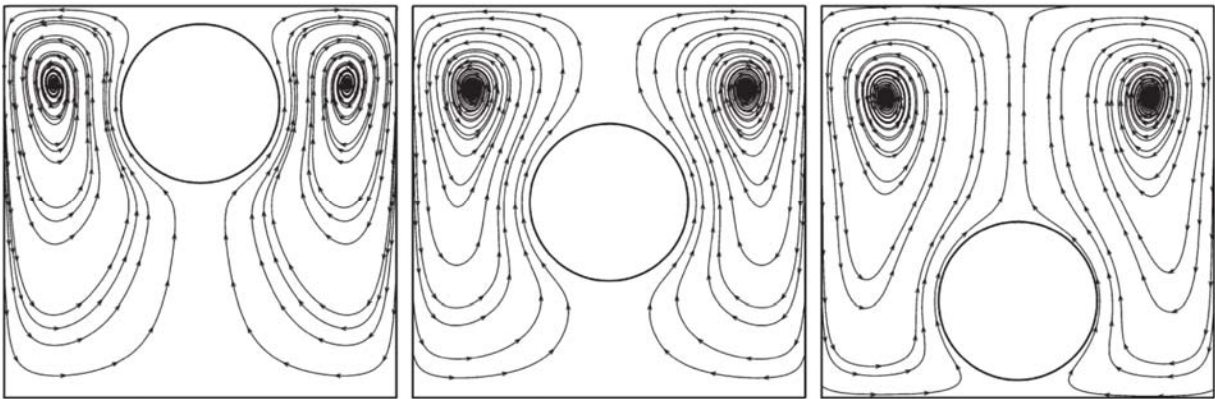
(a) Temperature distribution of the mid-plane cross section, $Ra = 10^4$



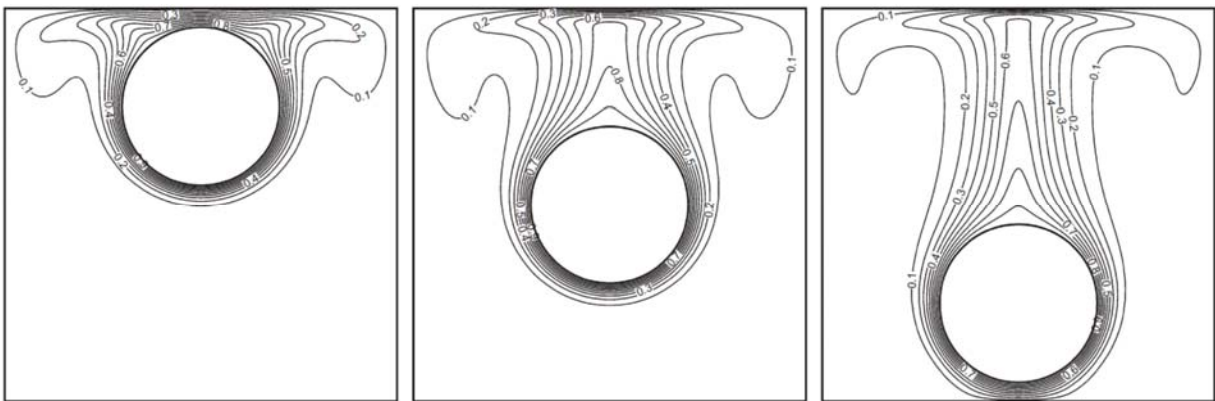
(b) Path lines projection on the mid-plane cross section, $Ra = 10^4$



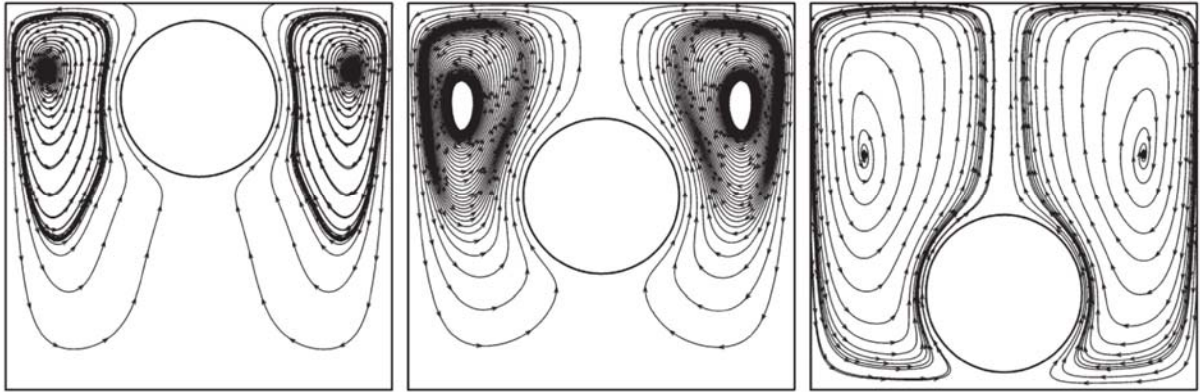
(c) Temperature distribution of the mid-plane cross section, $Ra = 10^5$



(d) Path lines projection on the mid-plane cross section, $Ra = 10^5$



(e) Temperature distribution of the mid-plane cross section, $Ra = 10^6$

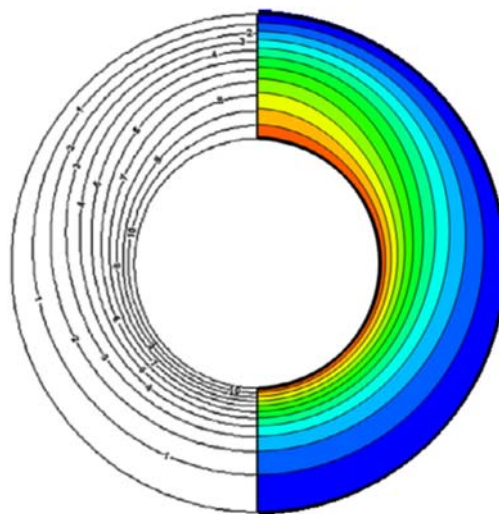


(f) Path lines projection on the mid-plane cross section, $Ra = 10^6$

Figure 3.1. Flow characteristics on a mid-plane cross section as a function of Ra number: temperature distribution and path lines projection obtained for the values of $\delta = -0.25, 0, 0.25$ on a 200^3 grid.

Natural convection in the spherical annuli – axi-symmetric flow

The results obtained for the flow inside the spherical annuli were also successfully verified by comparison with numerical data available in the literature. Fig. 3.2 presents a comparison between the axi-symmetric temperature fields provided by [52] for three different Ra numbers, and the corresponding results obtained in this study by fully three-dimensional simulations. There is a good qualitative and quantitative agreement between the corresponding temperature fields for the whole range of Ra numbers. Typical of steady laminar flows in spherical shells, the results obtained by the fully three-dimensional solver preserve the flow’s axi-symmetry.



(a)

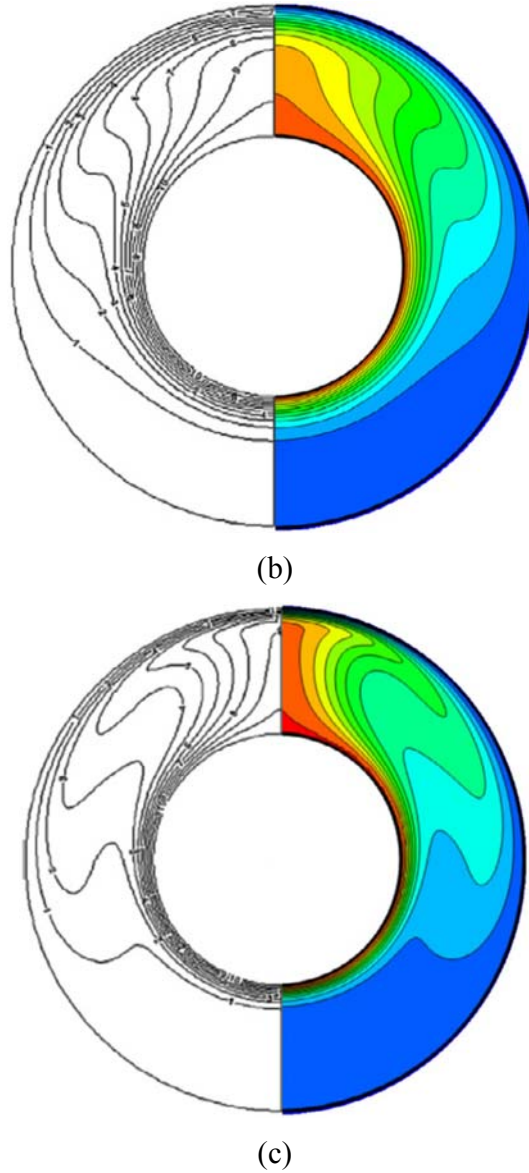


Figure 3.2. Comparison between the axi-symmetric temperature field provided by Dehghan and Masih [52], and the present results obtained by fully three-dimensional simulations for: (a) $Ra = 10^3$; (b) $Ra = 10^4$; (c) $Ra = 10^5$. The contour colors correspond to 10 equi-spaced values of temperature in the range of $0 < \theta < 1$.

Grid independence study

To perform a grid independence study, the natural convection flow was simulated inside a double-walled spherical shell (without internal baffles) on 200^3 and 300^3 uniform grids for $Ra = 10^3, 10^4, 10^5$. The results of all the velocity components and temperature were collected from the

control points located on the spherical shell center-lines, as shown in Fig. 3.3. For both grids, the flow characteristics were acquired at eight control points uniformly distributed along each centerline (four from each side of the center of spherical shell), as presented in Table 3.2. Most of the results obtained on the two grids are in excellent agreement. A deviation between the corresponding fields appears in the third decimal digit, as expected for the second order accuracy method. For all the cases, the axi-symmetry of the steady flow is clearly recognized by verifying the same values of the flow fields in the reflection symmetry points on the X and Y centerlines. Note also that zero ($O(10^{-6})$) values of the velocity components in the transverse direction were obtained for all the cases, additionally verifying an axi-symmetry of the obtained steady flow. Based on the performed grid independence analysis, the uniform 200^3 grid was chosen for further analysis.

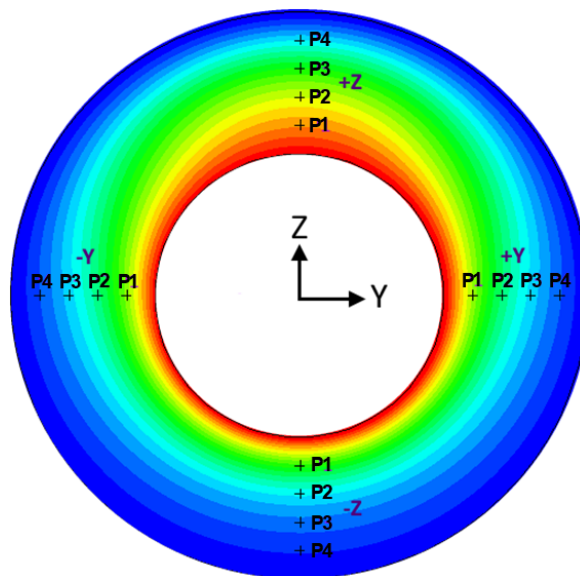


Figure 3.3. A scheme of location of control points.

Table 3.2

Flow characteristics along the spherical shell center-lines, all the velocity components (u_x , u_y , u_z) are multiplied by a factor of 10^3 .

$Ra = 10^3, Y = Z = 0, u_y = 0$						
X	200 ³ grid			300 ³ grid		
	u_x	u_z	θ	u_x	u_z	θ
-1.8	7.222	-187.2	0.101	7.667	-187.6	0.100
-1.6	17.17	-119.7	0.224	17.82	-119.4	0.223
-1.4	15.21	110.2	0.383	15.75	110.4	0.380
-1.2	3.893	306.6	0.627	4.087	309.5	0.623
1.2	-3.895	306.6	0.627	-4.088	309.5	0.623
1.4	-15.21	110.2	0.383	-15.75	110.4	0.380
1.6	-17.17	-119.6	0.224	-17.82	-119.4	0.223
1.8	-7.221	-187.2	0.100	-7.667	-187.6	0.100

$Ra = 10^3, X = Z = 0, u_x = 0$						
Y	200 ³ grid			300 ³ grid		
	u_y	u_z	θ	u_y	u_z	θ
-1.8	7.222	-187.2	0.100	7.668	-187.6	0.100
-1.6	17.17	-119.7	0.224	17.82	-119.4	0.223
-1.4	15.21	110.2	0.383	15.75	110.4	0.380
-1.2	3.894	306.6	0.627	4.088	309.5	0.623
1.2	-3.894	306.6	0.627	-4.088	309.5	0.623
1.4	-15.21	110.2	0.383	-15.75	110.4	0.380
1.6	-17.17	-119.6	0.224	-17.82	-119.4	0.223
1.8	-7.221	-187.2	0.100	-7.666	-187.6	0.100

$Ra = 10^3, X = Y = 0, u_x = u_y = 0$				
Z	200 ³ grid		300 ³ grid	
	u_z	θ	u_z	θ
-1.8	16.86	0.052	17.97	0.052
-1.6	55.70	0.127	56.86	0.125
-1.4	86.24	0.256	87.35	0.253
-1.2	63.45	0.522	64.99	0.515
1.2	69.87	0.851	71.39	0.853
1.4	133.7	0.709	136.2	0.713
1.6	120.3	0.518	123.9	0.526
1.8	47.62	0.259	50.74	0.266

Table 3.2 Continued

$Ra = 10^4, Y = Z = 0, u_y = 0$						
X	200 ³ grid			300 ³ grid		
	u_x	u_z	θ	u_x	u_z	θ
-1.8	28.66	-244.3	0.1049	29.49	-241.3	0.1029
-1.6	70.58	-161.7	0.1771	71.35	-160.7	0.1733
-1.4	73.28	69.33	0.2065	74.18	65.90	0.2022
-1.2	34.83	431.1	0.3731	35.74	426.2	0.3652
1.2	-34.84	431.1	0.3730	-35.74	426.2	0.3652
1.4	-73.27	69.34	0.2065	-74.18	65.86	0.2022
1.6	-70.58	-161.6	0.1771	-71.36	-160.67	0.1733
1.8	-28.66	-244.3	0.1049	-29.49	-241.3	0.1029

$Ra = 10^4, X = Z = 0, u_x = 0$						
Y	200 ³ grid			300 ³ grid		
	u_y	u_z	θ	u_y	u_z	θ
-1.8	28.66	-244.3	0.1049	29.49	-241.3	0.1029
-1.6	70.58	-161.7	0.1771	71.35	-160.7	0.1733
-1.4	73.27	69.34	0.2065	74.18	65.90	0.2022
-1.2	34.82	431.1	0.3731	35.74	426.2	0.3652
1.2	-34.84	431.0	0.3730	-35.74	426.2	0.3652
1.4	-73.28	69.33	0.2065	-74.19	65.86	0.2022
1.6	-70.59	-161.6	0.1771	-71.36	-160.6	0.1733
1.8	-28.66	-244.2	0.1049	-29.48	-241.3	0.1029

$Ra = 10^4, X = Y = 0, u_x = u_y = 0$				
Z	200 ³ grid		300 ³ grid	
	u_z	θ	u_z	θ
-1.8	9.253	0.0085	10.18	0.0079
-1.6	39.06	0.0216	39.81	0.0205
-1.4	79.05	0.0554	79.30	0.0535
-1.2	87.49	0.2298	88.17	0.2237
1.2	94.46	0.9346	93.41	0.9334
1.4	195.1	0.8938	193.3	0.8921
1.6	217.7	0.8590	217.2	0.8570
1.8	129.2	0.6856	131.9	0.6904

Table 3.2 Continued

$Ra = 10^5, Y = Z = 0, u_y = 0$						
X	200 ³ grid			300 ³ grid		
	u_x	u_z	θ	u_x	u_z	θ
-1.8	16.95	-239.2	0.174	17.89	-234.2	0.173
-1.6	11.77	-5.501	0.192	11.73	-5.251	0.187
-1.4	14.81	70.80	0.158	16.32	70.73	0.151
-1.2	28.21	223.1	0.189	29.39	211.1	0.179
1.2	-28.20	222.9	0.189	-29.39	211.1	0.179
1.4	-14.81	70.733	0.158	-16.36	70.72	0.151
1.6	16.95	-239.2	0.174	17.89	-234.2	0.173
1.8	11.77	-5.501	0.192	11.73	-5.251	0.187

$Ra = 10^5, X = Z = 0, u_x = 0$						
Y	200 ³ grid			300 ³ grid		
	u_y	u_z	θ	u_y	u_z	θ
-1.8	16.965	-239.3	0.1740	17.899	-234.3	0.1729
-1.6	11.781	-5.533	0.1922	11.728	-5.234	0.1873
-1.4	14.803	70.75	0.1580	16.315	70.75	0.1513
-1.2	28.183	223.1	0.1892	29.394	211.2	0.1789
1.2	-28.215	223.0	0.1891	-29.397	211.2	0.1789
1.4	-14.808	70.86	0.1580	-16.320	70.73	0.1513
1.6	-11.776	-5.461	0.1922	-11.737	-5.238	0.1873
1.8	-16.964	-239.3	0.1740	-17.901	-234.3	0.1729

$Ra = 10^5, X = Y = 0, u_x = u_y = 0$				
Z	200 ³ grid		300 ³ grid	
	u_z	θ	u_z	θ
-1.8	-1.418	0.0019	0.151	0.0014
-1.6	7.026	0.0045	9.324	0.0035
-1.4	28.54	0.0100	30.59	0.0082
-1.2	59.96	0.0552	60.56	0.0506
1.2	173.7	0.9439	172.1	0.9444
1.4	363.1	0.9116	363.2	0.9125
1.6	402.9	0.8880	404.8	0.8891
1.8	264.8	0.8688	266.7	0.8699

Verification of the average Nu values

Precise estimation of the average Nu number comprises an essential criterion for verification of any numerical solver and is particularly critical for the IBM. The IBM relies on a uniform Cartesian grid, which does not allow further local stretching for a more precise resolution of the thinnest boundary layers. In this case, a more precise estimation of the Nu values is achieved by utilizing the law of conservation of heat flux (see Eq. (2.17)), rather than simply calculating the near-surface temperature gradient. A comparison between the available and our estimated Nu values for various spherical shell configurations, and different Ra numbers corresponding to steady-state flow, is summarized in Table 3.3. It is remarkable that for steady state flow, an acceptable agreement in Nu values is observed for the fully three-dimensional and axi-symmetric simulations. The picture is, however, quite different for unsteady, non-axi-symmetric flows, which (for the same operating conditions) are characterized by an enhanced heat flux compared to the corresponding axi-symmetric idealizations (see Table 3.4). At the same time, there is good agreement for all the Nu when compared with the recent results of Feldman and Colonius [3], all obtained by a three-dimensional analysis. In all cases, the same Nu values (up to the third decimal digit) were obtained for the external and internal shell boundaries by their time and space averaging, after an asymptotic, quasi-state solution was reached. This finding verifies the heat flux conservation over the entire computational domain. Note also an excellent agreement between the Nu values obtained on 200^3 and 300^3 grids, which can be seen as additional justification of the grid independence of the obtained results.

Table 3.3

Average (in space) Nu numbers for steady laminar axi-symmetric flow.

ϕ	Ra	Present(200^3 grid)	Present(300^3 grid)	Ref. [3]	Ref. [53]	Ref. [52]	Ref. [51]
0.5	1.0×10^3	1.126	1.120	1.104	1.099	1.1310	1.1021
0.5	1.0×10^4	1.993	1.987	1.9665	1.973	1.9495	1.9110
0.5	1.0×10^5	3.461	3.452	3.4012	3.489	3.4648	3.3555
0.667	1.0×10^3	1.069	1.081	1.04825	1.001	1.00115	
0.833	1.0×10^3	1.061	1.053	1.011	1.0	1.0018	

Table 3.4

Average (in time and in space) Nu numbers for unsteady 3D flow. Results reported for axisymmetric flow are given in parentheses.

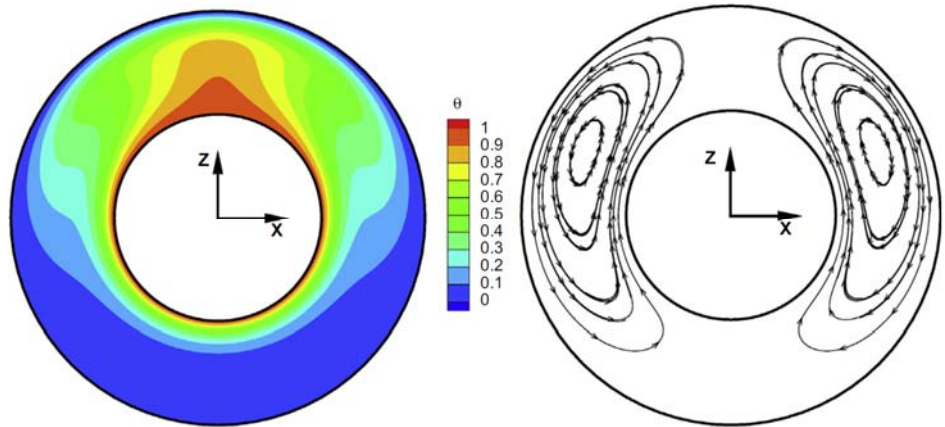
ϕ	Ra	Present(200 ³ grid)	Present(300 ³ grid)	Ref. [3]	Ref. [53]	Ref. [52]
0.667	1.0×10^4	1.811	1.826	1.793	1.073	1.07138
0.667	1.0×10^5	3.321	3.375	3.243	1.917	1.89756
0.833	1.0×10^4	1.620	1.713	1.6523	1.001	1.0028
0.833	1.0×10^5	3.274	3.276	3.0678	1.008	1.0100

3.2.2. Discussion

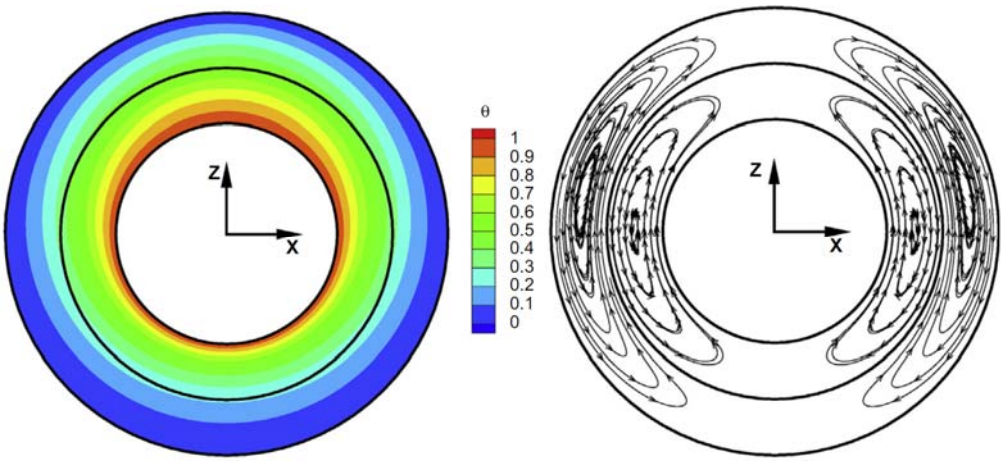
The IBM enables efficient manipulation of the orientation of the internal layers of the spherical shell so as to achieve optimized thermal insulation. Among the large number of possibilities, the present study focuses on an investigation of equi-spaced/non-equi-spaced concentric and horizontally/vertically, eccentric orientations of the internal layers. All the numerical simulations were performed for a spherical shell characterized by $\phi = D_i/D_o = 0.5$ on a 200³ uniform grid.

Concentric equi-spaced internal layers

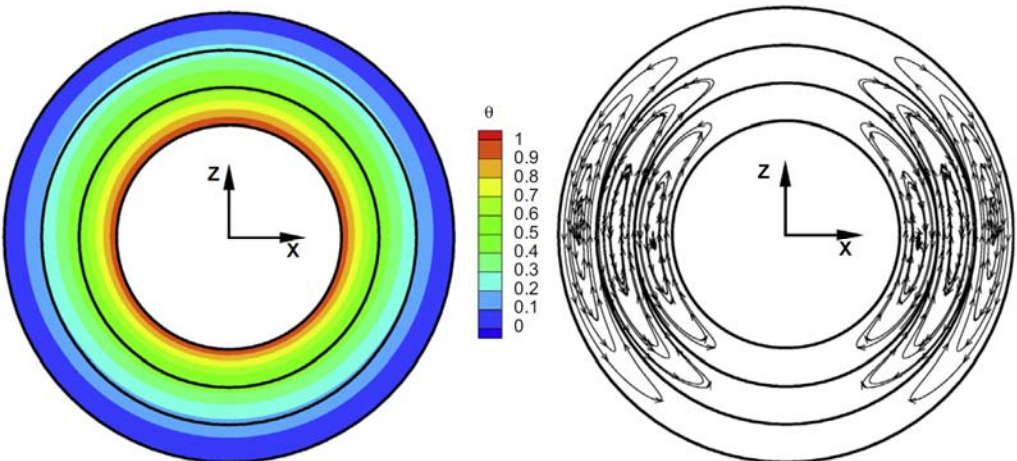
As the first step, the natural convection flow inside a spherical shell with up to four concentric, equi-spaced internal layers was investigated. Following the recent works of Samanta et al. [1], Feldman et al. [2], and Feldman and Colonius [3], zero wall thickness was assumed for all the internal baffles, providing zero thermal resistance in the radial direction. In addition, non-slip boundary conditions for all the velocity components were imposed on all internal baffles and external boundaries of the shell. Typical steady state temperature distributions, along with the flow path lines obtained in a mid cross-section of the spherical shells with up to four equi-spaced, internal layers for moderate $Ra = 10^4$, and high $Ra = 5 \times 10^5$ Rayleigh numbers, are shown in Figs. 3.4 and 3.5 respectively.



(a)



(b)



(c)

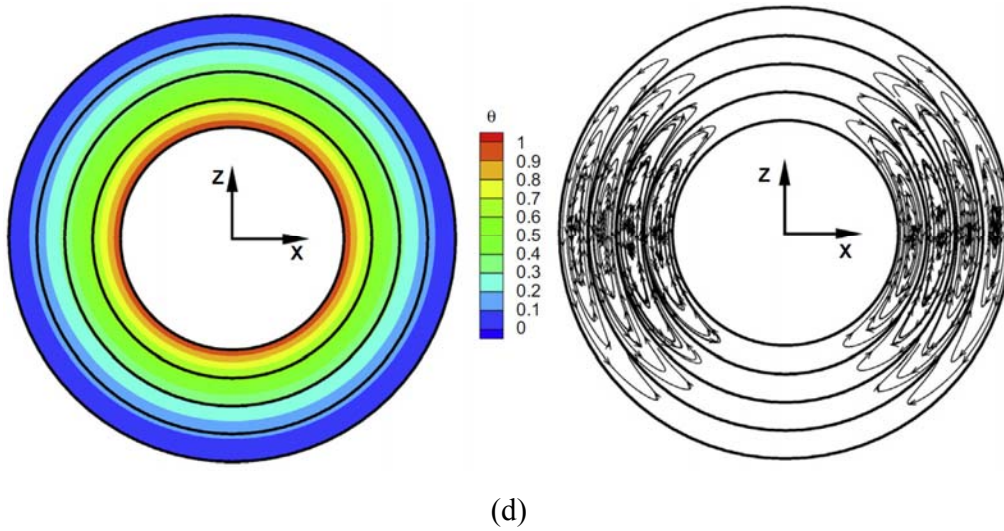
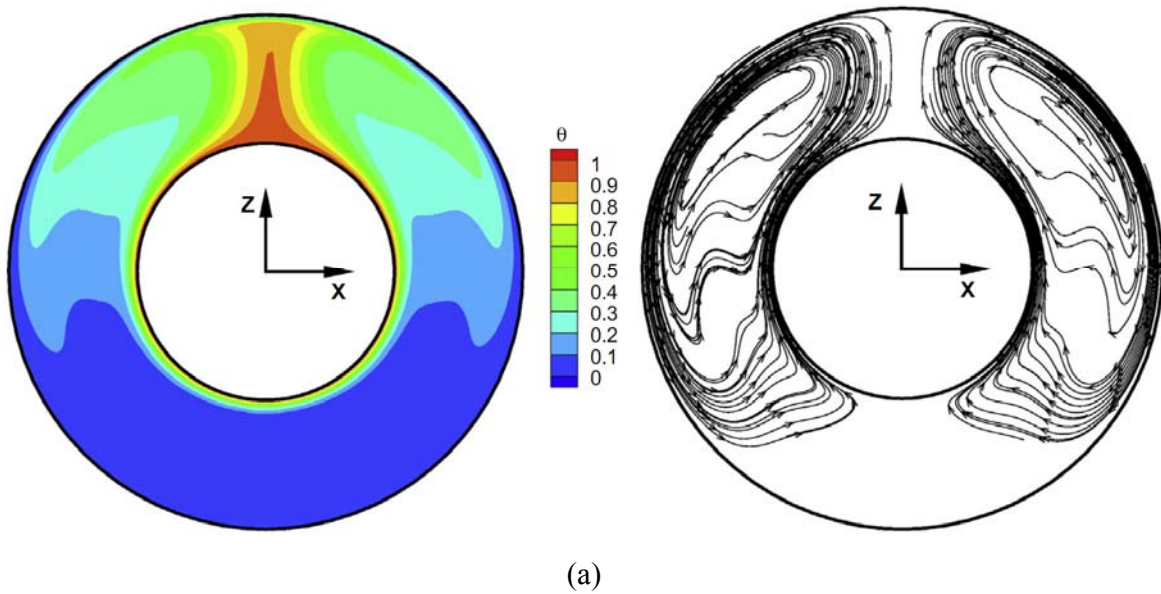
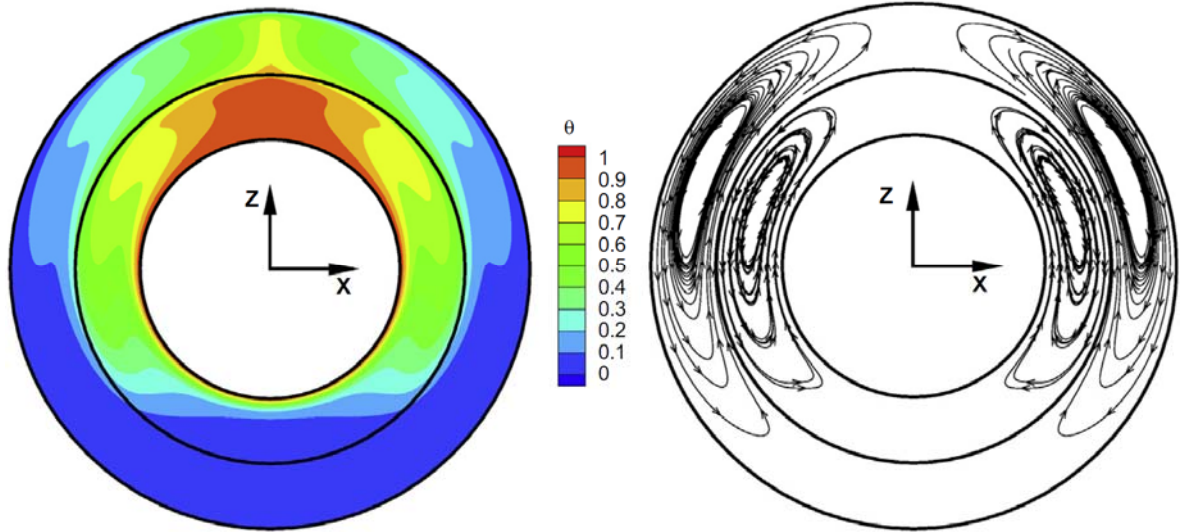
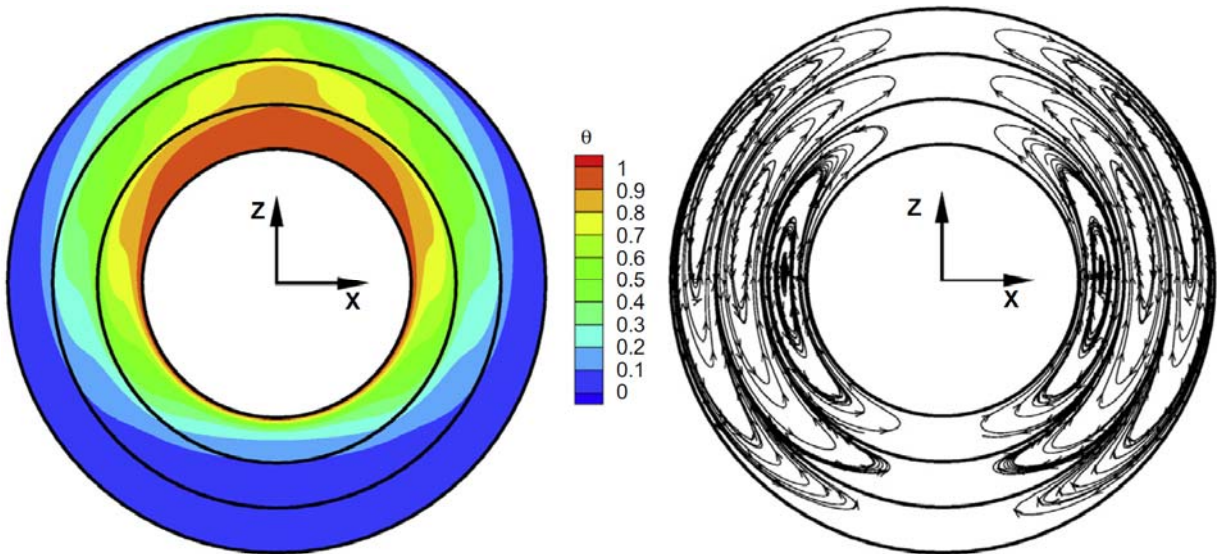


Figure 3.4. Steady-state temperature distribution θ , and projection of the flow path lines for $Ra = 10^4$ in the mid cross section of a spherical shell with: (a) one internal layer; (b) two equi-spaced internal layers; (c) three equi-spaced internal layers; (d) four equi-spaced internal layers.





(b)



(c)

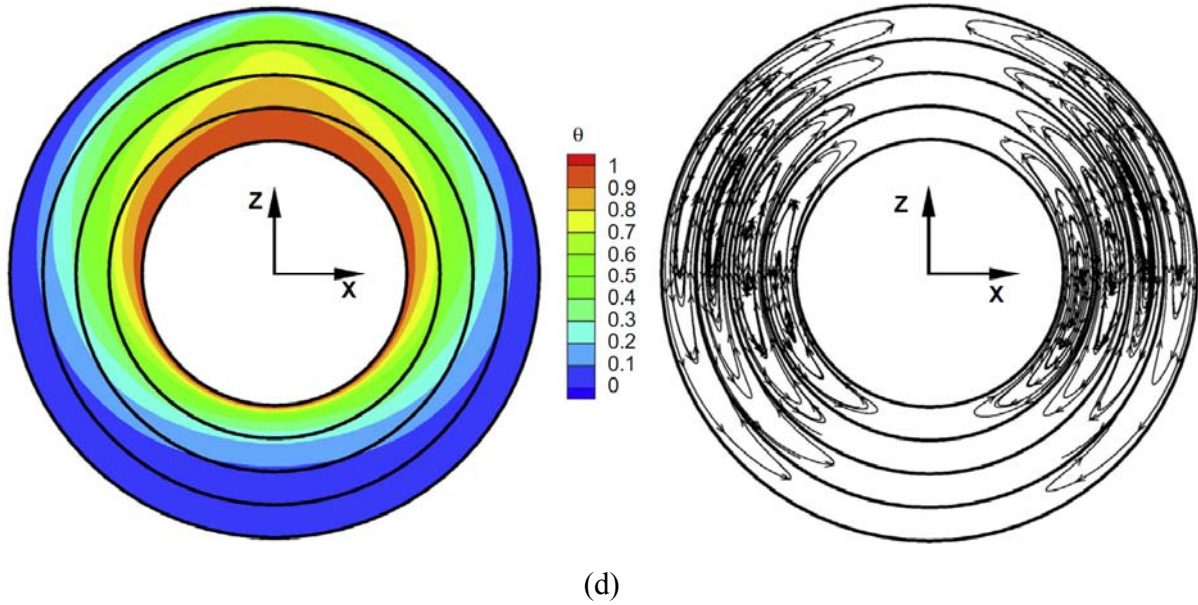
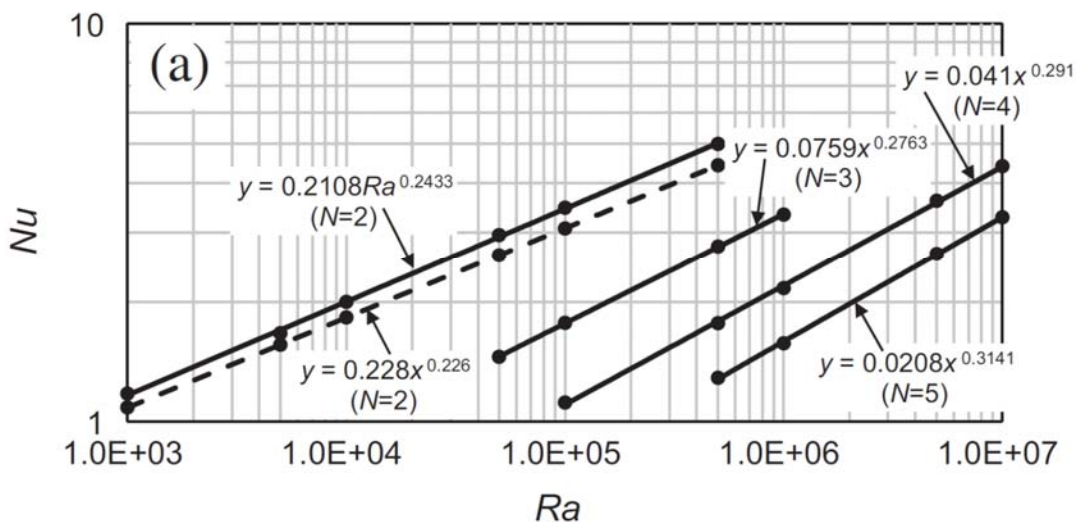


Figure 3.5. Steady-state temperature distribution θ , and projection of the flow path lines for $Ra = 5 \times 10^5$ in the mid cross section of a spherical shell with: (a) one internal layer; (b) two equi-spaced internal layers; (c) three equi-spaced internal layers; (d) four equi-spaced internal layers.

As expected, the steady flow obtained for all the configurations is axi-symmetric, as can be verified by a concentric shape of the flow path lines characterizing toroidal convection cells occupying each layer. It was also found that the internal baffles embedded in the spherical shell have a pronounced effect on the redistribution of convective flow inside the shell as follows. Firstly, the internal baffles stabilize the convective flow, thereby preserving steady-state regimes at much higher Ra values than those determining an instability onset in single-layered spherical shells. In fact, a modified kidney shaped eddy pattern, typical of high Ra values and wide shells and observed in Fig. 6a, transforms into a crescent eddy pattern for the configurations containing internal baffles (see Figs. 3.5 b–d). Secondly, the internal baffles suppress the convective component of the heat flux. As a result, a hot thermal plume rising up from the top of internal sphere either disappears at $Ra = 10^4$ or significantly weakens at $Ra = 5 \times 10^5$. The more internal baffles embedded, the weaker the convective heat transfer, and the closer the temperature distribution to that typical of a pure conduction regime. This observation is not surprising, since actual heat flux depends on the effective length scale which is a function of a number of internal baffles. We can then define an effective (modified) Ra^* number based on the distance between two adjacent baffles, which for the equi-spaced multi-layered spherical shell can be expressed as:

$$Ra^* = Ra/(N - 1)^3 \quad (3.1)$$

where N is the total number of the shell boundaries (internal and external). The quantitative differences in the observed flow regimes can be quantified by examining both the $Nu - Ra$ and the $Nu - Ra^*$ functionalities of each configuration. The same temperature difference between the hot and cold boundaries $\Delta\theta$, was chosen to provide a common basis for comparison. Fig. 3.6-a presents the $Nu - Ra$ functionality for spherical shells with two to five walls, when the Ra number is based on the total width L . In this case, the spherical shell is treated as a ‘black box’ whose insulation efficiency is only estimated as a function of the number of equi-spaced concentric internal baffles. Four separate curves were obtained for the $Nu - Ra$ power law functionality, each corresponding to a different number of walls. Note the good agreement between the current and the previously published results [7] obtained for a spherical shell without internal baffles for the entire range of Ra numbers. As expected, the insulation property of the spherical shell improves with the number of embedded baffles, leading to a considerable decrease in Nu for the same values of the Ra numbers. The maximal difference (up to four times) was observed at $Ra = 5 \times 10^5$ between the $N = 2$ and $N = 5$ configurations. To account for the effective length scale inherent to the multi-layered spherical shell problem, the modified Rayleigh number Ra^* is defined in Eq. (3.1), and the resulting $Nu - Ra^*$ functionality is shown in Fig.3.6-b. It can be seen that the curves corresponding to the different spherical shell configurations are now much closer, clearly indicating that the effective length scale plays an important role in determining the overall heat flux through the shell boundaries.



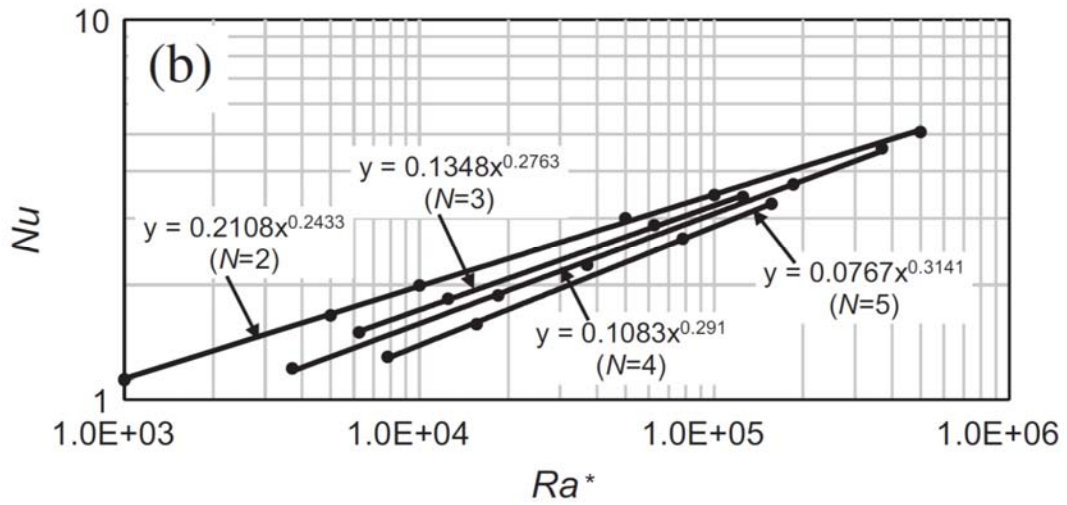


Figure 3.6. $Nu - Ra$ functionality obtained for spherical shells with different numbers of internal layers. The total number of walls for each spherical shell is given in parentheses. The dashed line corresponds to the universal correlation of Scanlan et al. [7] obtained for a single-layered spherical shell.

At the same time, introducing the modified Ra^* number is not enough to obtain the $Nu - Ra^*$ functionality in a form of the single curve universally fitting all the configurations discussed. This is apparently due to the fact that the actual temperature difference between the adjacent baffles is much smaller than it was assumed. Seeking ways to further generalize our analysis, we examined the $Nu - Ra^*$ functionality for all the configurations discussed and recognized both a monotonic increase of the power law exponent, and a monotonic decrease of the power law constant with an increasing number of layers. Formally denoting the power exponent by a and the power law constant by b , a functional relation of both quantities to the total number of shell boundaries N was approximated by the least squares method:

$$a = 0.443 \cdot N^{-1.064}, \quad 2 \leq N \leq 5 \quad (3.2)$$

$$b = 0.202 \cdot N^{0.27}, \quad 2 \leq N \leq 5 \quad (3.3)$$

Next it would be a matter of straight algebra to derive a unified correlation based on the power law for the $Nu^* - Ra^*$ functionality for up to five walls (see Fig. 3.7):

$$Nu^* = Ra^{*0.32} \quad (3.4)$$

where Nu^* is the modified Nu number defined as:

$$Nu^* = \left(\frac{Nu}{0.51 \cdot N^{1.21}} \right)^{1.65N^{-0.32}}, 2 \leq N \leq 5 \quad (3.5)$$

The equi-spaced concentric orientation of the internal layers is not the ultimate configuration to be considered for further improvement of the insulation efficiency of the spherical shell. In the following, three other configurations are discussed and their insulation properties are compared with the corresponding equi-spaced concentric.

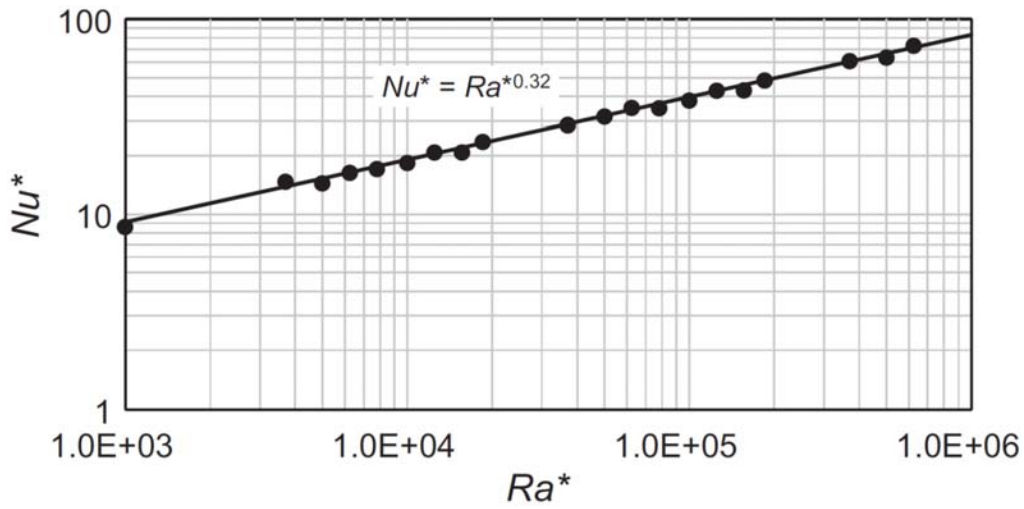


Figure 3.7. $Nu^* - Ra^*$ functionality. The correlation for modified Nu^* is valid for a multilayered spherical shell containing up to five equi-spaced concentric walls (four internal layers).

Horizontally/vertically eccentric layers

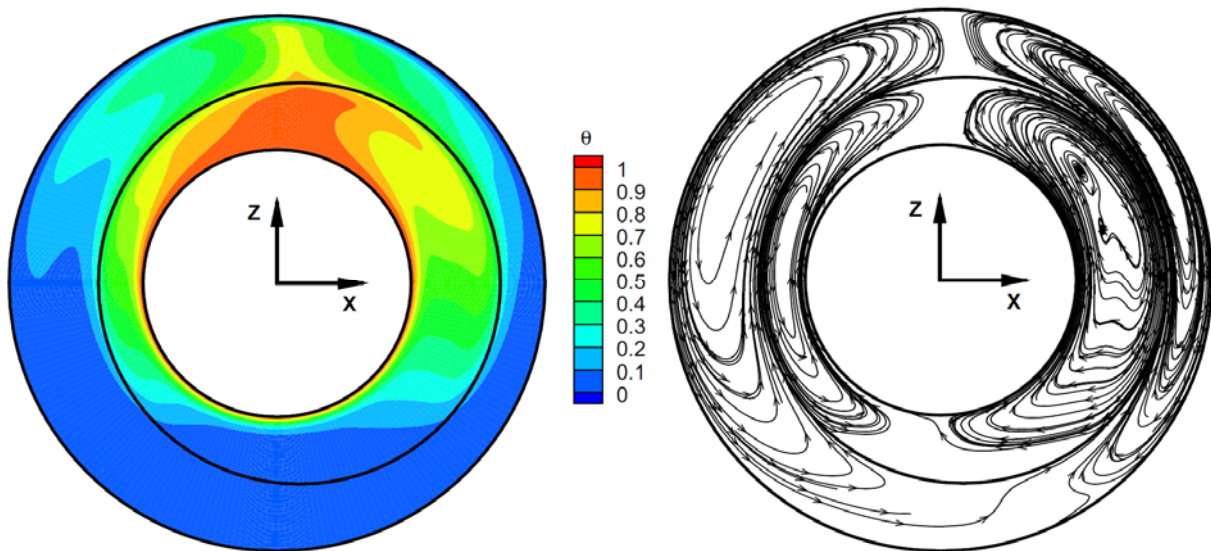
A number of double-layered spherical shells with varying vertical and horizontal eccentricity values were investigated. The eccentricity ϵ , is defined as:

$$\epsilon = \frac{|X_{eccentric} - X_{concentric}|}{L} \quad (3.6)$$

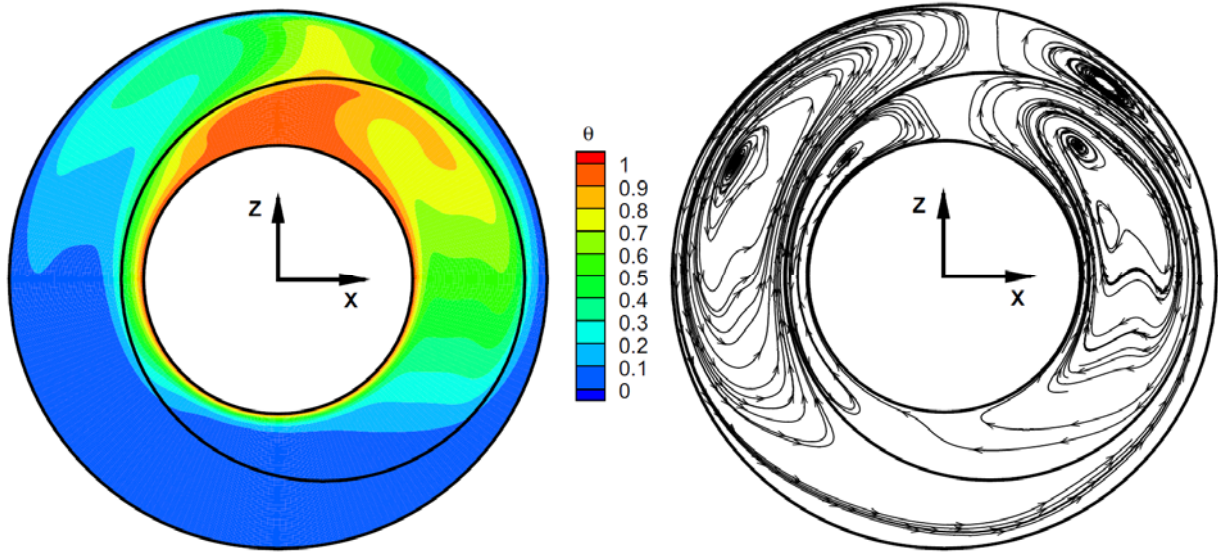
where $X_{eccentric}$ and $X_{concentric}$ are the center coordinates of the eccentric internal baffle and concentric internal and external boundaries of the spherical shell, respectively. Fig. 3.8 presents the steady-state distribution of the temperature field h , and the projection of the flow path lines on the mid-plane cross section of a double-layered spherical shell for two different eccentricity values $\epsilon = 0,167, 0,335$, and $Ra = 5 \times 10^5$. The impact of the horizontal offset of the internal baffle is clearly reflected in the character of the thermal plume, which is biased to the side in the direction of the offset. Note that the eccentricity has a pronounced effect on the distribution of both the θ

and the flow patterns in both layers. It is clear that the axial symmetry of the flow was broken and the flow is fully 3D. Non-negligible azimuthal velocities can be recognized by the presence of the flow path lines of a converging spiral shape in the center of some convection cells (see Fig. 3.8). Due to the lower temperature difference between the internal baffle and the external wall, the thermal redistribution inside the second layer is affected to a lesser extent by the eccentricity of the internal wall – a trend that is apparently preserved with a further increase in the number of internal layers.

The influence of the offset of the internal wall along the vertical axis on the steady flow fields is demonstrated in Fig. 3.9. The flow obtained was simulated for the same parameters ($Ra = 5 \times 10^5$ and $\phi = 0.5$) and eccentricity values as in the previous case. It is remarkable that the high temperature region inherent in the configuration with the downward biased internal sphere is much narrower than that observed for spherical shell with the upward biased internal sphere. Thus, the distance between the top of the hot boundary and the internal baffle has a critical effect on the development of the thermal plume inside the layer adjacent to the hot boundary. The closer the internal wall to the top of the hot boundary, the less is the local effective length scale of the flow, resulting in the lower velocity values of the thermal plume developed in that region. Similarly to the previously performed axi-symmetric simulations [50], a local increase of the distance between the internal baffle and the external boundary in the bottom region gives rise to the multi-cell convection flow (see Fig. 3.9), not observed in either concentric configurations.

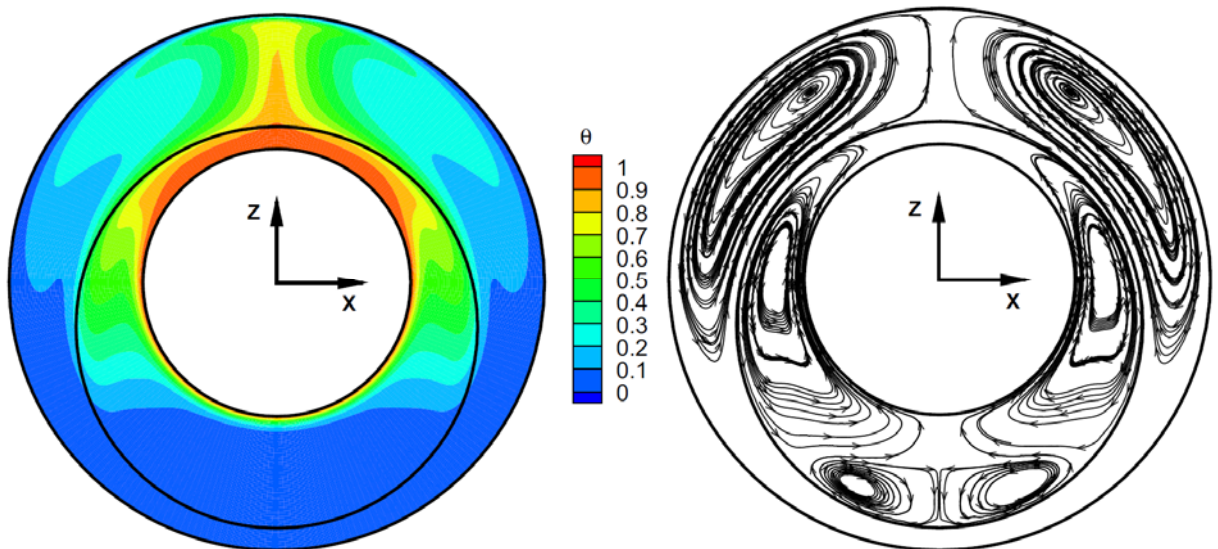


(a)



(b)

Figure 3.8. Steady-state flow fields, obtained at the mid-plane cross section of a three-wall spherical shell for $Ra = 5 \times 10^5$. Contours of the temperature θ and projection of the flow path lines for: (a) $\epsilon = 0,167$; (b) $\epsilon = 0.335$.



(a)

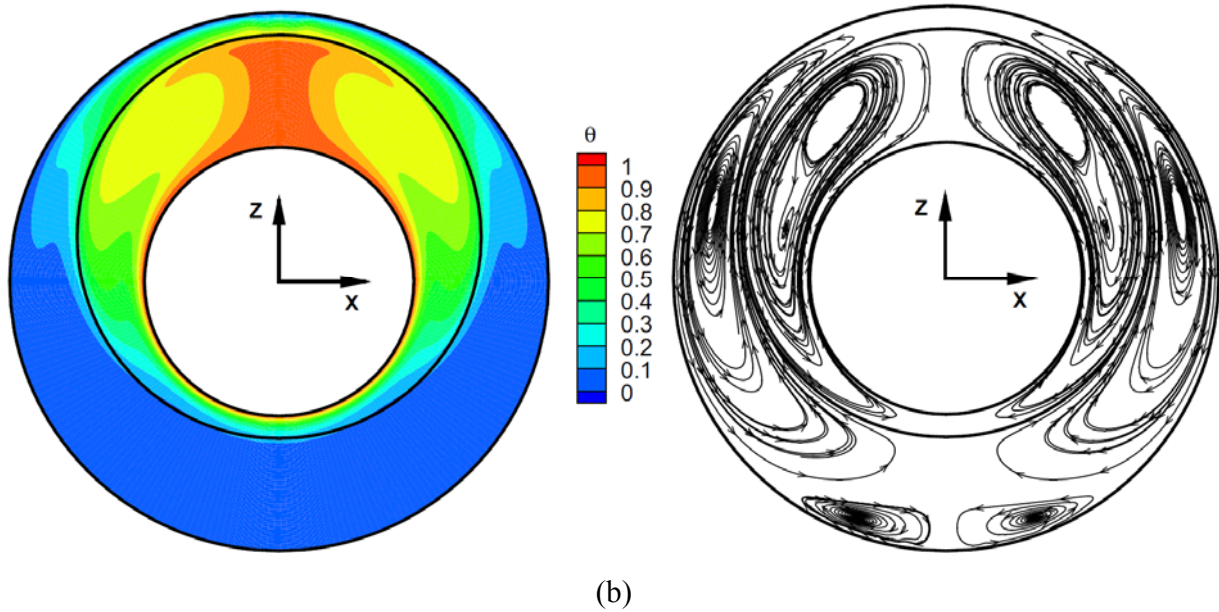


Figure 3.9. Steady-state flow fields obtained at the mid-plane cross section of a three-wall spherical shell for $Ra = 5 \times 10^5$. Contours of the temperature θ and projection of the flow path lines for: (a) $\epsilon = 0,167$; (b) $\epsilon = 0,167$.

Non-equi-spaced concentric layers

We next focused on the investigation of the effect of a non-uniform width of the internal layers on the characteristics of the steady state flow developing inside the double-layered spherical shell. The non-uniform, non-dimensional distance was defined in terms of the diameter ratio $1 \leq D_b/D_i \leq 2$, where D_b corresponds to the diameter of internal baffle and D_i is the diameter of the hot boundary sphere. Note that the value $D_b/D_i = 1.5$ corresponds to the double-layered equi-spaced configuration. The numerical simulations were performed for two configurations corresponding to $D_b/D_i = 1.17, 1.83$ and $Ra = 5 \times 10^5$. The steady state distribution of the temperature field θ , and the azimuthal velocity field ϕ in the mid cross section of the spherical shell obtained for both cases, are shown in Fig. 3.10.

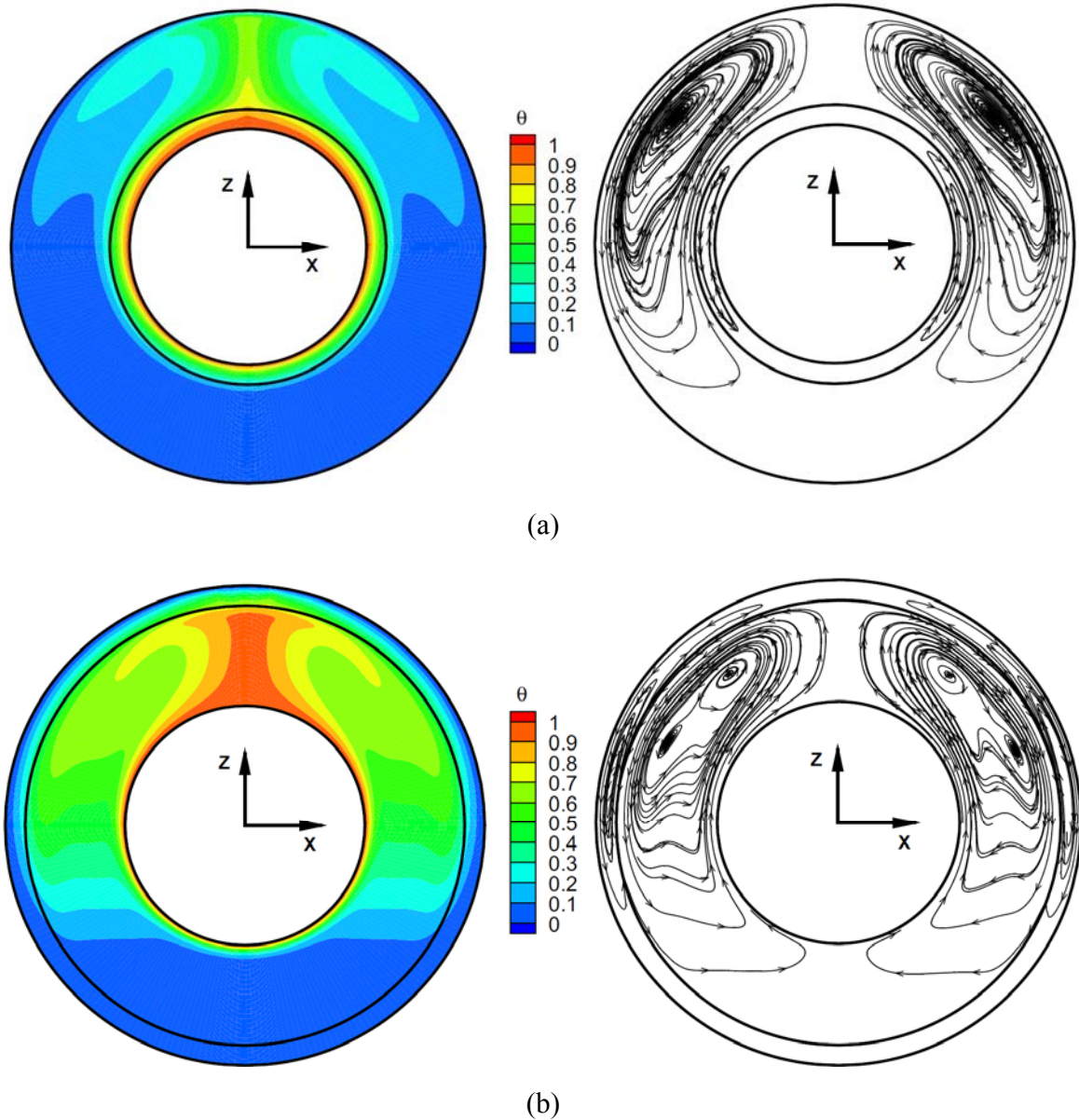


Figure 3.10. Steady-state flow fields obtained at the mid cross section of a three-wall spherical shell for $Ra = 5 \times 10^5$. Contours of the temperature θ and projection of the flow path lines for: (a) $D_b/D_i = 1.17$; (b) $D_b/D_i = 1.83$.

Clearly, the proximity of the internal baffle to any of the spherical shell boundaries suppresses the convective flow motion in the corresponding internal layer. In contrast, convective heat transfer with a fully developed thermal plume dominates in both cases in the wide internal layer. Also remarkable is an existence of the different shape patterns in the sub-layers of different widths for both cases: a crescent eddy in the narrow sub-layer and a modified kidney shape eddy in the wide

sub-layer. The differences between all the configurations discussed were quantified in terms of Nu numbers, as summarized in Table 3.5. It is noteworthy that the most significant variation (-15% to +16%) of the Nu value was observed inside the non-equi-spaced spherical shell configuration. In this case, the minimal Nu value was provided by the smallest distance between the hot wall and the internal baffle, clearly indicating a route for further improvement of the spherical shell insulation efficiency. In contrast, the eccentricity of the internal baffle (both horizontal and vertical) has a much less pronounced effect on the heat flux rate through the boundaries of the spherical shell.

Table 3.5

Nu number values for a double-layered horizontally eccentric internal sphere.

Horizontal eccentricity ϵ	Nu number	Comparison with equi-spaced 3w configuration $Nu = 2.87$
0.167	2.92	+2%
0.335	2.89	+1%

Vertical eccentricity ϵ	Nu number	Comparison with equi-spaced 3w configuration $Nu = 2.87$
-0.335	3.16	+9%
0.335	3.15	+9%

D_b/D_i	Nu number	Comparison with equi-spaced 3w configuration $Nu = 2.87$
1.17	2.43	-15%
1.83	2.45	+16%

3.3. Smart thermo-insulation

3.3.1. Verification of the linear stability analysis

The verification study focuses on analysis of the natural convection flow around two cylinders confined by a square cavity (see Fig. 3.11). The ratio between the cylinder diameter d , and the cavity side length L , is equal to $d/L = 0.2$. The cylinders are aligned along the cavity's vertical centerline and are symmetrically distanced from the cavity's horizontal centerline. The distance δ between the cylinder centers, normalized by the cavity side length L , is equal to $\delta = 0.5$. Both cylinders are held at a constant hot temperature $\theta_H = 1$, whereas all the cavity boundaries are held at a constant cold temperature, $\theta_C = 0$. The force of gravity acts in the negative y direction. The above configuration was chosen for the two main reasons.

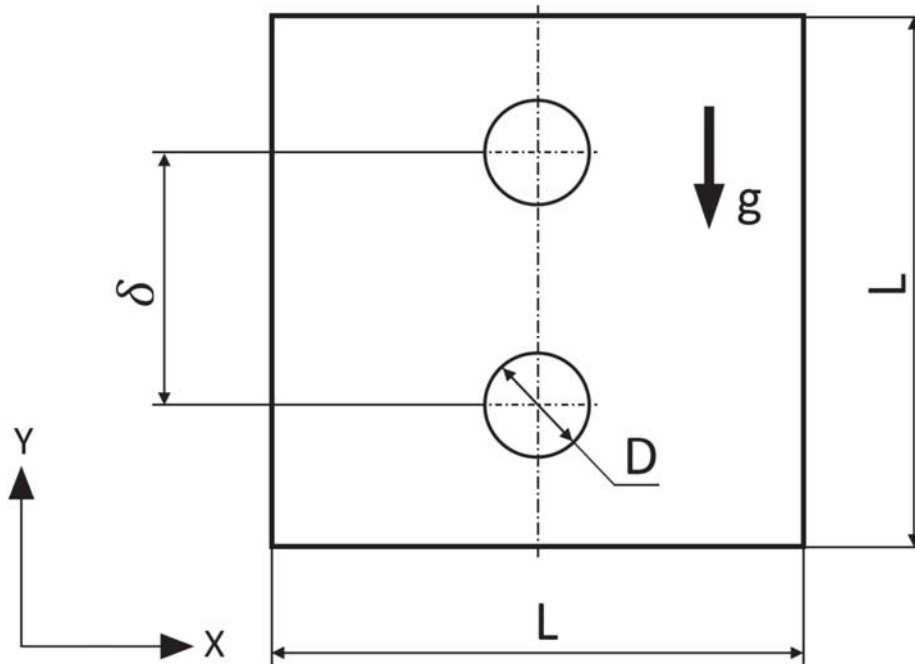


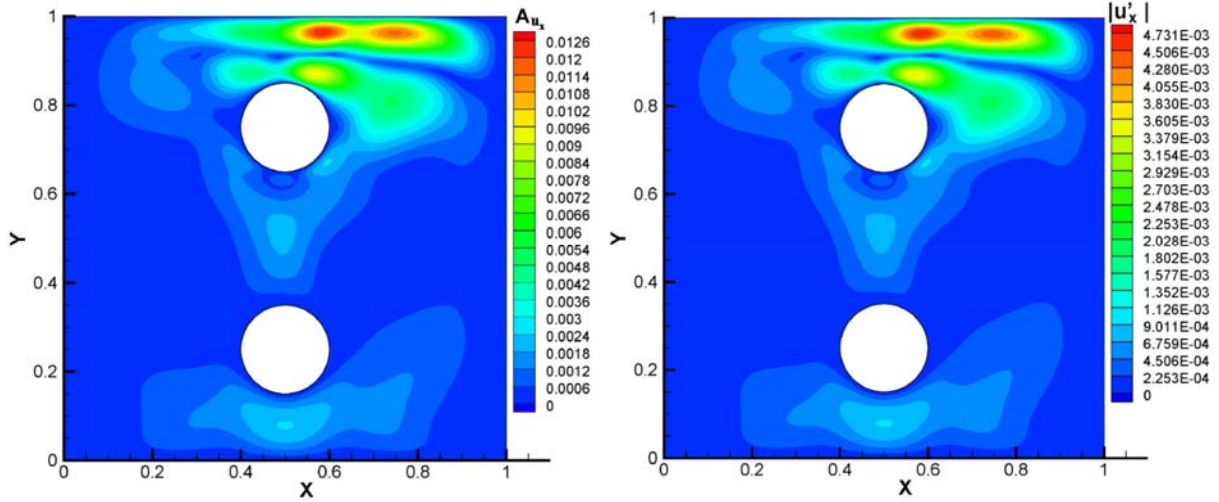
Figure 3.11. Vertically aligned cylinders confined by a square cavity: schematic representation of a geometrical model of the computational domain. The arrow indicates the direction in which the force of gravity acts.

First, it is relevant to the configurations under consideration in the present study, the only exceptions being that the porous media is modelled by thermally passive unconnected cylinders. Second, the considered flow undergoes transition to unsteadiness through the first Hopf bifurcation [54], which allows to compare the patterns of absolute values of the leading eigenvectors of temperature and velocity fields obtained by linear stability analysis with those obtained by calculation of the time averaged oscillation amplitudes³.

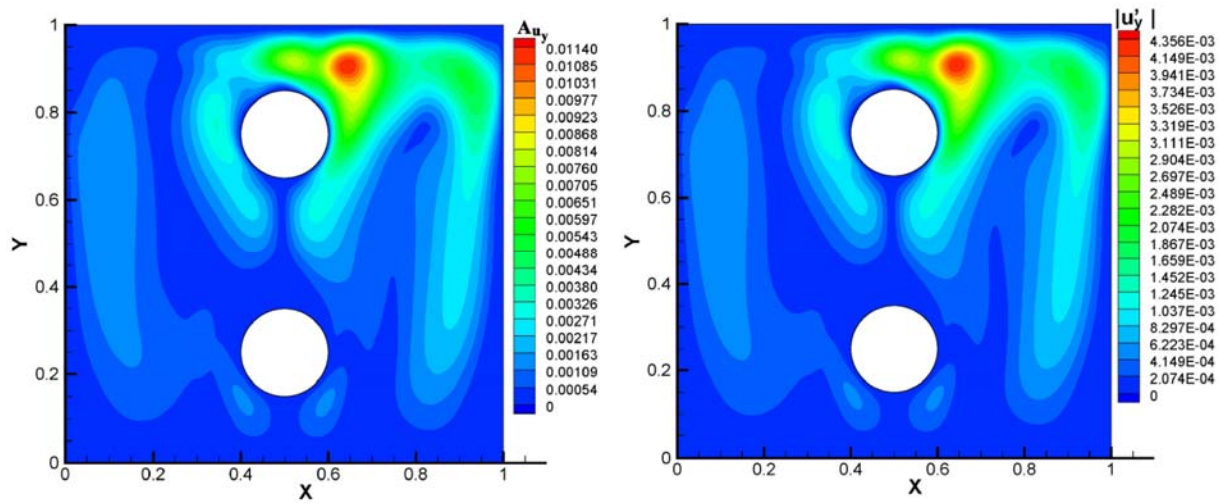
Figure. 3.12 presents comparison between the contours of the leading eigenvectors obtained for u_x , u_y and θ fields, and the corresponding contours of oscillating amplitudes averaged over 20 time periods. An excellent agreement between the corresponding spatial distributions verifies the correctness of the performed linear stability analysis. Note the significant quantitative discrepancy observed between the values of oscillation amplitudes and the absolute values of the corresponding eigenvectors. This fact is not surprising since the magnitude of the leading

³ Contours of maximal time averaged amplitudes of bifurcated flow conveniently approximate contours of absolute values of the corresponding leading eigenvectors [55-57].

eigenvector obtained by the linear stability analysis indicates the spatial distribution of intensity of oscillations exhibited in bifurcated flow, and is determined up to multiplication by a constant.



(a)



(b)

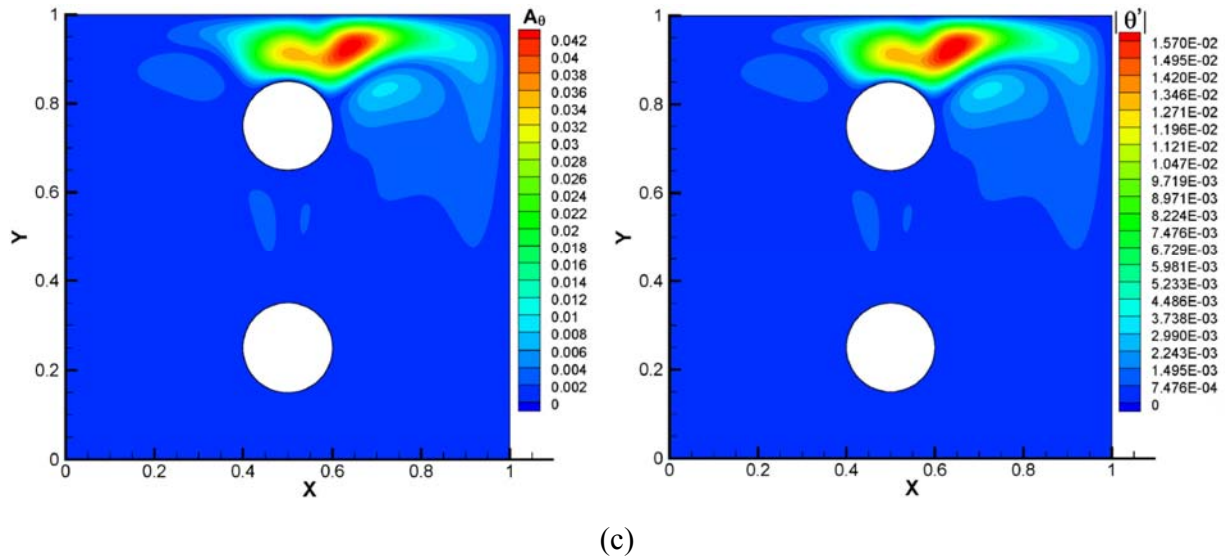


Figure 3.12. Contours of the averaged oscillating amplitudes and the corresponding absolute values of leading eigenvectors obtained for: (a) velocity component u_x ; (b) velocity component u_y ; (c) temperature, θ .

3.3.2. Results and discussion

In this section the concept of "smart" thermally-insulating materials is presented, first, for 2D conduced natural convection flow. The square differentially heated cavity with perfectly thermally conducting horizontal boundaries is used as a test bed. The proposed concept is further validated for the realistic 3D flow in deferentially heated cubic cavity with thermally perfectly conducting lateral walls and all no-slip boundaries.

*"Smart" thermo-insulating materials for 2D flows*⁴

Heat flux rate through the differentially heated cavity can be estimated by the calculation of the average Nusselt number Nu at the cavity boundaries, which for the no-slip boundary conditions only depends on the temperature gradient normal to the wall direction. Note that for the steady state flow, the temperature distribution is skew-symmetric relative to the cavity center (i.e. F), and therefore the net heat flux rate is only determined by the average Nu values calculated at the vertical boundaries. At steady state, both Nu values should be equal to provide conservation of the total heat flux. It is commonly known (see e.g. [58, 59]) that for this type of steady natural

⁴ This section is based on Y. Gulberg, Y. Feldman [61]

convection flow, $Nu \sim Ra^{0.25}$. As the Rayleigh number increases, the flow undergoes steady-unsteady transition through the first Hopf bifurcation. Further increase of the Ra number eventually leads to the turbulent flow regime, characterized by an increased heat flux rate through the cavity boundaries governed by the $Nu \sim Ra^{0.33}$ relation [58, 59]. It is clear that the most intuitive way to considerably decrease heat flux rate through the cavity boundaries would be to completely fill up the cavity interior by any kind of homogeneous thermal insulator. However, this naive approach will significantly increase costs and the overall weight of such thermal insulation. A typical flow pattern inside the differentially heated cavity filled with thermal insulating materials of different porosity is presented in Figure 3.13. As can be seen from $Nu - Ra$ functionality (see Fig. 3.14), there is no significant difference between $\phi = 0.8$ and $\phi = 0.7$ for high Ra values, which can result in an idea that similar thermal insulation efficiency can be achieved by introducing a small amount of bodies into a flow.

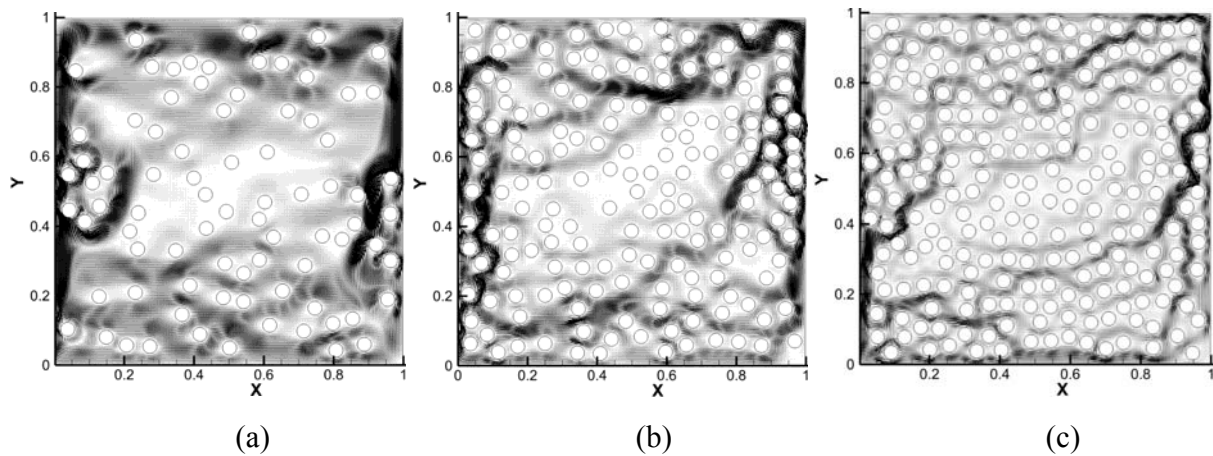


Figure 3.13. A typical flow field inside a differentially heated cavity filled with thermal insulating material. $Ra = 10^7$, Porosity = V_V/V_T , V_V -void, V_T -total. (a) $\phi = 0.9$ (b) $\phi = 0.8$ (c) $\phi = 0.7$.

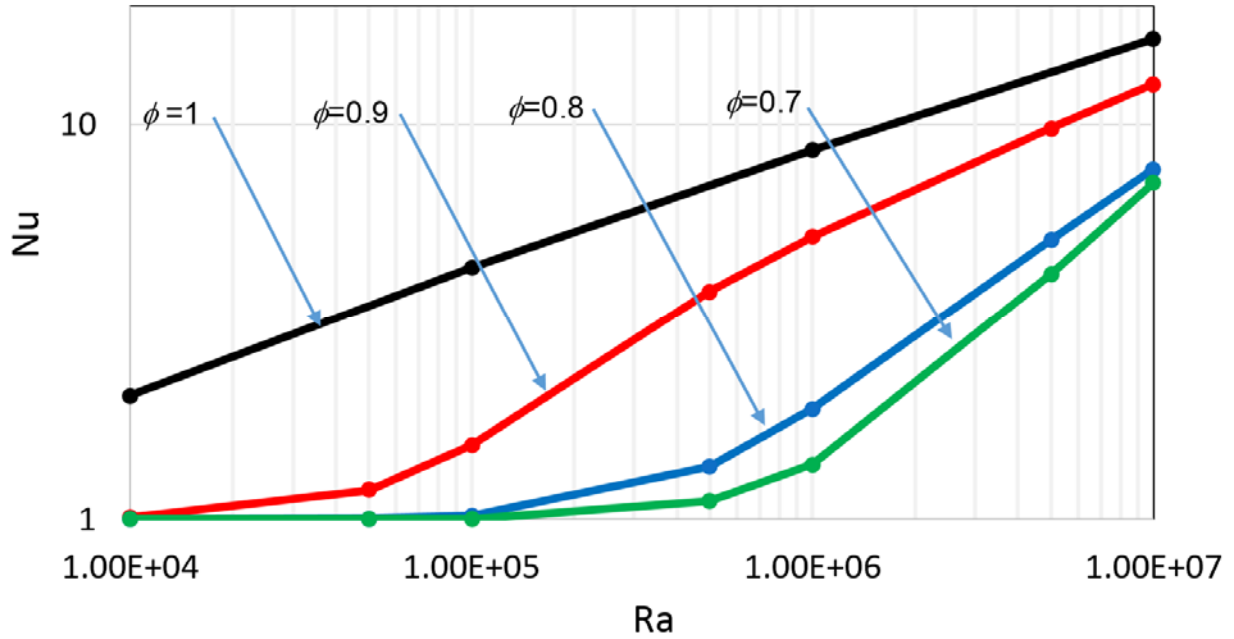
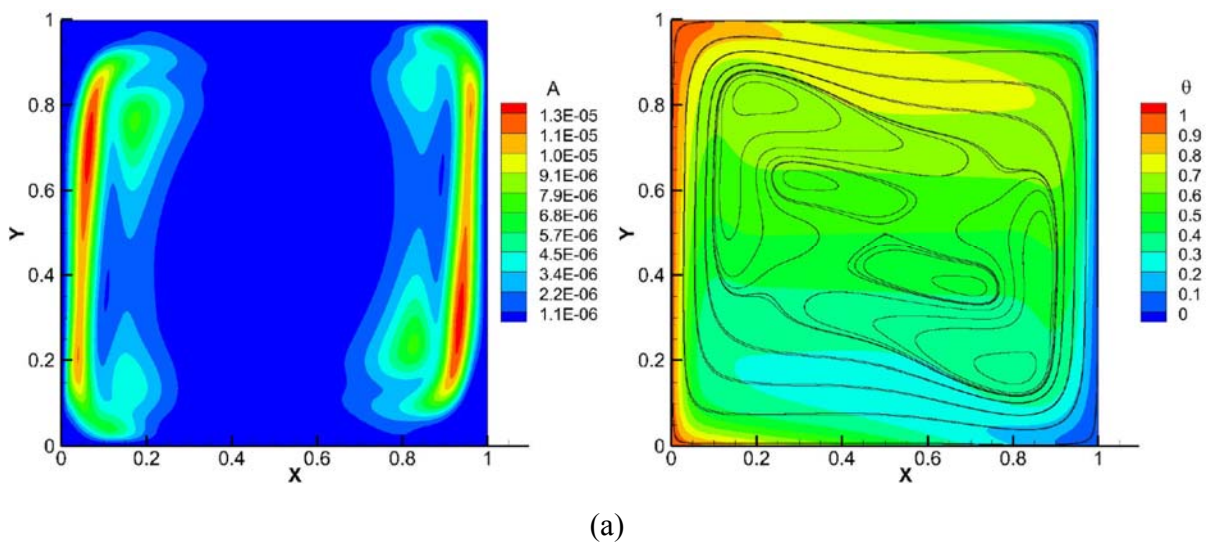


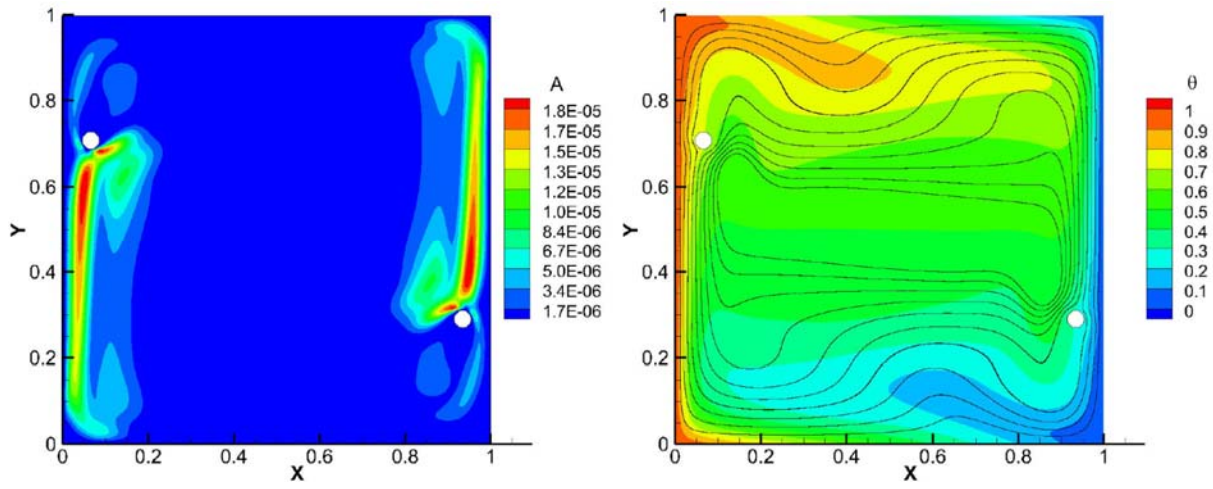
Figure 3.14. $Nu - Ra$ functionality for a differentially heated cavity filled with thermal insulating material.

Another alternative comprising the key idea of the present study is to considerably decrease heat flux rate through the cavity boundaries by intelligently suppressing the momentum of the flow in accordance with a priori defined criteria. The first criterion **A** is defined as $\mathbf{A} = |u'_x|^2 + |u'_y|^2$, where $|u'_x|$ and $|u'_y|$ are the absolute values of perturbations of the corresponding velocity components. The idea originates from the definition of the turbulent kinetic energy e'_k , equal to the sum of squares of fluctuations of the velocity components, although the proposed criterion **A** can not be formally related to e'_k due to the phase differences between $|u'_x|$ and $|u'_y|$. The second criterion **B** is directly related to the absolute value of perturbation of the temperature $\mathbf{B} = |\theta'|$. In the present study, we demonstrate the impact of local suppressing the momentum of the flow by locating cylindrical thermally passive obstacles of uniform diameter $d = 0.04$ in the regions with maximal absolute values of the criteria **A** and **B**, as defined previously. Figure 3.15 demonstrates the procedure used for the design of a "smart" thermal insulator aimed at decreasing the heat flux rate for the natural convection flow inside a differentially heated cavity with thermally, perfectly conducting lateral walls. The procedure is iterative and utilizes the **A** criterion. At the first iteration, the linear stability analysis is performed for the flow within the cavity without obstacles, yielding the value of critical Rayleigh number Ra_{cr} for the first Hopf bifurcation. The corresponding fields

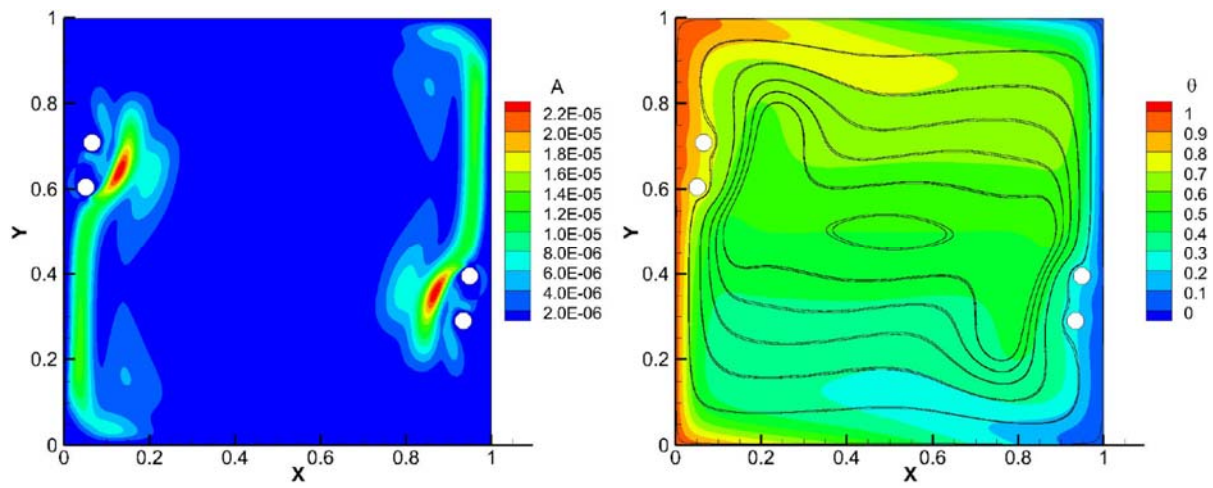
of values of \mathbf{A} and the temperature distribution at steady state with the superimposed streamlines are shown in Fig.3.15-a. Then a pair of cylindrical obstacles are located at places where \mathbf{A} reaches its absolute maximum⁵. At the next step, the linear stability analysis is performed for the modified flow inside the cavity containing two embedded obstacles (see Fig. 3.15-b). As a result, we obtain a new value of Ra_{cr} , at which the modified flow characterized by a new distribution \mathbf{A} undergoes transition to unsteadiness. The next pair of obstacles can be located again at places where the new values of \mathbf{A} reach their absolute maximum. The above procedure is repeated until a priori chosen stop condition is achieved (a twofold decrease in the average Nu number). Figs. (3.15 c-h) demonstrate evolutionary stages of the modelled implant of porous media, which can be seen as a prototype for a "smart" thermally insulating material based on the criterion \mathbf{A} .



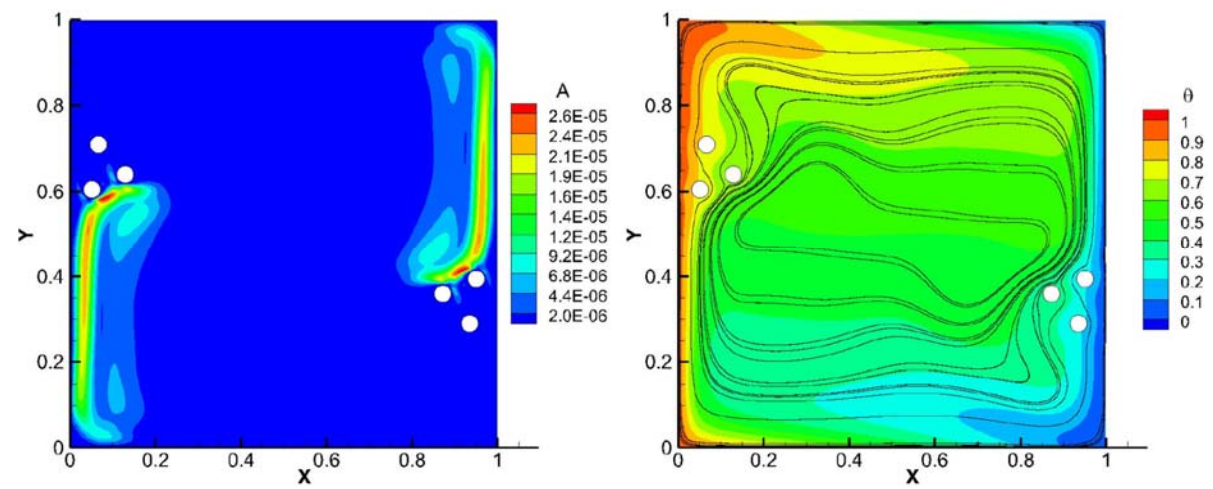
⁵ Note that for the configuration discussed the distribution of \mathbf{A} is skew-symmetric relative to the cavity center, i.e. $\mathbf{A}(x, y) = -\mathbf{A}(L - x, L - y)$ and therefore the obstacles always come in pairs.



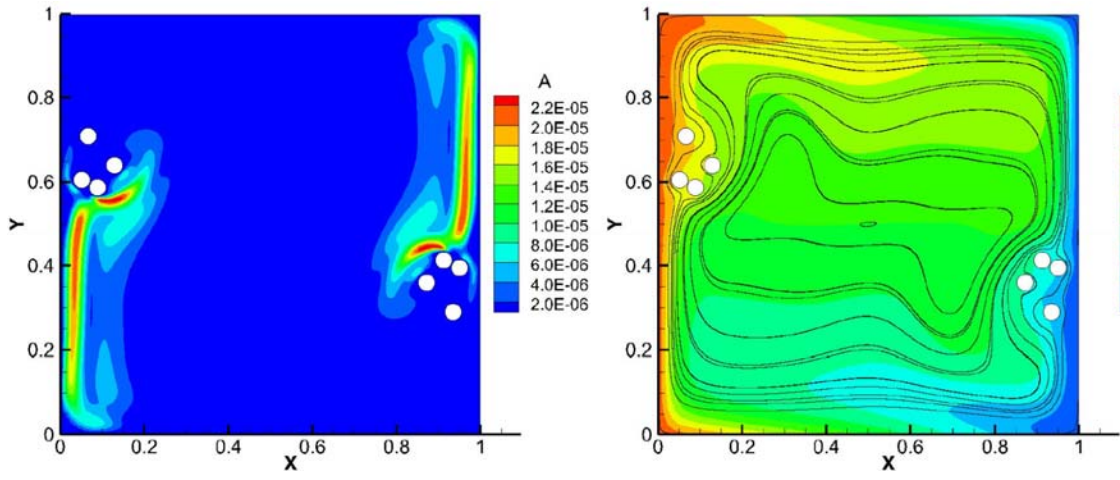
(b)



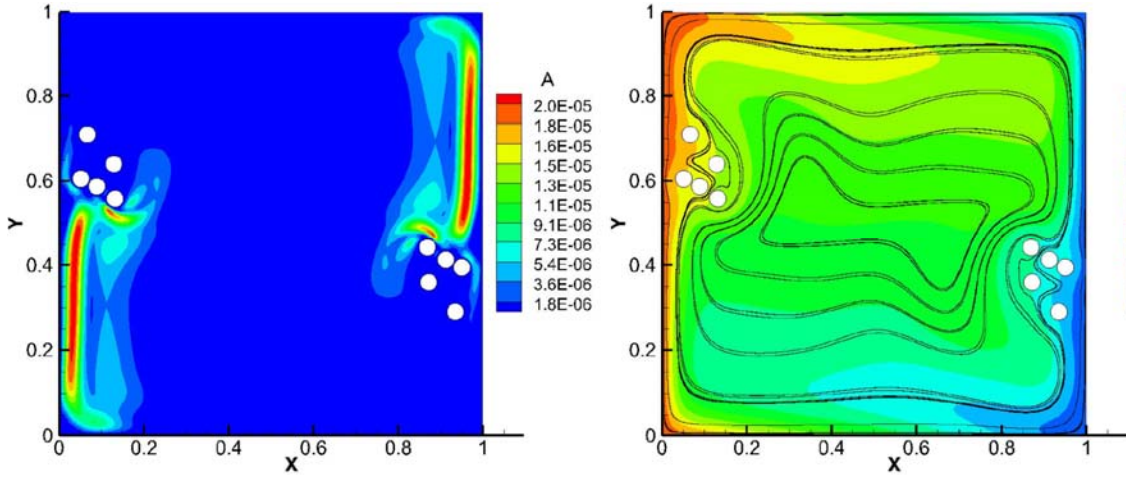
(c)



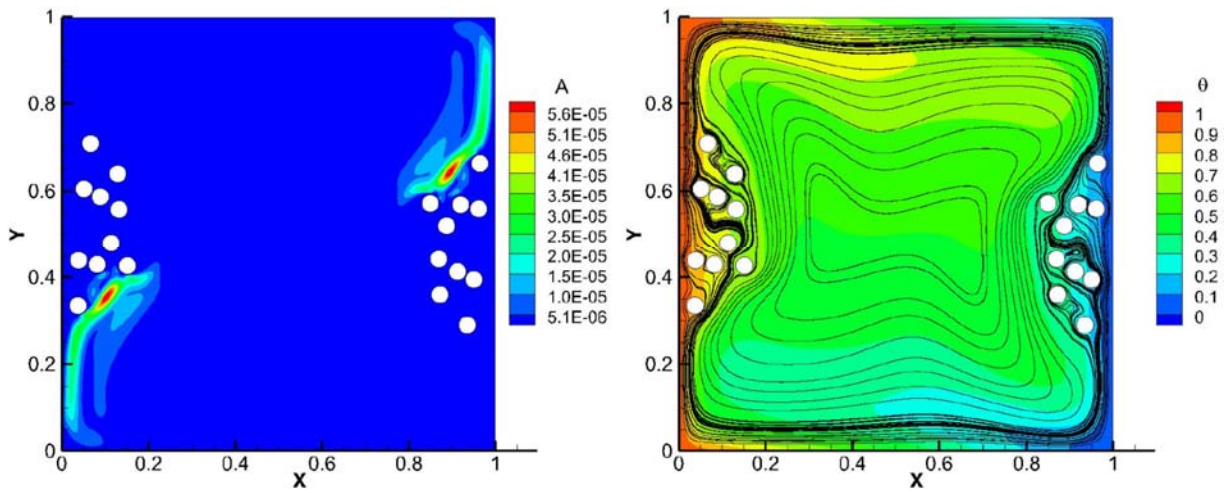
(d)



(e)



(f)



(g)

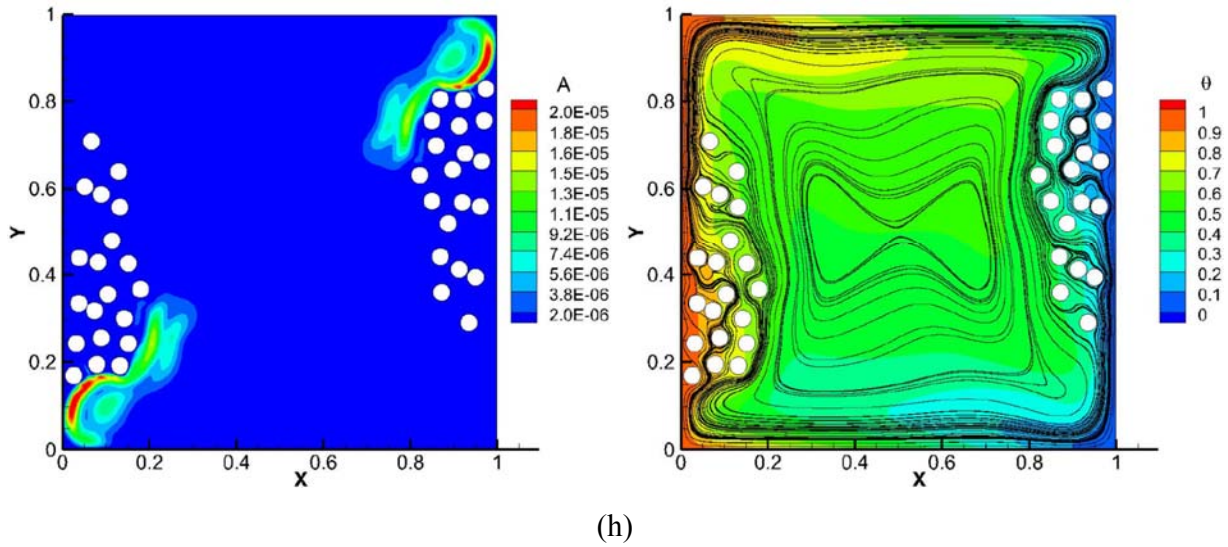
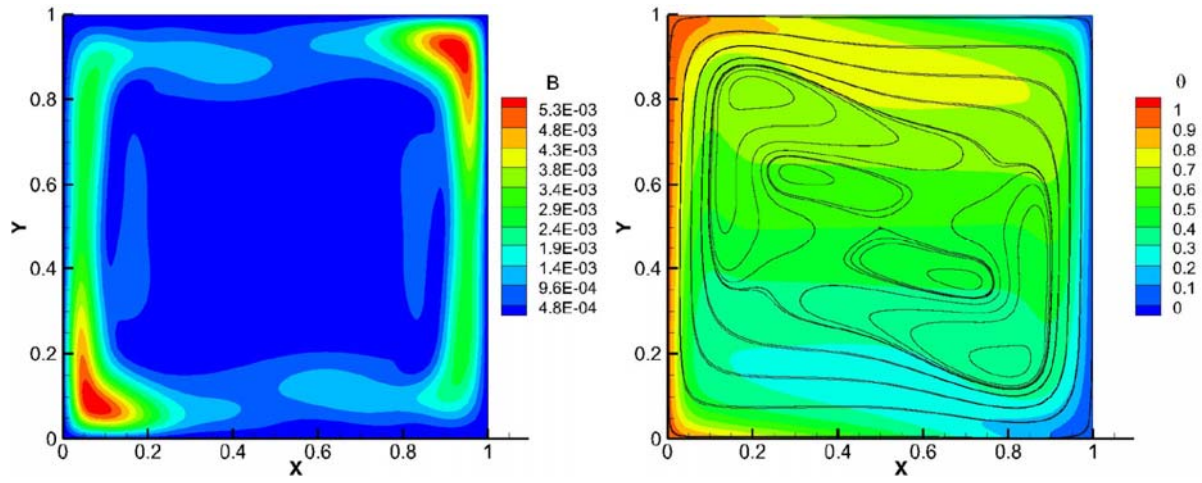


Figure 3.15. Contours of the criterion \mathbf{A} and the corresponding steady state distribution of temperature θ , with superimposed streamlines obtained at $Ra = 2.11 \times 10^6$ for: (a) no obstacles; (b) 2 obstacles; (c) 4 obstacles; (d) 6 obstacles; (e) 8 obstacles; (f) 10 obstacles; (g) 20 obstacles; (h) 40 obstacles. Diameter of all the obstacles is equal to $d = 0.04$.

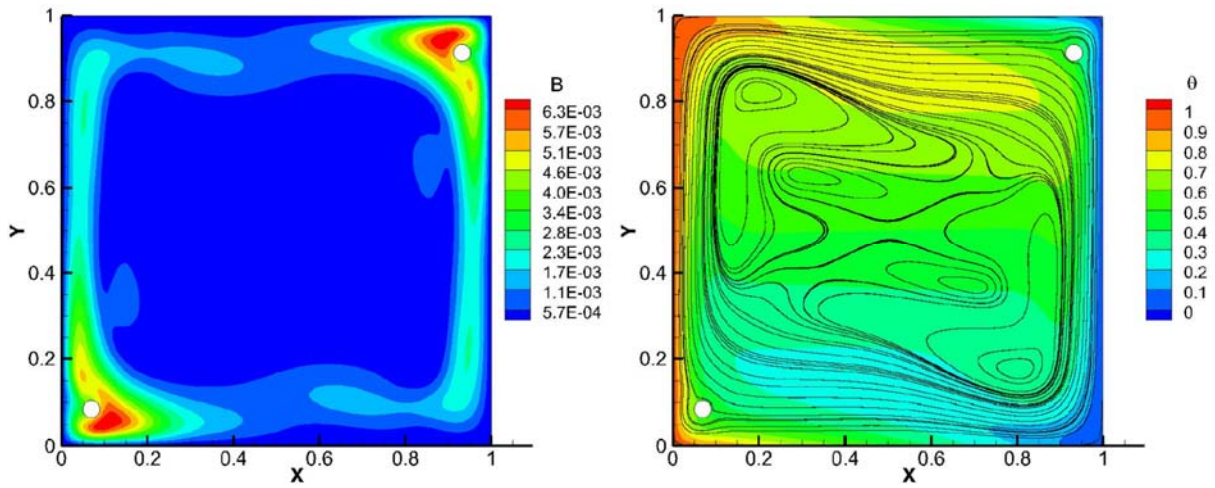
At the next stage, an alternative design of implant of the porous media was obtained by applying an iterative procedure based on the value of the second optimization parameter \mathbf{B} . Evolution stages of the design corresponding to a different number of embedded cylindrical obstacles are shown in Fig. 3.16⁶. It should be stressed that in the present study the morphological structure of the modelled implants of porous media is restricted to unconnected packed beds (due to the limitations of the IB method). The above limitation, however, can be violated if the distance between any global maxima of \mathbf{A} or \mathbf{B} is equal or less than the diameter of the cylindrical obstacle. In addition, none of the obstacles should touch or intersect any of the cavity boundaries. In both cases, the location of the next largest value of \mathbf{A} or \mathbf{B} is sought and the morphological structure of the current "candidate" of the porous media implant is tested for meeting all the restrictions. The procedure of seeking a new location for the next pair of cylindrical obstacles should be repeated until all the above restrictions are satisfied⁷.

⁶ Note that for the configuration discussed, the distribution of \mathbf{B} is skew-symmetric relative to the cavity center and therefore the obstacles always come in pairs.

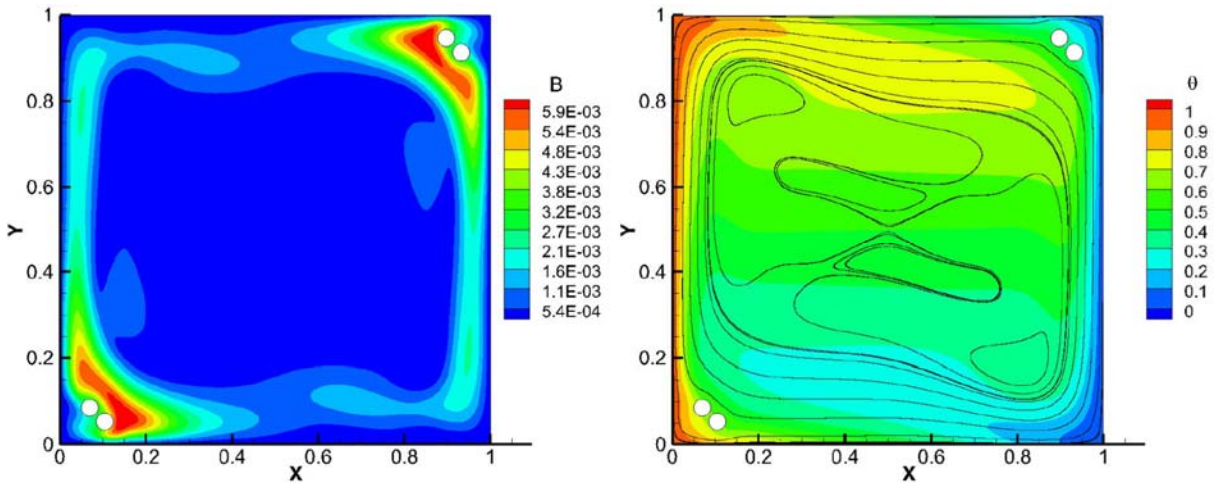
⁷ Typically, only one iteration was required for the configurations considered in the present study.



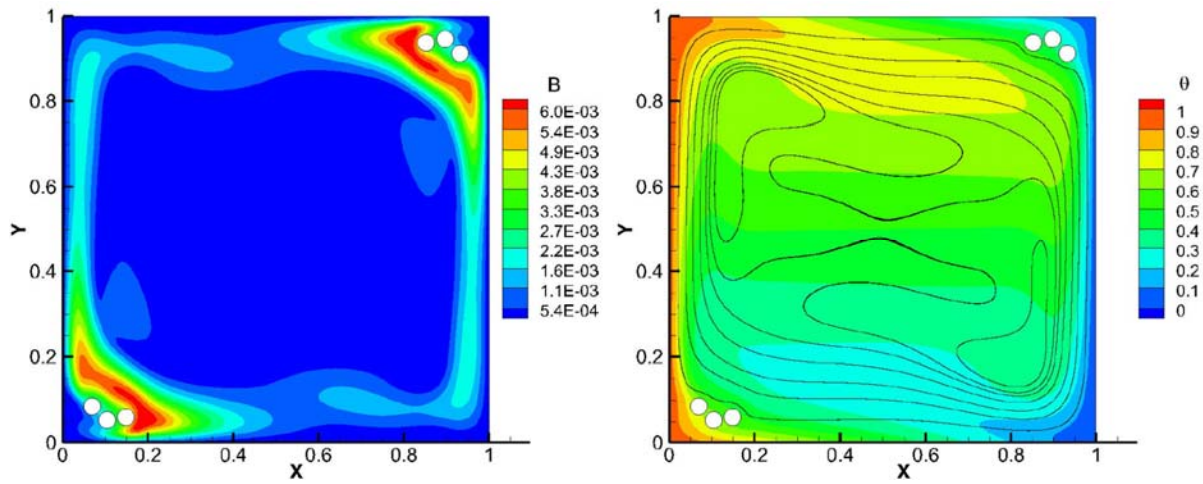
(a)



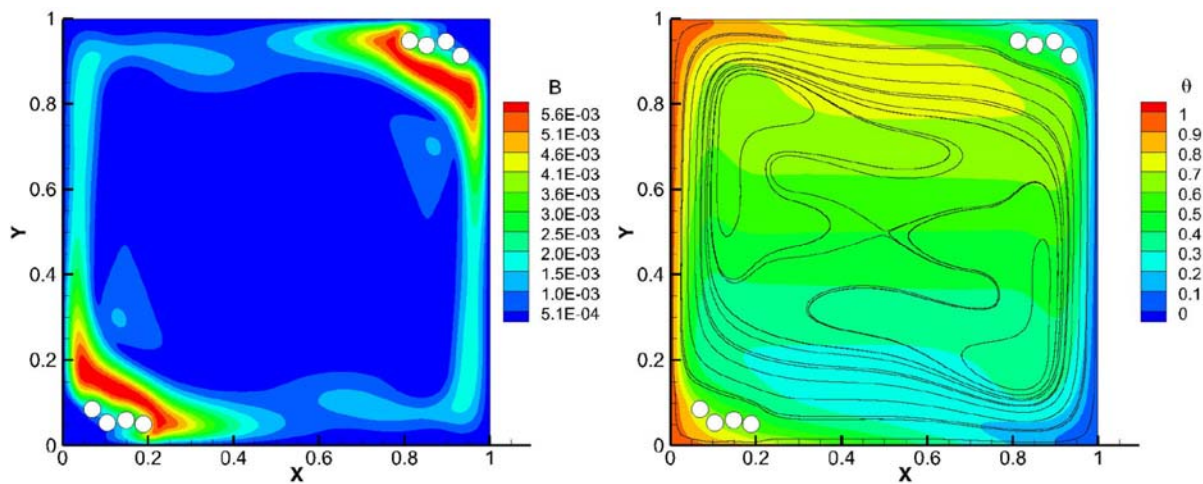
(b)



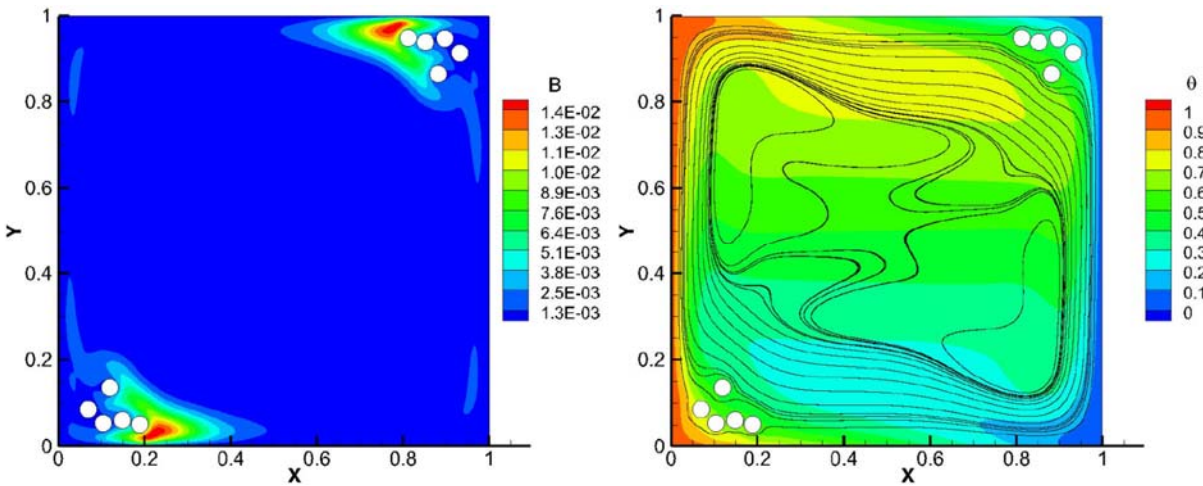
(c)



(d)



(e)



(f)

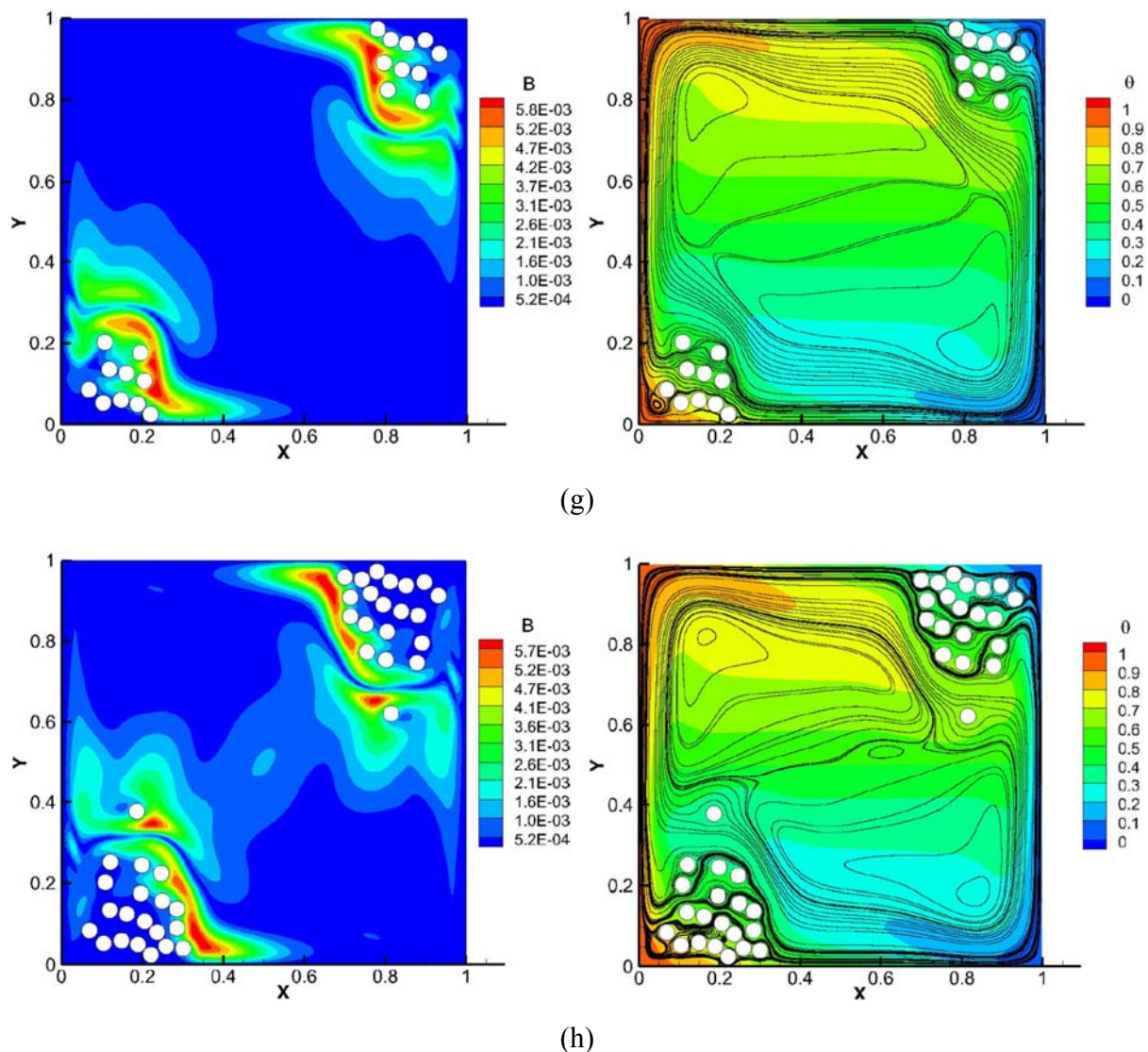
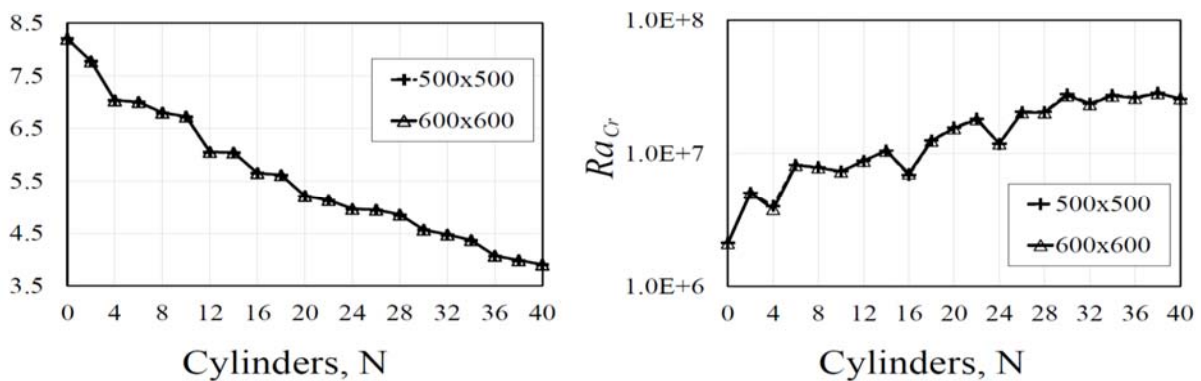


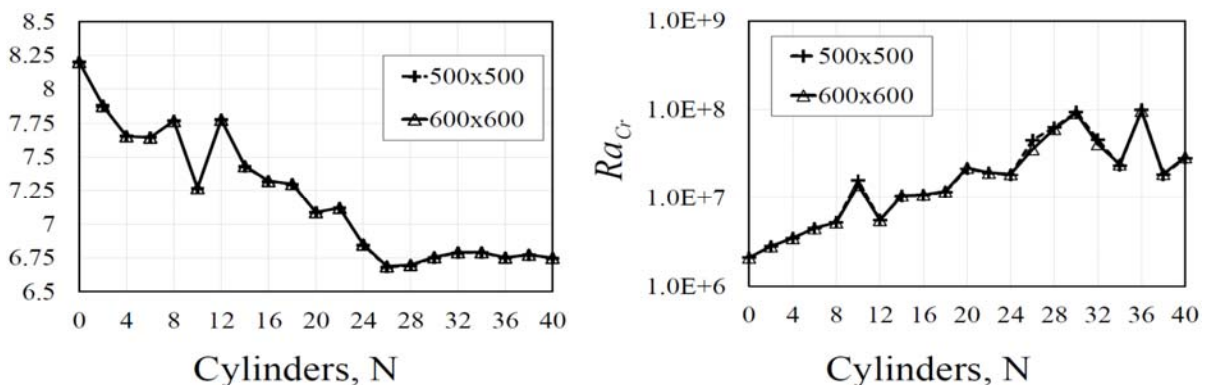
Figure 3.16. Contours of the criterion B and the corresponding steady state distribution of temperature θ , with superimposed streamlines obtained at $Ra = 2.11 \times 10^6$ for: (a) no obstacles; (b) 2 obstacles; (c) 4 obstacles; (d) 6 obstacles; (e) 8 obstacles; (f) 10 obstacles; (g) 20 obstacles; (h) 40 obstacles. Diameter of all the obstacles is equal to $d = 0.04$.

Embedding cylindrical obstacles is characterised by a twofold mechanism which can increase an insulating efficiency of the cavity. First, for the given value of the Ra number, it suppresses the overall momentum of the convective flow, which in turn leads to increasing thickness of the thermal boundary layer, and results in lower temperature gradients in normal to the vertical walls direction. Second, it delays the onset of unsteadiness, which means that the natural convection flow in the cavity with embedded obstacles remains laminar and steady, even at rapidly increasing Ra numbers. The effect of both mechanisms was quantified, as shown in Fig.

3.17. Indistinguishable differences are observed for both average Nu and critical Ra_{cr} values obtained on 500×500 and 600×600 , which successfully verifies grid independence of the results. It can be also seen that utilizing the implants of porous media designed in accordance with the first criterion A, (see Fig. 3.17-a) allows for a rapid decrease of the average Nu number values, attaining half its original value for 40 embedded cylinders⁸. Note also that 40 cylinders only occupy 5% of the total volume of the cavity. The dependency of Ra_{cr} values on the number of obstacles is not as monotonic, although the critical Ra_{cr} number of the final configuration consisting of 40 cylinders is by an order of magnitude higher compared to its original value.



(a) Optimization criterion A



(b) Optimization criterion B

Figure 3.17. Variation of the values of the averaged Nu number obtained for the vertical hot wall of the cavity at $Ra_{cr} = 2.11 \times 10^6$ and the critical Rayleigh Ra_{cr} number for the steady-unsteady transition obtained by the linear stability analysis as a function of a number of cylindrical obstacles for: (a) **A** optimization criterion; (b) **B** optimization criterion.

⁸ All the simulations were performed at $Ra_{cr} = 2.11 \times 10^6$, at which the flow without obstacles undergoes steady-unsteady transition.

The implants of porous media designed by utilizing the second criterion **B**, (see Fig. 3.17-b) exhibit much lower efficiency in terms of thermal insulation. In fact, embedding the implants consisting of 40 cylinders (the same amount as for criterion **A**) leads to only about 30% decrease in the average Nu value. Moreover, after embedding 24 cylinders, the average Nu number reaches its asymptotic value, which does not deviate significantly with the number of embedded cylinders. Similarly to the previous configuration, the dependency of the Ra_{cr} value on the number of obstacles is not monotonic. It is remarkable that again, one order of magnitude difference is observed between the initial and the final values of the critical Ra_{cr} number. It is worth noting that the similar 30% decrease in average Nu value was also reported by Costa et al. [60] when investigating the influence of solid inserts of thermal conductivity equal or less than the fluids placed at the inner corners of differentially heated square enclosures. According to the authors, the rationale for these inserts choice can be explained by the stagnation regions, which develop in the vicinity of the corners. In the present study we revisit and explain formally the observed decrease of heat flux rate by means of linear stability analysis of the natural convection flow.

"Smart" thermo-insulating materials for 3D flows

In the present section, the concept of "smart" thermally insulating materials is validated for the realistic 3D flows. The 2D configurations containing implants of porous media embedded into the square differentially heated cavity are extruded in the direction, normal to the plane of 2D cavity. As a result, the original 2D configurations are transformed into their 3D analogs, comprising a cubic differentially cavity with thermally, perfectly conducting, lateral walls, and all no-slip boundaries. The 2D circular obstacles are in turn transformed into 3D circular cylinders, extending over the whole cavity width. Example of four of such 3D configurations corresponding to the optimization criteria **A** and **B**, with patterns containing 20 and 40 cylinders, are shown in Fig. 3.18.

All the simulations were performed for $Ra = 2.11 \times 10^6$ corresponding to the value of the critical Rayleigh number Ra_{cr} , characterizing the transition to unsteadiness of the 2D flow inside a differentially heated cavity with thermally, perfectly conducting horizontal walls. We note in passing, that for a differentially heated cavity $Ra_{cr_{2D}} < Ra_{cr_{3D}}$, due to the damping affect of lateral walls, which determines a steady state regime of all the 3D flows considered in the present study.

Convergence to steadiness is assumed to be reached when the maximal point-wise relative difference for a field at two consecutive time steps is less than 10^{-5} . Note also a striking resemblance between the 3D and the corresponding 2D temperature distributions (see Figs. 3.15-g, h, Figs. 3.16-g,h) are typical of this kind of convective flow. Table 1 presents the grid independence study in terms of the Nu values averaged over the hot wall of the cavity as a function of the amount of embedded obstacles. The results were obtained on 200^3 , 300^3 and 400^3 grids.

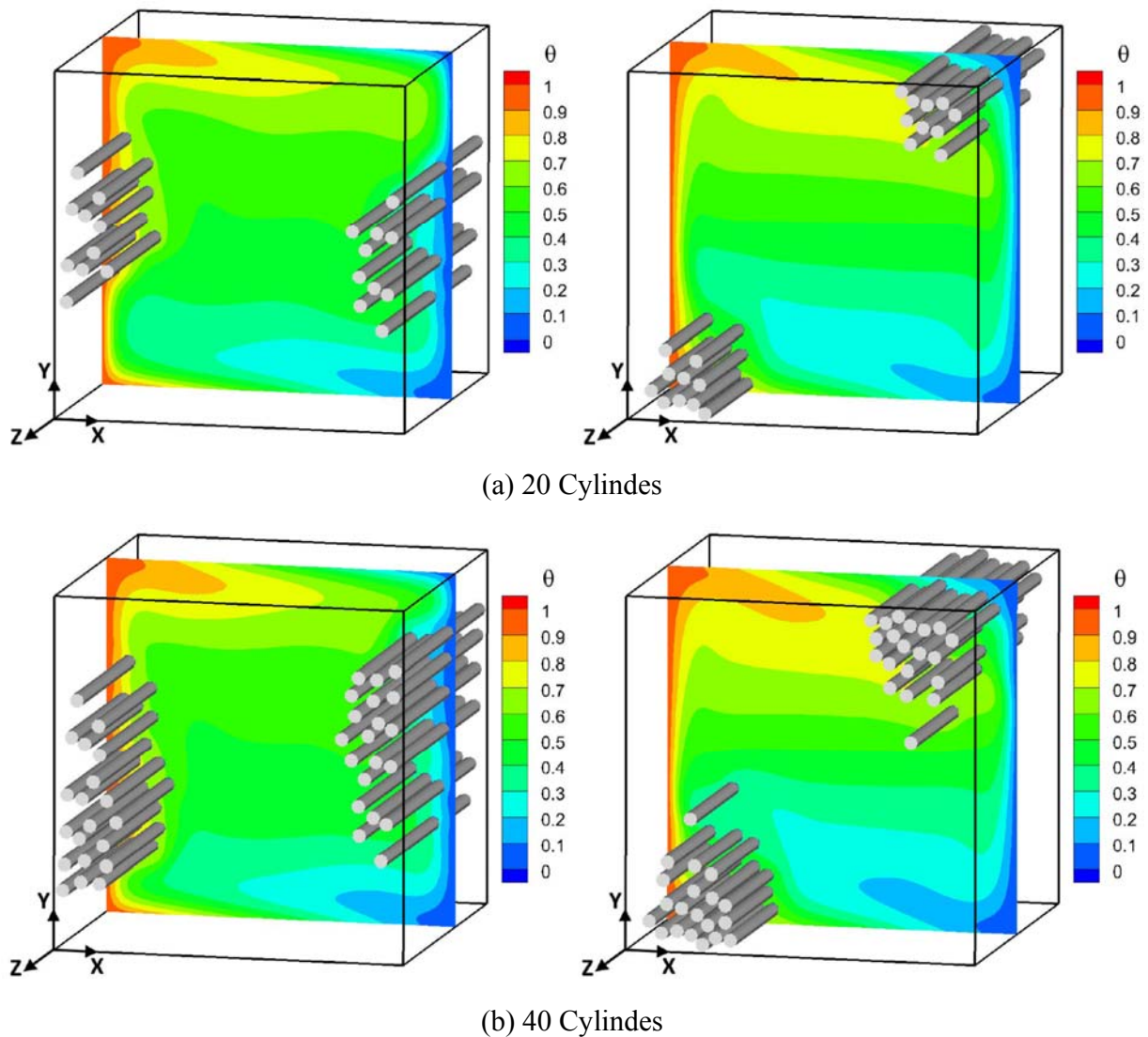


Figure 3.18. 3D setup obtained by extrusion of the corresponding 2D configurations in the z direction with superimposed temperature distribution at mid cross-section of the cavity obtained at $Ra = 2.11 \times 10^6$ by : (a) 20 cylinders location of which was obtained by utilizing optimization criteria **A** and **B**; (b) 40 cylinders location of which was obtained by utilizing optimization criteria **A** and **B**.

Table 3.6: Verification of grid independence of the averaged Nu values calculated at the hot wall of the cubic cavity for $Ra = 2.11 \times 10^6$

Number of cylinders	Criterion A			Criterion B		
	200 ³	300 ³	400 ³	200 ³	300 ³	400 ³
0	8.353	8.353	8.353	8.353	8.353	8.353
10	6.449	6.506	6.552	7.043	6.985	6.992
20	4.943	5.087	5.126	6.588	6.755	6.724
30	4.281	4.327	4.356	6.333	6.426	6.328
40	3.535	3.569	3.589	6.214	6.34	6.328

It can be seen that the maximum deviation in the averaged Nu values for 300³ and 400³ grids does not exceed 1%, successfully verifying a grid independence of the results. All the calculations of 3D flow further presented in this section were obtained on a 400³ computational grid. It was also verified (not shown here) that the values of Nu numbers averaged over the hot and the cold walls are equal up to the fourth decimal digit, which proves a conservation of the overall heat flux through the cavity boundaries.

The final validation of concept of "smart" thermally insulating materials designed by utilizing both **A** and **B** optimization criteria for 2D and 3D flows is summarized in Table 3.7. It is remarkable that in a 3D differentially heated cavity, the ultimate morphology of the implant of porous media designed by utilizing criterion **A**, and consisting of 40 cylinders, yield slightly higher than two fold decrease in average Nu value than the two fold decrease observed for the corresponding 2D configuration. In contrast, when the second optimization criterion **B** is used, both 2D and 3D implants of porous media yield to only a 30% decrease in the average Nu number.

Table 3.7: Validation of the concept of "smart" thermally insulating materials for 2D and 3D flows. The Nu values were averaged over a hot wall of a differentially heated cavity with all thermally perfectly conducting horizontal (2D) and lateral (3D) walls.

Number of cylinders, N		0	10	20	30	40
Criterion A	2D	8.2	6.728	5.215	4.568	3.906
		8.2	7.270	7.089	6.756	6.750
Criterion A	3D	8.353	6.552	5.126	4.356	3.589
		8.353	6.992	6.724	6.328	6.328

Chapter 4

Conclusions

The present study was aimed at investigating passive control of natural convection flow in confined enclosures, and to develop a novel methodology to further enhance passive control of confined natural convection flows. At the first stage, a heuristic approach applied to the control of laminar, natural convection flow inside spherical shells with concentric, eccentric, equi-spaced and non-equi-spaced, zero thickness internal baffles was investigated by the IBM. Numerical simulations were performed by extending the general pressure–velocity segregated solver [38], (based on the tensor product factorization (TPF) method combined with the Thomas solver (TPT)) with the immersed boundary functionality. The results obtained were extensively verified by performing a detailed grid independence study and comparison with previously published data.

The insulation efficiency of the spherical shell was studied for up to five walls, corresponding to four equi-spaced, concentric internal layers. It was found that the number of internal baffles had a considerable effect on the average Nu number, whose value was computed for a shell with four equi-spaced, concentric internal layers decreased by up to fourfold, compared to that obtained for a single-layer spherical shell. It was shown that the length scale of the flow is determined by the difference between two adjacent walls. This observation allowed derivation of a unified functional dependency, correlating the modified Nu^* and Ra^* numbers for a spherical shell with up to four equi-spaced, concentric, internal layers. The effect of the eccentricity of the internal baffle (both horizontal and vertical) on the developing various flow patterns and on the insulating efficiency of a spherical shell was also investigated. The results – both qualitative and quantitative – showed that for a particular Ra , both vertical and horizontal eccentricities have a quite limited impact on the total heat flux rate through the shell boundaries. In addition, the effect of the width of the internal layer and its proximity to the hot and cold boundaries on the total heat flux rate was studied. It was found that the configuration with the narrowest concentric layer close to the hot boundary provided the best insulating efficiency, characterized by a Nu value that was about 15% lower than that obtained for the same operating conditions for the equi-spaced spherical

shell. In contrast, the Nu for the spherical shell with the narrowest layer close to the cold boundary was about 16% higher than that of the equi-spaced spherical shell.

In the second stage of the study, we established the concept of “smart” thermo-insulation. The concept of design of "smart" thermally insulating materials based on heterogeneous, thermally, passive porous media, was established and extensively validated for both 2D and 3D confined natural convection flows. The porous media was modelled by unconnected packed beds of circular cylinders. The location of each cylinder was determined by an iterative procedure based on the linear stability analysis of the flow fields. The affect of both optimization criteria **A** and **B** related to perturbation of the velocity and the temperature fields respectively on insulation properties of 2D and 3D differentially heated cavities has been extensively investigated. It was found that for the given value of Ra , the implants of porous media designed by utilizing criterion **A** and occupying only 5% of the overall cavity volume can decrease the overall heat flux rate by a factor of 2 through the boundaries of 2D and 3D differentially heated cavities. In contrast, the implants of porous media designed by using criterion **B** can only decrease the heat flux rate by 30% for both 2D and 3D configurations. Implants of porous media designed by both criteria delay the transition to unsteadiness of the 2D natural convection flow, which is reflected by increasing the critical Ra_{cr} value by an order of magnitude when using the ultimate (consisting of 40 cylinders) patterns of implants of both types.

The present work summarizes my first effort aimed at developing a systematic formal methodology for establishing a concept for design of "smart" thermally, insulating materials. In practice, such materials can be built of heterogenous porous media whose geometry and spatial orientation is intelligently adapted to any specific engineering configuration. In the present study, the heterogeneous porous media was modelled by unconnected packed beds of equi-sized circular cylinders (both 2D and 3D). However, real porous media materials typically contain pores of varying sizes. Generalization of the results obtained in the present study for heterogeneous porous media, modelled by the cylinders of varying sizes, requires statistical evaluation of the whole set of "similar" systems, and will be the focus of future studies.

Bibliography

- [1] A. Samanta, D. Appelo, T. Colonius, J. Nott, J. Hall, "Computational modeling and experiments of natural convection for a titan mongolfiere," *AIAA Journal*, vol. 48, no. 5, pp. 1007-1016, 2010.
- [2] Y. Feldman, T. Colonius, M. T. Pauken, J. L. Hall, J. A. Jones, "Simulation and cryogenic experiments of natural convection for the Titan Montgolfiere," *AIAA Journal*, vol. 50, no. 11, pp. 2483-2491, 2012.
- [3] Y. Feldman, T. Colonius, "On a transitional and turbulent natural convection in spherical shells," *International Journal of Heat and Mass Transfer*, vol. 64, pp. 514-525, 2013.
- [4] E. H. Bishop, S. Kolflat, L. R. Mack, J. A. Scanlan, "Convective heat transfer between concentric spheres," in *Proceedings of the Heat Transfer and Fluid Mechanics Institute Stanford University Press, Palo Alto, CA*, pp. 69-80, 1964.
- [5] E. H. Bishop, L. R. Mack, J. A. Scanlan, "Heat transfer by natural convection between concentric spheres," *International Journal of Heat and Mass Transfer*, vol. 9, pp. 649-662, 1966.
- [6] L. R. Mack, H. A. Hardee, "Natural convection between concentric spheres at low Rayleigh numbers," *International Journal of Heat and Mass Transfer*, vol. 11, pp. 387-396, 1968.
- [7] J. A. Scanlan, E. H. Bishop, R. E. Powe, "Natural convection heat transfer between concentric spheres," *International Journal of Heat and Mass Transfer*, vol. 13, pp. 1857-1872, 1970.
- [8] S. H. Yin, R. E. Powe, J. A. Scanlan, E. H. Bishop, "Natural convection flow patterns in a spherical annuli," *International Journal of Heat and Mass Transfer*, vol. 16, pp. 1785-1795, 1973.
- [9] T. Fujii, T. Honda, M. Fujii, "A numerical analysis of laminar free convection around an isothermal sphere: Finite difference solution of the full Navier-Stokes and energy equations between concentric spheres," *Numerical Heat Transfer*, vol. 7, pp. 103-111, 1984.
- [10] M. Fujii, H. Takamatsu, T. Fujii, "A numerical analysis of free convection around an isothermal sphere (Effects of space and Prandtl number)," *Proceedings 1987 ASME-JSME Thermal Engineering Joint Conference*, vol. 4, pp. 55-60, 1987.
- [12] V. Travnikov, K. Eckert, S. Odenbach, "Influence of the Prandtl number on the stability of convective flows between non-isothermal concentric spheres," *International Journal of Heat and Mass Transfer*, vol. 66, pp. 154-163, 2013.

- [13] V. Travnikov, K. Eckert, S. Odenbach, "Linear stability analysis of the convective flow in a spherical gap with $\eta = 0.714$," *International Journal of Heat and Mass Transfer*, vol. 80, pp. 266-273, 2015.
- [14] R. Powe, R. Warrington, J. Scanlan, "Natural convective flow between a body and its spherical enclosure," *International Journal of Heat and Mass Transfer*, vol. 23, pp. 1337-1350, 1980.
- [15] B. Futterer, A. Brucks, R. Hollerbach, C. Egbers, "Thermal blob convection in spherical shells," *International Journal of Heat and Mass Transfer*, vol. 50, pp. 4079-4088, 2007.
- [16] A. Bejan, "Natural convection heat transfer in a porous layer with internal flow obstructions," *International Journal of Heat and Mass Transfer*, vol. 26, no. 6, pp. 815-822, 1983.
- [17] N. Tatsuo, N. Fumio, K. Yuji, "Natural convection in horizontal enclosures with multiple partitions," *International Journal of Heat and Mass Transfer*, vol. 32, no. 9, pp. 1641-1647, 1989.
- [18] Y. Varola, H. F. Oztop, A. Varol, "Effects of thin fin on natural convection in porous triangular enclosures," *Int. J. Therm. Sciences*, vol. 46, no. 10, pp. 1033-1045, 2007.
- [19] K. C. Chung, L. M. Trefethen, "Natural convection in a vertical stack of inclined parallelogrammic cavities," *International Journal of Heat and Mass Transfer*, vol. 25, no. 2, pp. 277-284, 1982.
- [20] T. Nishimura, M. Shiraishi, F. Nagasawa, Y. Kawamura, "Natural convection heat transfer in enclosures with multiple vertical partitions," *International Journal of Heat and Mass Transfer*, vol. 31, no. 8, pp. 1679-1686, 1988.
- [21] S. L. M. Junqueira, F. C. D. Lai, A. T. Franco, J. L. Lage, "Numerical investigation of natural convection in heterogeneous rectangular enclosures," *Heat Transf. Engin*, vol. 34, no. 5-6, pp. 460-469, 2013.
- [22] O. Laguerre, S. Benamara, D. Remy, D. Flick, "Experimental and numerical study of heat and moisture transfers by natural convection in a cavity filled with solid obstacles," *International Journal of Heat and Mass Transfer*, vol. 52, pp. 5691-5700, 2009.
- [23] M. Sathiyamoorthy, S. Narasimman, "Control of flow and heat Transfer in a porous enclosure due to an adiabatic thin fin on the hot wall," *Transport in Porous Media*, vol. 89, pp. 421-440, 2011.
- [24] S. D. Jamalud-Din, D. A. S. Rees, B. V. K. Reddy, A. Narasimhan, "Prediction of natural convection flow using network model and numerical simulations inside enclosure with distributed solid blocks," *Heat and Mass Transfer*, vol. 46, no. 3, pp. 333-343, 2010.

- [25] A. A. Merrikh, J. L. Lage, "Natural convection in an enclosure with disconnected and conducting solid blocks," *International Journal of Heat and Mass Transfer*, vol. 48, no. 7, pp. 1361-1372, 2005.
- [26] E. J. Braga, M. J. S. de Lemos, "Laminar natural convection in cavities filled with circular and square rods," *International Communications in Heat and Mass Transfer*, vol. 32, no. 10, pp. 1289-1297, 2005.
- [27] E. J. Braga, M. J. S. de Lemos, "Heat transfer in enclosures having a fixed amount of solid material simulated with heterogeneous and homogeneous models," *International Journal of Heat and Mass Transfer*, vol. 48, no. 23-24, pp. 4748-4765, 2005.
- [28] B.V. Antohe, J. L. Lage, "A general two-equation macroscopic turbulence model for incompressible flow in porous media using unit cell scale," *International Journal of Heat and Mass Transfer*, vol. 40, no. 13, pp. 3013-3024, 1997.
- [29] W. P. Breugem, B. J. Boersma, R. E. Uittenbogaard, "The laminar boundary layer over a permeable wall," *Transport in Porous Media*, vol. 59, pp. 267-300, 2005.
- [30] J. C. F. Pereira, I. Malico, T. C. Hayashi, J. M. F. Raposo, "Experimental and numerical characterization of the transverse dispersion at the exit of a short ceramic foam inside a pipe," *International Journal of Heat and Mass Transfer*, vol. 48, no. 1, pp. 1-14, 2005.
- [31] J. C. F. Pereira, I. Malico, T. C. Hayashi, J. M. F. Raposo, "Study of high Reynolds number pipe flows with porous inserts," *Journal of Porous Media*, vol. 15, pp. 549-563, 2012.
- [32] R. A. Silva, M. J. S. de Lemos, "Turbulent flow in channel occupied by a porous layer considering the stress jump at the interface," *International Journal of Heat and Mass Transfer*, vol. 46, no. 26, pp. 5113-5121, 2003.
- [33] K. Vafai, C. L. Tien, "Boundary and inertia effects on flow and heat transfer in porous media," *International Journal of Heat and Mass Transfer*, vol. 24, no. 2, pp. 195-203, 1981.
- [34] M. M. Al-Hazmi, "Analysis of coupled natural convection conduction," *Energy and Buildings*, vol. 38, no. 5, pp. 515-521, 2006.
- [35] M. M. Al-Hazmi, "Numerical investigation on using inclined partitions to reduce natural convection inside the cavities of hollow bricks," *International Journal of Thermal Sciences*, vol. 49, pp. 2201-2210, 2010.
- [36] S. Banerjee, A. Mukhopadhyay, S. Sen, G. Ganguly, "Natural convection in a bi-heater configuration of passive electronic cooling," *International Journal of Thermal Sciences*, vol. 47, pp. 1516-1527, 2008.

- [37] G. Nardini, M. Paroncini, "Heat transfer experiment on natural convection in a square cavity with discrete sources," *Heat and Mass Transfer*, vol. 48, pp. 1855-1865, 2012.
- [38] H. Vitoshkin, A.Y. Gelfgat, "On direct inverse of Stokes, Helmholtz and Laplacian operators in view of time-stepper-based Newton and Arnoldi solvers in incompressible CFD," *Communications in Computational Physics*, no. 14, pp. 1103-1119, 2013.
- [39] Y. Gulberg, Y. Feldman, "On laminar natural convection inside multi-layered spherical shells," *International Journal of Heat and Mass Transfer*, no. 91, pp. 908-921, 2015.
- [40] C. Peskin, "Flow patterns around heart valves: a numerical method," *Journal of Computational Physics*, no. 10, pp. 252-271, 1972.
- [41] K. Taira, T. Colonius, "The immersed boundary method: A projection approach," *Journal of Computational Physics*, no. 225, pp. 3121-3133, 2007.
- [42] A. Roma, C. Peskin, M. Berger, "An adaptive version of the immersed boundary method," *Journal of Computational Physics*, no. 153, p. 509-534, 1999.
- [43] M. Uhlmann, "An immersed boundary method with direct forcing for the simulation of particulate flows," *Journal of Computational Physics*, no. 209, pp. 448-476, 2005.
- [44] Y. Feldman, A. Y. Gelfgat, "On pressure velocity coupled time-integration of incompressible Navier Stokes equations using direct inversion of Stokes operator or accelerated multigrid technique," *Computers and Structures*, vol. 87, pp. 710-720, 2009.
- [45] S. V. Patankar, "Numerical heat transfer and Fluid Flow," McGraw-Hill, 1980.
- [46] A. Y. Gelfgat, "Three-dimensional instability of axisymmetric: Solution of benchmark problems by a low-order," *International Journal for Numerical Methods in Fluids*, no. 2007, pp. 269-294, 2007.
- [47] S. L. Xiaoye, J. W. Demmel, "SuperLU DIST: A scalable distributed memory sparse direct solver for unsymmetric linear systems," *ACM Transactions on Mathematical Software*, no. 29, pp. 110-140, 2003.
- [48] W. W. Ren, C. Shu, W. M. Yang, "Boundary condition-enforced immersed boundary method for thermal flow problems with dirichlet temperature condition and its applications," *Computers & Fluids*, no. 57, pp. 40-51, 2012.
- [49] A. Y. Gelfgat, "Stability of convective flows in cavities: Solution of benchmark problems by a low-order finite volume method," *International Journal for Numerical Methods in Fluids*, no. 53, pp. 485-506, 2006.

- [50] C. Chiu, W. Chen, "Transient natural convection heat transfer between concentric and vertically eccentric spheres," *International Journal of Heat and Mass Transfer*, no. 39 pp. 1439-1452, 1996.
- [51] H. Yoon, D. Yu, M. Ha, Y. Park, "Three-dimensional natural convection in an enclosure with a sphere at different vertical locations," *International Journal of Heat and Mass Transfer*, no. 53 pp. 3143-3155, 2010.
- [52] A. Dehghan, K. Masih, "Numerical simulation of buoyancy-induced turbulent flow between two concentric isothermal spheres," *Heat Transfer Engineering*, no. 31, pp. 33-44, 2010.
- [53] H. Chu, T. Lee, "Transient natural convection heat transfer between concentric spheres", *International Journal of Heat and Mass Transfer*, no. 36, pp. 3159-3170, 1993.
- [54] Y. Feldman, Y. Gulberg, "An extension of the immersed boundary method based on the distributed Lagrange multiplier approach," *Journal of Computational Physics* no. 322, pp. 248-266, 2016.
- [55] V. Theofilis, P. W. Duck, J. Owen, "Viscous linear stability analysis of rectangular duct and cavity flow," *Journal of Fluid Mechanics*, no. 505, pp. 249-286, 2005.
- [56] Y. Feldman, A. Y. Gelfgat, "Oscillatory instability of a three-dimensional lid-driven flow in a cube," *Physics of Fluids*, no. 22, 2010.
- [57] Y. Feldman, "Theoretical analysis of three-dimensional bifurcated flow inside a diagonally lid-driven cavity," *Theor. Comput. Fluid Dynam.* no. 29, pp. 245-261, 2015.
- [58] J. Xamán, G. Álvarez, L. Lira, C. Estrada, "Numerical study of heat transfer by laminar and turbulent natural convection in tall cavities of façade elements," *Energy and Buildings*, no. 37, pp. 787-794, 2005.
- [59] S. H. Yin, T.Y. Wung, K. Chen, "Natural convection in air layer enclosed within rectangular cavities," *International Journal of Heat and Mass Transfer*, no. 21, pp. 307-315, 1978.
- [60] V. A. F. Costa, M. S. A. Oliveira, A. C. M. Sousa, "Control of laminar natural convection in differentially heated square enclosures using solid inserts at the corners," *International Journal of Heat and Mass Transfer*, 46 (2003) 3529-3537.
- [61] Y. Gulberg, Y. Feldman, "Flow control through the use of heterogeneous porous media: "Smart" passive thermo-insulating materials", *International Journal of Thermal Sciences*, no. 110, pp. 369-382, 2016.

תקציר

המחקר הנוכחי התמקד בשיטות לבקרה פאסיבית של הזרימות, המונעות בכוחות תרמיים, בתווך סגור. בחלקו הראשון של המחקר, נחקרה ההשפעה של הגודל האפקטיבי של התא בבעיית מעבר חום בתווך כדורי על תכונות תרמיות. במסגרת זו, נחקרה זרימה למינארית בהסעה טבעית בתוך תווך כדורי בעל חוצצים פנימיים, הכולל שפה פנימית חמה ושפה חיצונית קרה. סימולציות נומרית, אשר בוצעו בשילוב עם שיטת "immersed boundary" למידול זרימת הסעה טבעית, בתוך תווך כדורי תלת-מימדי, בעל חוצצים פנימיים בעלי עובי אפסי בקונפיגורציות שונות: בחלוקה אחידה, בחלוקה לא אחידה, בחלוקה סימטרית סביב המרכז או לא סימטרית סביב המרכז. יעילות הבידוד התרמי של התווך הכדורי נבחנה עבור קונפיגורציות של עד ארבעה חוצצים פנימיים בחלוקה אחידה. כמו כן, פותחו פונקציות קורלציה עבור מספרי Nu^* ו- Ra^* לטובת קונפיגורציות של עד ארבעה חוצצים פנימיים בחלוקה אחידה. בנוסף, נבחנה ונמדדה ההשפעה של סטייה מהמרכז במישור האופקי ובמישור האנכי של החוצצים הפנימיים וכן סטיית רוחב, על ביצועי הבידוד התרמי של התווך הכדורי, כל זאת במונחי פונקציונאליות של Nu ו- Ra .

בחלקו השני של המחקר, טבענו את הקונספט של בידוד תרמי "חכם". התאמנו ובדקנו לעומק את הקונספט של חומרים מבודדים תרמיים "חכמים" ליישום בקונפיגורציות הנדסיות מסוימות. הבידוד התרמי הושג על-ידי דיכוי מקומי של התנע של הזרימות המונעות בכוחות תרמיים בתווך סגור, באזור הקריטי ביותר, כפי שנקבע על-ידי אנליזת "linear stability" של הזרימות, בנוכחות שתלים בתווך נקבובי הטרונגי. השתלים ממודלים על-ידי קבוצות של גופים גליליים, בעלי גודל אחיד, כאשר אין ביניהם מגע. הקונספט מבוסס על גישת סקלת ביניים ("approach mesoscale"), אשר עברה תנאי אי החלקה על השפה בקרבת הגופים השתולים מוטל ישירות על-ידי שימוש בשיטת "immersed boundary". במסגרת זו, נקבעו שני דפוסים שונים של החומרים הנקבוביים "החכמים" ותכונת הבידוד התרמי שלהם כומתה. ניתן לראות כי השתלים של החומר הנקבובי הטרונגי, המהווים רק כ-5% מהנפח הכללי של התווך, יכולים ליצור השפעה משמעותית על עיכוב במעבר ממצב יציב למצב לא יציב של זרימת הסעה טבעית בתווך דו-מימדי ריבועי, בעל קירות אנכיים חם-קר וקירות אופקיים מוליכים. בנוסף, הודגם כי השתלים מאפשרים להשיג הפחתה משולשת של קצב מעבר החום דרך תווך תלת-מימדי ריבועי, בעל קירות אנכיים חם-קר וקירות אופקיים מוליכים.

תוכן עניינים

1	מבוא וסקר ספרות	1
1	1.1 מוטיבציית המחקר.....	
1	1.1.1 הסעה טבעית בתוך קליפות כדוריות.....	
5	1.1.2 חומרים "חכמים" לבידוד תרמי פאסיבי.....	
7	1.2 מטרות המחקר.....	
9	רקע תאורטי	2
9	2.1 סקירת הפרק.....	
9	2.2 זרימת הסעה טבעית בלתי דחיסה בתווך תלת-מימדי.....	
9	2.2.1 מודל פיסיקאלי.....	
11	2.2.2 דיסקרטיזציה בזמן.....	
11	2.2.3 שיטת Immersed boundary: גישה ישירה.....	
16	2.3 בידוד תרמי "חכם" – קונספט ורקע תאורטי.....	
16	2.3.1 Fully pressure-velocity coupled direct (FPCD).....	
18	2.3.2 Implicit immersed boundary FPCD בזמן אינטגרציה.....	
21	2.3.3 פותרן Steady-state immersed boundary FPCD.....	
22	2.3.4 פותרן Linear stability immersed boundary FPCD solver.....	
26	תוצאות ודיון	3
26	3.1 סקירת הפרק.....	
27	3.2 קליפות כדוריות רב שכבתיות.....	
27	3.2.1 אימות.....	
37	3.2.2 דיון.....	
49	3.3 בידוד תרמי "חכם".....	
49	3.3.1 אימות של אנליזות יציבות לינארית.....	
52	3.3.2 תוצאות ודיון.....	
66	סיכום ומסקנות	4
68	ביבליוגרפיה	5



אוניברסיטת בן-גוריון בנגב
הפקולטה למדעי ההנדסה
המחלקה להנדסת מכונות

**שיטת IMMERSED BOUNDARY לחקירת
זרימות המונעות על ידי כוחות תרמיים
בנפחים סגורים**

חיבור זה מהווה חלק מהדרישות
לקבלת תואר "מגיסטר" בהנדסה

מאת: יוסף גולברג



אוניברסיטת בן-גוריון בנגב
הפקולטה למדעי ההנדסה
המחלקה להנדסת מכונות

שיטת IMMERSED BOUNDARY לחקירת זרימות המונעות על ידי כוחות תרמיים בנפחים סגורים

חיבור זה מהווה חלק מהדרישות
לקבלת תואר "מגיסטר" בהנדסה

מאת: יוסף גולברג

מנחה: דוקטור יורי פלדמן

חתימת המחבר..... תאריך.....

אישור המנחה/ים..... תאריך.....

אישור יו"ר ועדת תואר שני מחלקתית..... תאריך.....